# Computer simulation of oxide surfaces and grain boundaries

Davies, M. J.

*Award date:*
1992

*Awarding institution:*
University of Bath

**Computer Simulation of Oxide Surfaces and Grain Boundaries**

submitted by M. J. Davies

for the degree of PhD

of the University of Bath

1992







ProQuest LLC
789 East Eisenhower Parkway
P.O. Box 1346
Ann Arbor, MI 48106-1346

**Abstract**

The aim of this thesis is to employ computer simulation techniques to study the surface and grain boundary properties of a range of oxides. Chapter 1 provides an introduction to the current state of experimental and simulation techniques in determining the properties of surfaces and grain boundaries in oxides. The two following chapters outline the theoretical methods employed in atomistic simulation and described the potential models used for the calculations presented in this thesis.

The remainder of this thesis presents the calculated results. In chapter 4 the energies of the low index surfaces of a range of oxides are considered. These include the surfaces of wüstite (FeO), rutile ($TiO_2$), spinel ($MgAl_2O_4$), magnetite ($Fe_3O_4$) and forsterite ($Mg_2SiO_4$). The results establish the importance of surface relaxation and its effects on surface structure. Rearrangement of the cation distribution at the surface of spinel is considered. Predicted equilibrium morphologies based on Wulff's theorem are employed as a means of testing the simulation results by comparing them with experimental crystals.

The structure, energies and formation energies of defects at the surfaces of hematite are discussed in chapter 5. The energies of cation and anion vacancies close to two of the low index surfaces of hematite have been calculated. In addition isovalent impurity segregation to all of the low index surfaces of hematite is considered.

In chapter 6 the structures of the low index mirror twins in hematite are discussed. Minimum energy configurations for each twin are obtained. Both the vacancy formation energies and the isovalent segregation energies are presented for the basal and rhombohedral twins.

**Acknowledgements**

I would firstly like to thank my supervisor Dr S. C. Parker for all his help, encouragement and most of all for his infinite patience.

I would also like to thank Jez, Romek, Jerzy, Chris, and Tom for all there pestering over the past two years.

I am gratefully to Ian and Helen Walker for continually tell me I would make it.

Many thanks to Dr Alison Wall for all her help during the writing of this thesis.

Finally I would like to express my gratitude to Parish, Millington, Pete and Greg for helping to maintain my sanity over the years and for all their assistance in saving the multiverse on numerous occasions.

## Contents

# Chapter 1

# Introduction

The structures and properties of the surfaces and internal boundaries of oxides influences many processes in material science. They are directly involved in catalysis, corrosion, crystal growth and sintering. Therefore a knowledge of their composition, structure and energetics is a prerequisite for a greater understanding of such processes. Despite recent advances in surface analytical techniques [1, 2], however, data on the detailed surface atomic arrangements of oxides are still difficult to obtain and hence sparse [3]. Atomistic simulation can therefore, not only be of use in the interpretation of exiting experimental data but also in the investigation and prediction of surface and interfacial properties outside the usual or accessible experimental conditions. We shall now start by giving a brief review of recent developments in experimental and atomistic simulation techniques.

## 1.1 Recent Developments

### 1.1.1 Experimental

The surfaces and grain boundaries of ionic solids in general, and metal oxides in particular, are difficult to investigate and characterise experimentally. This is partly due to the difficulty of obtaining pure well characterised single crystals [4], but also because of a surface charging problem. Charged particles used in many surface spectroscopic techniques interact with the charged surfaces of oxides making it difficult to resolve and interpret experimental data [5]. This problem has recently been reduced by increasing the resolution, sensitivity and detection limits of electron optic techniques. This has facilitated the probing of the outermost layers of surfaces.

The current methods used in surface analysis can be divided roughly into three groups, those that give information on the chemical composition, the lattice

structure and the energetics of surfaces. The latter may again be sub-divided into investigations on electrons and phonons at surfaces. Determination of the lattice structure can be achieved by either exploiting the periodic long range nature of the surface, for example LEED (low energy electron diffraction) [6], or by investigating the surface structure with atomic resolution, e. g. STM (scanning tunnelling microscope) [7] and AFM (atomic force spectroscopy) [2]. The composition and energetics of surfaces can also be determined by investigating their interaction with electron, ions, atoms and photons. Some of these techniques are non-destructive e.g. AES (auger electron spectroscopy) [8] while others erode the surface structure [9]. This latter effect can be utilised to investigate the composition with depth below the surface [9]. A recent review of the versatility and use of the available techniques is give by Hirschwald [10].

The number of techniques available to investigate grain boundaries are much more limited. The composition of grain boundaries may be determined using some of the techniques applied to surfaces, e.g. AES. Determination of boundary structure, however, is limited to diffraction and direct imaging techniques [11]. The periodicity of the boundary may be reflected in X-ray diffraction patterns where additional spots may indicate the presence of structures such as dislocation arrays. Furthermore, streaks present in the patterns give some information about the periodicity perpendicular to the boundary and hence the boundary width [12]. Direct imaging techniques such as HREM (high resolution electron microscopy) allow observation of the boundary structures at atomic level resolution [13]. To derive reliable atomic position from such images a series of images are mated to proposed structures.

### 1.1.2 Lattice simulation

The development of efficient computer simulation techniques over the last twenty five years had provided a notable complement to experiment in determining the properties of a wide range of materials. Early work by Norgett and Lidiard [14] showed that atomistic simulation could be used to reliably calculate the bulk

defect properties of halides. The scope of atomistic simulation was extended by Catlow [15] to include the fluorite structured halide and oxides. The methods were further used to study both cubic [16] and non-cubic [17] oxides, and more recently to study of ternary oxides [18] and minerals [19]. This work on bulk structures was built upon to develop the codes required to handle surface simulation. Initial surface studies were confined to alkali halides [20] but following the development of reliable potentials describing the interionic forces in ionic solids, cubic [21] and non-cubic [22] binary oxide surfaces have been investigated.

The scope of atomistic simulation has also been extended to the study of grain boundaries. Duffy and Tasker [23, 24] have used these techniques to investigate the structures of tilt boundaries in NiO and cation diffusion along these boundaries [25]. Also Stoneham and Tasker [26] have built on this work in the study of the structures of boundaries between different dielectrics, NiO and BaO. The inclusion of image charge effects, which influence many of the properties of interfaces between metals and ionic solids [27] will further increase our understanding of processes such as catalysis and corrosion [28].

The critical test of the quality of any atomistic simulation is the ability of the simulation to reliably reproduce the results of experimentally well characterised systems. Where such comparisons have been made for bulk properties [29] the agreement is excellent. Similarly for surface segregation [30] good agreement has been achieved. We can therefore be confident that application of atomistic simulation techniques can further our understanding of systems that are poorly understood experimentally.

## 1.2 Aims of this work

Previously, atomistic simulations have been used to calculate the structures and energies of the surfaces of binary halides [20] and oxides [21, 22]. The aim of the work described in chapter 4 is to extend these calculation to a range of new materials. These include spinel, a ternary oxides, and forsterite a silicate.

Experimental measurement of surface energies is both difficult and unreliable [31], hence comparison with calculated surface energies is impossible. In chapter 4 we propose the use of equilibrium morphologies calculated using Wulff's theorem [32] as a means of comparing with real systems.

Atomistic simulations of grain boundaries in oxides have in the main been limited to cubic systems [24, 33]. In this thesis we propose to extend this work to consider grain boundaries in hexagonal systems, specifically hematite. In chapter 5 we firstly consider the surfaces of hematite. In addition to surface energy calculations we shall present calculations of the vacancy formation energies near to surfaces and the heats of segregation of isovalent impurities to the hematite surfaces. Then in chapter 6 we consider the mirror twin boundaries in hematite. The structure of the minimum energy configurations will be determined and the vacancy energies near and segregation energies to the boundaries will be considered and contrasted with those of the surfaces.

## Chapter 2

## Theoretical Methods

In this chapter we shall discuss the theoretical methods used in the calculation of the energies and properties of two-dimensionally periodic interfaces in ionic materials. These methods are embodied in the computer codes MIDAS [34] and CHAOS [35] which were used in the preparation of the results presented in this thesis.

We shall firstly describe methods for calculating and then minimising the energies of two-dimensionally periodic ionic lattices. Then given these methods, we shall consider the techniques employed in MIDAS and CHAOS which allow us to calculate the energies of extended planar defects and point defects close to interfaces.

### 2.1 Lattice Energy

The cohesive energy of an ionic lattice can be considered, according to the Born Model [36], as the sum of the pair-wise ionic interactions. These pair-wise interactions themselves can be considered to be made up of two terms, an electrostatic term due to the charged nature of the ions, and a short range hard core term due to the interaction between the electron clouds of neighbouring ions. Therefore the contribution to the lattice energy of the interaction between an ion $i$ in the reference unit cell and an ion $j$ in the $l^{th}$ unit cell can be expressed as

$$\mathrm{U}_{ij} = q_i q_j (|r_i - r_j + r_l|)^{-1} + \phi_{ij}(|r_i - r_j - r_l|) \qquad (2.1)$$

where $q_i$ and $q_j$ are the charges on the ions $i$ and $j$ at positions $r_i$ and $r_j$ respectively. $r_l$ is the lattice vector to the $l^{th}$ unit cell and $\phi_{ij}$ is some function which describes the short range interaction between ions $i$ and $j$. The form of this short range interaction will be discussed in chapter 3.

The total lattice energy can be expressed as

$$U_{lattice} = \sum_{l}{}' \sum_{i,j} \frac{q_i q_j}{|r_i - r_j + r_l|} + \sum_{l}{}' \sum_{i,j} \phi_{ij}(|r_i - r_j - r_l|) \qquad (2.2)$$

where the superscript prime in the summations indicates that the case $l = 0$ is excluded for $i = j$. The dominant electrostatic part of this sum presents a computational problem due to its long range nature and slow convergence. This is overcome for bulk three dimensionally periodic lattices using a method originally developed by Ewald [37]. Parry [38, 39] taking a limited case of the Ewald method developed a similar technique for efficiently calculating the Coulombic sum in a two dimensionally periodic lattice, it is this method we present here.

### 2.1.1 Coulombic Sum – Parry Method

The electrostatic contribution to the lattice energy in equation (2.2) can be rewritten as

$$U_{Mad} = \frac{1}{2} \sum_{i,j} q_i q_j M_{ij} \qquad (2.3)$$

where

$$M_{ij} = \sum_{l} \frac{1}{|r_{ij} + r_l|} \qquad (2.4)$$

$$r_{ij} = r_i - r_j \qquad (2.5)$$

In the Parry Method $r_l$ is the two dimensional lattice vector.

$M_{ij}$ can now be evaluated using the integral form of $1/|z|$, that is

$$\frac{1}{|z|} = \frac{2}{\sqrt{\pi}} \int_0^\infty \exp(-z^2\rho^2)\, d\rho \qquad (2.6)$$

giving

$$M_{ij} = \sum_{l} \frac{1}{|r_{ij} + r_l|} = \sum_{l} \frac{2}{\sqrt{\pi}} \int_0^\infty \exp(-(|r_{ij} - r_l|)^2\rho^2)\, d\rho \qquad (2.7)$$

Now following Tosi [40] we can split this integral about some arbitrary point $G$ to give

$$M_{ij} = M_{ij}^{G} + M_{ij}^{R} \tag{2.8}$$

$$\begin{aligned} M_{ij} = & \sum_{l} \frac{2}{\sqrt{\pi}} \int_{0}^{G} \exp(-(|r_{ij} + r_{l}|)^{2}\rho^{2})\, d\rho \\ & + \sum_{l} \frac{2}{\sqrt{\pi}} \int_{G}^{\infty} \exp(-(r_{ij} + r_{l})^{2}\rho^{2})\, d\rho \end{aligned} \tag{2.9}$$

The first integral, $M_{ij}^{G}$, can be evaluated in reciprocal space using fourier transform methods to give

$$\begin{aligned} M_{ij}^{G} = \frac{\pi}{A}\Bigg\{ & -2u_{ij}\,\mathrm{erf}(Gu_{ij}) - \frac{2\exp(-G^{2}u_{ij}^{2})}{\pi^{\frac{1}{2}}G} \\ & + \sum_{k\neq 0} \frac{\exp(ik.p_{ij})}{k}\Big[\exp(ku_{ij})\,\mathrm{erfc}(\frac{k}{2G} - Gu_{ij}) \\ & + \mathrm{erf}(-ku_{ij})\,\mathrm{erfc}(\frac{k}{2G} + Gu_{ij})\Big]\Bigg\} \end{aligned} \tag{2.10}$$

where $k$ is the two dimensional reciprocal lattice vector, $A$ is the surface unit cell area, erf and erfc are the standard and complementary error functions respectively, and $r_{ij}$ has been resolved into two components, $p_{ij}$ in the plane of the lattice vectors $r_{l}$, and $u_{ij}$ perpendicular to the plane.

The second integral, $M_{ij}^{R}$, in (2.9) can be handled simply in real space to give

$$M_{ij}^{R} = \sum_{l} \frac{\mathrm{erfc}(G|r_{ij} - r_{l}|)}{|r_{ij} - r_{l}|} \tag{2.11}$$

$M_{ij}$ is calculated without the singularity $l = 0$ term in real space summation and $2G/\pi^{\frac{1}{2}}$ is subtracted to remove the self-interaction term included in the reciprocal space summation. G, the arbitrary point, is chosen to minimise the total number of terms in the sum. A value of $(\pi/A)^{\frac{1}{2}}$ has been found to be a good value for the type of calculations carried out in this thesis. A more detailed derivation

of the expressions above using a more rigorous approach than Parry is given by Heyes et al, reference [41]. In addition to the energy, we also require the first and second derivatives of the energy with respect to the ion position, expressions for these are given by Harding [42].

## 2.2 Minimisation Methods

In the simulation of ionic systems we are interested in obtaining the equilibrium configuration. That is we need to reduce the system to zero strain by solving the equilibrium condition

$$\frac{\partial U}{\partial \underline{r}} = 0 \tag{2.12}$$

This is achieved, in the programs used in this thesis, by means of a Newton-Raphson variable matrix method which we shall outline here.

The lattice energy is firstly expanded about a point $r$ to second order

$$U(\underline{r}^*) = U(\underline{r}) + \underline{g}^t\underline{\delta} + \frac{1}{2}\underline{\delta}^t\underline{\underline{W}}\,\underline{\delta} \tag{2.13}$$

where $\underline{\delta}$ is a vector of the ionic displacements

$$\underline{\delta} = \underline{r}^* - \underline{r} \tag{2.14}$$

$\underline{g}$ is a vector of the first derivatives of the energy

$$\underline{g} = \frac{\partial U}{\partial \underline{r}} \tag{2.15}$$

and $\underline{\underline{W}}$ is the corresponding matrix of second derivatives

$$\underline{\underline{W}} = \frac{\partial^2 U}{\partial \underline{r}\partial \underline{r}} \tag{2.16}$$

Hence for equilibrium, combining equations (2.12) and (2.13) gives

$$\frac{\partial U}{\partial \underline{r}} = 0 = \underline{g} + \underline{\underline{W}}\,\underline{\delta} \tag{2.17}$$

Thus U($\underline{r}$) has a minimum when

$$\underline{g} = -\underline{\underline{W}}\,\underline{\delta} \tag{2.18}$$

and the optimum ion displacement to achieve equilibrium is given by

$$\underline{\delta} = -\underline{\underline{W}}^{-1}\underline{g} \tag{2.19}$$

Unfortunately the lattice energy is not strictly harmonic and therefore equation (2.19) will not lead us directly to the equilibrium configuration. It will, however, usually represent a configuration closer to the minimum and thus by repeated uses of equation (2.19) over several iterations the equilibrium configuration may be found.

This approach is very reliable but suffers from the problem that evaluating and inverting the second derivative matrix $\underline{\underline{W}}$ is very time consuming. This problem is partially overcome by updating the inverted matrix $\underline{\underline{W}}^{-1}$ for successive iterations using an approximation, and only recalculating $\underline{\underline{W}}^{-1}$ after a set number of iterations have elapsed. The essence of this approach is to replace equation (2.19) with a similar equation of the form

$$\underline{\delta} = -\lambda\underline{\underline{H}}\,\underline{g} \tag{2.20}$$

where $\underline{\underline{H}}$, the Hessian, is initially set to equal $\underline{\underline{W}}^{-1}$ and $\lambda$ is a linear parameter initially set to 1. Therefore for the $k+1$ iteration the ionic displacements are given by

$$\underline{\delta}_k = -\lambda_k\underline{\underline{H}}_k\underline{g}_k \tag{2.21}$$

where

$$\underline{\delta}_k = r_{k+1} - r_k \tag{2.22}$$

Then using an approximation developed by Davidon [43], Fletcher and Powell [44] the Hessian for the next iteration can be estimated

$$\underline{\underline{H}}_{k+1} = \underline{\underline{H}}_k - \frac{\underline{\delta}_k\underline{\delta}_k^t}{\underline{\delta}_k^t\underline{\delta}_k} - \frac{\underline{\underline{H}}_k\underline{\delta}_k\underline{\delta}_k^t\underline{\underline{H}}_k}{\underline{\gamma}_k^t\underline{\underline{H}}_k\underline{\gamma}_k} \tag{2.23}$$

where

$$\underline{\gamma}_k = \underline{g}_{k+1} - \underline{g}_k \tag{2.24}$$

The new coordinate positions for the $k+2$ iteration can then be calculated. This approach only requires the recalculation of the first derivatives, $\underline{g}$, for each iteration and hence is much less time consuming than recalculating the second derivative matrix each iteration.

## 2.3 Calculation of the energies of extended planar defects

Throughout this thesis the computer code MIDAS (**M**inimisation of **I**nterfacial **D**efects **A**nd **S**urfaces), developed by P.W. Tasker [34] at AERE Harwell, has been used to calculate the energies and structures of planar defects. This code allows us to calculate the relaxed structure and energy of any planar defect which possess a high degree of two dimensional periodicity. Examples of such defects are surfaces, shear planes, stacking faults and grain boundaries.

The basic approach taken by MIDAS is to consider the crystal as a block consisting of a stack of planes periodic in two dimensions and parallel to the plane of the defect. By considering one such block surfaces may be simulated. By putting two blocks together with a mismatch in their structures, interfaces such as stacking faults can be considered, figure 2.1. To facilitate the energy calculation the block is divided into two regions as illustrated in figure 2.1. An inner region I surrounding the defect in which the ions are relaxed to equilibrium, and an outer region II in which the ions are held fixed but the region as a whole is allowed to move. The two dimensional periodicity of the system is exploited to minimise the number of ions modelled explicitly, but it should be noted that this periodicity is determined by the structure of the defect and thus the unit cell may be larger than that for a bulk plane.

The energy of the block is split into two parts

$$E = E_1 + E_2 \tag{2.25}$$

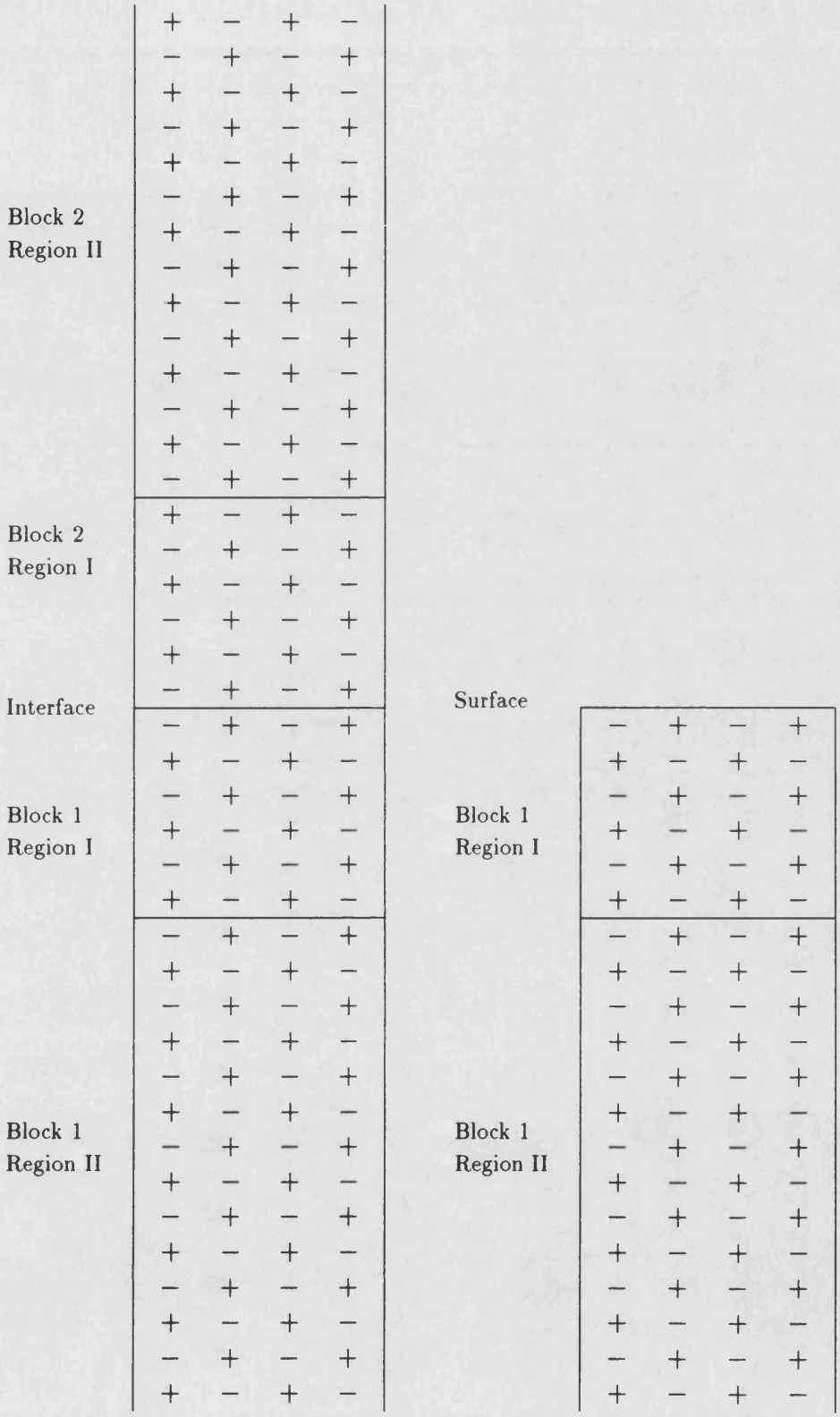


Figure 2.1: Midas block structure for interface and surface calculations.

each arising from the energies of the ions in region I and region II respectively. Assuming only pair potentials, $U_{ij}(r)$ as in section 2.1, then the the energy of region I, $E_1$, may be expressed as

$$E_1 = \sum_{\substack{i\in I \\ j\in I}} \sum_{l}{}' U_{ij}(|r_{ij} + r_l|) + \frac{1}{2} \sum_{\substack{i\in I \\ j\in II}} \sum_{l} U_{ij}(|r_{ij} + r_l|) \tag{2.26}$$

where $r_{ij} = r_i - r_j$ and $r_l$ is the two dimensional lattice vector. The first term corresponds to the interaction between the ions in region I, the second term to the interaction between region I and region II. Similarly the energy of region II, $E_2$, may be expressed as

$$E_2 = \frac{1}{2} \sum_{\substack{i\in I \\ j\in II}} \sum_{l} U_{ij}(|r_{ij} + r_l|) + E_{22} \tag{2.27}$$

Only interactions in region II that are affected by the defect or relaxation of region I need be included in $E_2$. The first term in equation (2.27) is equivalent to the second term in equation (2.26) and represents the interaction between region I and region II. The second term, $E_{22}$, includes interactions within region II that are affected by region I. This must be evaluated if a long range field causes polarisation in region II. For rigid outer boundaries it can generally be neglected except for cases of dipolar systems which we shall discuss in the next section.

The energies $E_1$ and $E_2$ are evaluated using the methods described in section 2.1, the Coulombic contribution is handled using the Parry method. The derivatives of the energy with respect to the ionic coordinates in region I, and with respect to the position of the outer region II are evaluated simultaneously with the energy calculation and the block is relaxed to equilibrium using the methods discussed in section 2.2.

### 2.3.1 Charged Planes

In certain crystal directions the planes making up the crystal block used in MIDAS are charged, for example they may consist of just anions or cations. This

presents no problem if there is no dipole moment in the repeat unit perpendicular to the planes. If, however there is a dipole moment, a neutral block built from such a stack of planes will have a net dipole moment polarising the ions in the block and resulting in an infinite surface energy. This follows from a consideration of the electrostatic potential within the crystal block for such a stacking sequence.

The contribution to the electrostatic potential within the crystal block due to a planar sublattice of charge $q$ at a perpendicular distance $z$ can easily be evaluated using the Parry expressions described in section 2.1. For large perpendicular distances $z$ the expression reduces to a particularly simple form

$$V(z) = \frac{2\pi}{A} qz \tag{2.28}$$

where $A$ is the area of the unit cell in the plane. This is identical to the expression for the potential due to an infinite charged plane of charge density $\rho = q/A$. The field , $E$, due to the charged plane is then given by

$$E = 2\pi \frac{q}{A} \tag{2.29}$$

Since equations (2.28) and (2.29) do not diminish with increasing $z$ the electrostatic sum must be infinite over the whole crystal unless cancellation of these terms takes place.

Now if we consider the three stacking sequences shown in figure 2.2 we can see the effect of a dipolar repeat perpendicular to the stacking direction. In figure 2.2a each plane is neutral, since it consists of both anions and cations in a stoichiometric ratio. The potential, equation (2.28), cancels on each plane since the contribution of the sublattices are equal and opposite. If additional planes are added to the crystal block they make no contribution to the energy of the ions in the bulk and therefore the lattice sums required for the Coulombic energy at any ion site require only a few planes either side of that site to converge.

Figure 2.2b shows a stacking sequence consisting of charged planes. Three planes make up a symmetrical repeat unit which therefore has no dipole moment

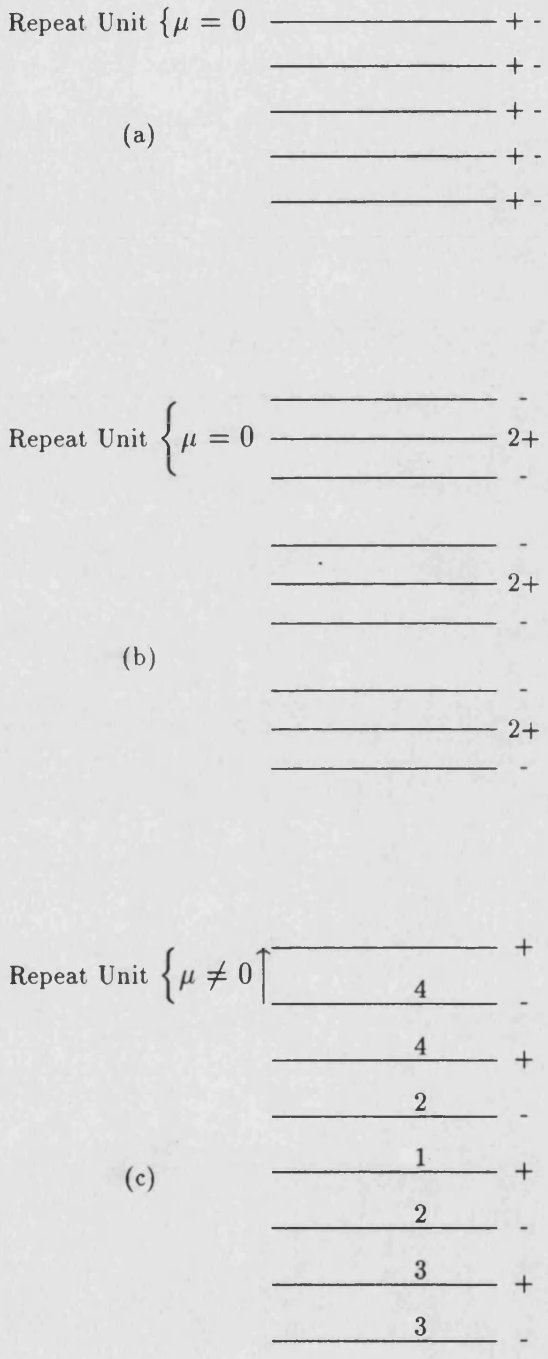


Figure 2.2: Distribution of charges on planes for stacking sequences parallel to surface.

perpendicular to the surface. Each plane contributes a term in the potential of the form of equation (2.28), but a sum over the three plane repeat unit cancels the potential to zero. Hence addition of extra neutral repeats units to the crystal block will not modify the energy of ions in the bulk, and again the Coulombic sums for the potential at any ion site converge rapidly.

In contrast to the above, consider the stacking sequence shown in 2.2c which consists of alternately charged planes which produce a dipole moment perpendicular to the surface. The two plane repeat unit will produce a potential at large distances. This can be seen if we consider the plane labelled 1. The field from the planes labeled 2 cancel by symmetry, those labelled 3 and 4 both contribute a dipole layer and so their contribution to the potential is zero. This leaves the effect of the surface plane which will always be present in a neutral block. Similar arguments can be applied for any plane in the crystal and therefore the addition of extra neutral repeats units will still contribute to the energy of ions at an infinite distance below the surface thus leading to a divergent Coulombic sum and an infinite surface energy.

Kummer and Yao [45] have indicated that the field within a crystal terminated with such faces may be removed by transfer of half a plane of charge between opposite faces, as illustrated in figure 2.3. This may be viewed as a restructuring of the two free surfaces to minimise the surface energy. The two opposite halves of region II in figure 2.3 are now charged, in this case by $-\frac{1}{2}e/A$. The interaction between the two halves must therefore be included in equation (2.27) since it varies with dilation of region I. Using the expressions for the Coulombic sum given in section 2.1.1, it can easily be shown that the region II interaction energy is given by

$$E_{22} = \frac{\pi |e|^2}{2A} u \tag{2.30}$$

where u is the perpendicular distance between the two halves of region II. In the case of a surface, the halving of the charge at the surface is achieved by creating

vacancies. No $E_{22}$ term is required for surfaces as there is only a single block and therefore only one continuous region II.

## 2.4 Calculation of the energy of point defects near interfaces

The inclusion of charged point defects make the calculation of the energies of point defects near interfaces more complex than the calculation of extended planar defects covered in the previous sections. The computer code CHAOS (Computer simulation **HA**des **O**n **S**urfaces) based on the bulk defect energy code HADES [46] has been developed by Duffy and Tasker [35] to deal with such calculations. The defect energies in these programs are calculated by comparison to a perfect lattice. In the case of CHAOS the perfect lattice energy and structure are obtained from MIDAS.

Both CHAOS and HADES are based on the Mott-Littleton [47] method for the calculation of the formation energies of charged point defects. As in MIDAS the crystal is divided into two regions, figure 2.4. In region I, a spherical or hemispherical region surrounding the defect, all ions are treated explicitly and relaxed to equilibrium. Region II, the rest of the crystal, is treated as a dielectric continuum polarised according to the Mott-Littleton formulation. Region II itself is further sub-divided into two parts, region IIa a spherical or hemispherical shell surrounding region I in which the short range interactions with region I are explicitly calculated and region IIb in which the interaction with region I is approximated as the interaction between charged induced dipoles which solely involve the defect.

The total energy of such a system can be written as the sum of three terms

$$\mathrm{U}(x,y) = \mathrm{U}_1(x) + \mathrm{U}_2(x,y) + \mathrm{U}_3(y) \qquad (2.31)$$

where $\mathrm{U}_1(x)$ is the energy of region I, $\mathrm{U}_3(y)$ is the energy of region II, and $\mathrm{U}_2(x,y)$ is the interaction between the two regions. $x$ and $y$ are vectors that represent the

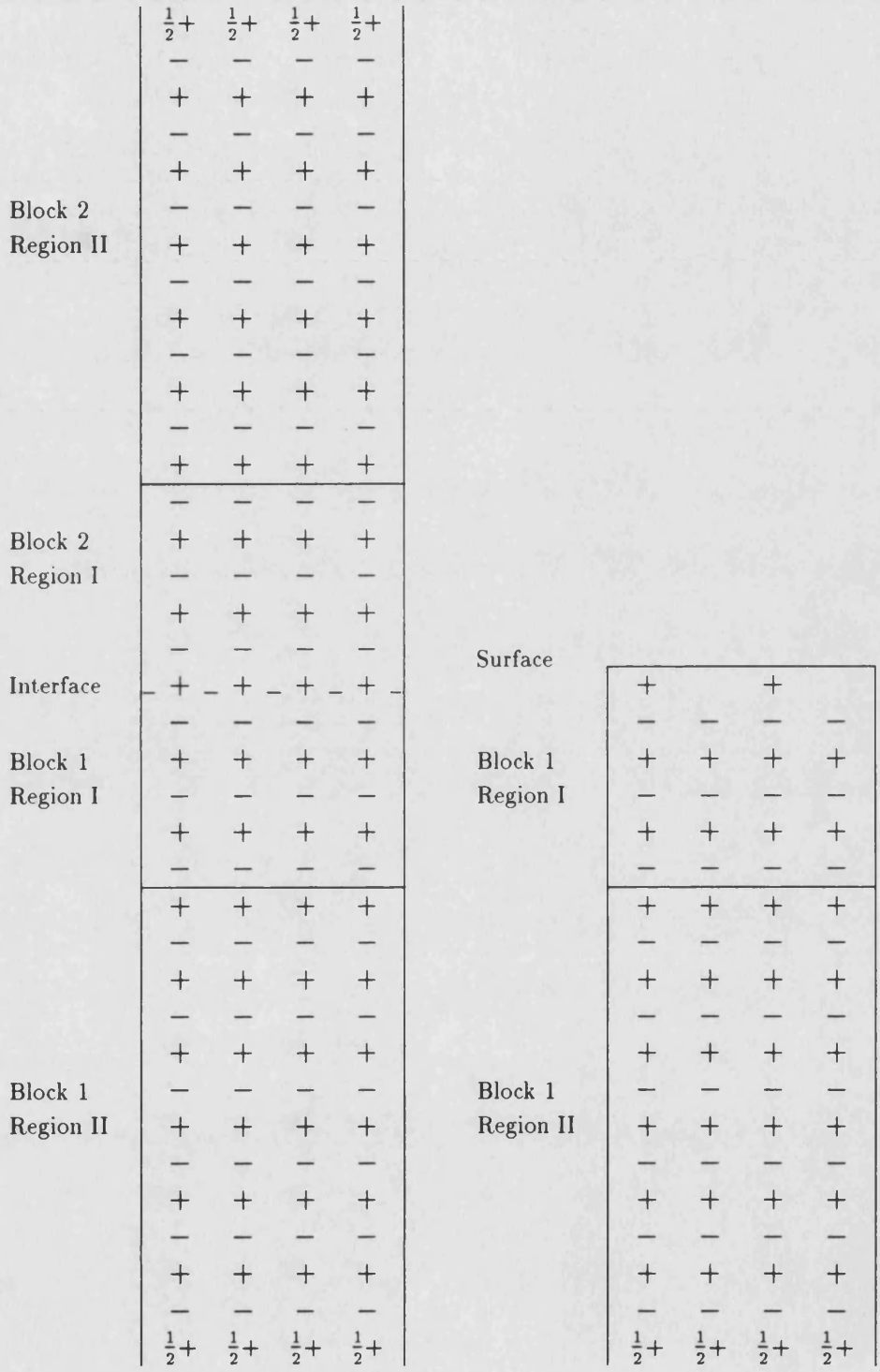


Figure 2.3: Removal of dipole for MIDAS interface and surface block structures.

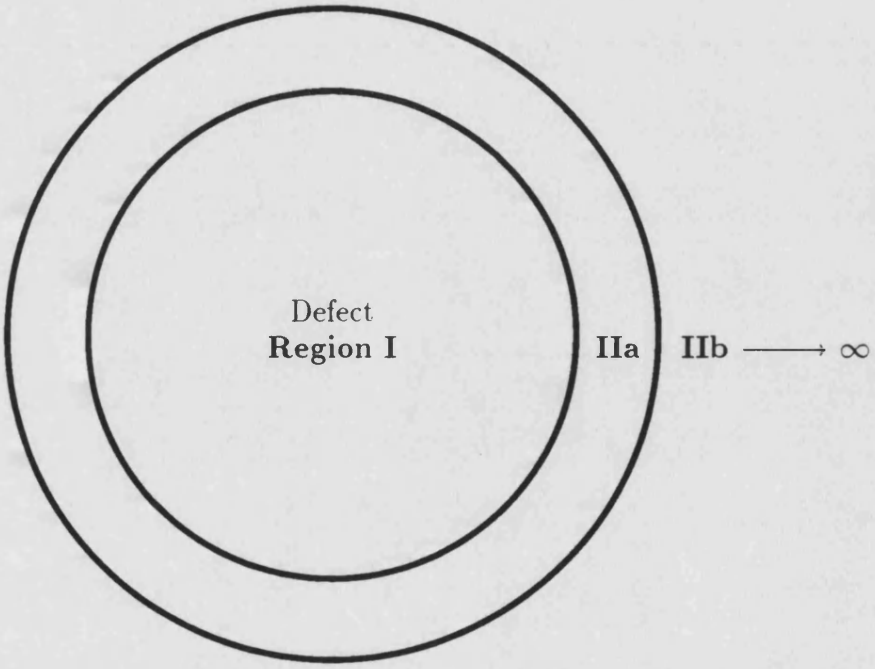


Figure 2.4: Two-region approach used in HADES and CHAOS.

coordinates of ions in region I and II respectively. Now if $U_3(y)$ is defined to be a quadratic function in $y$

$$U_3(y) = \frac{1}{2}\underline{y}^t \underline{\underline{A}}\, \underline{y} \tag{2.32}$$

Substituting this expression into equation (2.31) and assuming the equilibrium condition for region II then

$$\frac{\partial U(x,y)}{\partial \underline{y}} = \frac{\partial U_2(x,y)}{\partial y}|_{\underline{y}=\underline{\bar{y}}} + \underline{\underline{A}}\,\underline{\bar{y}} = 0 \tag{2.33}$$

where $\underline{y} = \underline{\bar{y}}$ at equilibrium. This leads us to an alternative expression for $U_3(y)$

$$U_3(y) = \frac{1}{2}\frac{\partial U_2(x,y)}{\partial \underline{y}}|_{\underline{y}=\underline{\bar{y}}}.\underline{\bar{y}} \tag{2.34}$$

and hence also for the total energy $U(x,y)$

$$U(x,y) = U_1(x) + U_2(x,y) + \frac{1}{2}\frac{\partial U_2(x,y)}{\partial \underline{y}}|_{\underline{y}=\underline{\bar{y}}}.\underline{\bar{y}} \tag{2.35}$$

The defect energy can be found by iteratively minimising the forces on each ion in region I to zero

$$\frac{\partial U(x,y)}{\partial x}|_{\underline{y}=\underline{\bar{y}}} \tag{2.36}$$

as the total energy $U(x,y)$ can now be calculated by considering only interactions within region I and between region I and II.

The Coulombic contribution to the energy of region I is calculated using the appropriate method for the system involved, the Ewald method in HADES, Parry method in CHAOS. Treatment of the Coulombic interactions which extend into region II are handled via a continuum approximation developed from the classical polarisation theory of Mott and Littleton. For bulk defect calculations using HADES this leads to a $r^{-4}$ interaction term which diminishes with increasing region I size. In CHAOS however, in order to take into account structural variations around the planar defect the Coulombic contribution is calculated by means of a

discrete sum of planar integrals around the interface and a volume integral over the remainder of the crystal. The planar integral takes into account any dilation of the crystal at the interface, thus

$$E_{IIb} = \frac{Q}{2}[\sum_{p\in I,IIa}\sum_{k}\int_{(R_{IIb}^2-r_k^2)^{\frac{1}{2}}}^{\infty}\frac{1}{r^2+r_p}2\pi r dr + \frac{1}{2}\sum_{k}q_k K_k\int_{R_{IIb}}^{\infty}\frac{1}{r^4}4\pi r^2 dr] \tag{2.37}$$

where $r_p$ is the perpendicular distance between the origin and the plane.

The other important consequence of charged defects at surfaces or interfaces is the interaction of the defects with their image charge. When the interface is between two materials of different dielectric constants, $\epsilon_1$ and $\epsilon_2$, the image charge is given by [48]

$$q_{image} = q_{def}\frac{(\epsilon_1-\epsilon_2)}{(\epsilon_1+\epsilon_2)} \tag{2.38}$$

where $q_{def}$ is the net charge on the defect and $\epsilon_1 > \epsilon_2$. The field due to this image charge must be included when calculating the displacement of the ions in region IIa and the polarisation of region IIb. The image charge is assumed to be situated half an interplanar spacing outside the last plane of ions. This is consistent with the method used to calculate the energy of the outer continuum where the polarisation is assumed to be caused by the total defect charge concentrated at the origin.

## Chapter 3

## Potential Models

The success of any calculation on perfect or defective lattices is critically dependent on the potential model used to describe the interionic interactions in the lattice. In this chapter, therefore, we shall outline the form of the potential model used in the calculations presented in this thesis, discuss how the important phenomena of polarisability is include in this potential model and finally describe the methods by which potential parameters are derived.

### 3.1 The form of the potential model

The starting point for any atomistic simulation technique is the evaluation of the lattice energy of a perfect lattice. For ionic and semi-ionic materials this may be expressed using the Born model as

$$\mathrm{U}_{lattice} = \sum_{i,j}{}' \frac{|e|^2 q_i q_j}{4\pi\epsilon_0 |r_i - r_j|} + \sum_{i,j}{}' \phi_{ij}(r_i, r_j) \tag{3.1}$$

where $q_i$ and $q_j$ are the charges on the ions $i$ and $j$ at positions $r_i$ and $r_j$i, $e$ is the electronic charge, $\epsilon_0$ is the permittivity of free space and $\phi_{ij}$ is the short range interaction between ions $i$ and $j$. The primes in the summations indicate that multiple counting of equivalent terms (e.g. $ij$ and $ji$) are avoided.

The major contribution to the lattice energy comes from the first term, the electrostatic or Coulombic term. This term converges slowly if evaluated explicitly, but special methods have been developed to handle this sum efficiently, the Ewald method for three dimensionally periodic systems and the Parry method for two dimensionally periodic systems (see chapter 2). The ion charges $q_i$ and $q_j$ are generally assigned as the formal fully ionic charges. Although partial charges may be used for semi-ionic materials, this can lead to some uncertainty as to the most appropriate distribution of such charges. This is particularly evident if

the formation energies of defect reaction are required. In general it is found that models based on formal charges work well, even for compounds such as silicates where it is known that there is an appreciable covalent contribution to the bonding.

The short range interaction, $\phi_{ij}$, is used to describe the interaction between the electron clouds of neighbouring ions. At small separations the electron clouds overlap and the potential is highly repulsive. This is usually represented by an analytical function which expresses the potential energy in terms of ionic separation, the Born-Mayer expression is very popular [49, 50]

$$\phi_{ij}(r_i, r_j) = A_{ij} \exp(-|r_i - r_j|/\rho_{ij}) \tag{3.2}$$

where the parameters $A_{ij}$ and $\rho_{ij}$ are specific to the interaction and material. As the ionic separation increases the interaction may contain an attractive component arising from the effects of dispersion and covalency. This is taken into account in the Buckingham potential by the addition of a $C_{ij}/r^6$ attractive term to the expression above.

$$\phi_{ij}(r_i, r_j) = A_{ij} \exp(-|r_i - r_j|/\rho_{ij}) - C_{ij}/|r_i - r_j|^6 \tag{3.3}$$

Many other functional forms may be used to describe the short range interactions, such as the Lennard Jones potential or Morse potentials but all potentials used in this thesis were of the Buckingham form given above.

The inclusion of higher order terms than the pair wise or two-body interactions above has until recently been considered an unnecessary complication for ionic materials. However, the work of Sanders et al [51] and Price et al [52] on silicate minerals has shown that inclusion of further interaction terms is necessary to reproduce the crystal structures of these complex compounds. These three-body terms must be included to take into account the strongly directional nature of the bonding in such materials. This is achieved using a "bond bending potential" of the form

$$\phi_{ijk}(r_i, r_j, r_k) = \frac{1}{2} K_{ijk}(\theta - \theta_0)^2 \tag{3.4}$$

where $\theta_0$ is the equilibrium bond angle and $K_{ijk}$ is the harmonic bond force constant.

The method by which the potential parameters mentioned above are derived will be described later in this chapter but firstly, we shall describe methods by which ionic polarisability may be incorporated into the potential model.

## 3.2 Ionic Polarisability

The simplest type of potential models neglect ionic polarisability altogether. In other words the high frequency dielectric constant of the material is assumed to be unity. Clearly as lattice vibrations are strongly influenced by ionic polarisation [53, 54] this approach will place a major limitation on the ability of the model to reproduce the dynamical properties of ionic lattices. Also this approach will affect the calculated energies of charged defects as the polarising effect of such defects will be truncated.

Despite these limitations this rigid ion model is normally employed in molecular dynamics and Monte-Carlo simulations as inclusion of polarisability would make such calculations computationally very expensive. However, it is clear that in general some explicit representation of polarisability is necessary in the modeling of both lattice properties and defect energies. One of the earliest used and simplest models for achieving this is the point polarisable ion model.

### 3.2.1 Point Polarisable Ion Model

In this model the polarisability is introduced by allowing each point ion to develop a fixed point dipole moment, $m$, which in the presence of an electric field $E$ is given by

$$m = \alpha E \tag{3.5}$$

$\alpha$ being the polarisability. Hence the energy of the interacting dipole can be calculated. This model is acceptable for point ions or small molecules but unfortunately for lattices it is unsatisfactory because of its inability to allow the polarisability

to change with ion environment. Defect calculations using this model have been seen to underestimate defect energies by a substantial degree [55, 56]. This failure arises because the model fails to take into account the coupling between the short range interactions and the polarisation, a coupling which is obvious when the physical origin of polarisation as a distortion of the electronic charge cloud is considered. Furthermore it is has been shown by Faux [57] that the model exhibits an instability when the distances between ions become small which may be expected to occur in defect calculations. As the two ions approach each other, if the separation becomes less than a critical value $r_{crit}$, the interaction energy becomes divergent

$$r_{crit} = (4\alpha_i\alpha_j)^{\frac{1}{6}} \tag{3.6}$$

These problems are overcome by means of the shell model, which gives a considerably improved model of polarisability by treating the electron clouds of the ions as separate species.

### 3.2.2 Shell Model

The shell model, originally developed by Dick and Overhauser [58], uses a simple mechanical model of an ion. Each ion is considered to be made up of a core in which the mass of the ion is concentrated, charge $X$, which is coupled to a massless shell, charge $Y$, via a harmonic spring of force constant $K$. The polarisation of the ion is described as a displacement of the shell relative to the core. The interaction between the core and shell for an ion $i$ can therefore be expressed as

$$\phi(r_i) = K_i r_i^2 \tag{3.7}$$

and the free ion polarisability $\alpha$ may be written as

$$\alpha = \frac{Y_i^2}{K_i + r_i} \tag{3.8}$$

where $K_i >> r_i$. The short range interactions are taken to act between shells and thus the coupling between the short range potential and the polarisation is achieved.

This model has been used with great success in the calculation of the elastic, dielectric and lattice dynamical properties of a large number of ionic materials. It has the disadvantage of introducing two additional potential parameters, but this disadvantage is greatly outweighed by the increased reliability achieved in calculations using this model. For an in-depth discussion of polarisability and its effect on defect calculations see reference [59] by Catlow and Mackrodt.

### 3.3 Derivation of potential parameters.

The parameters in the short range potential energy function can be obtained either by fitting to known crystal properties or by direct calculation using approximate quantum mechanical techniques. However there is no method at present available to calculate the shell model parameters $Y$ and $K$, these must be obtained by empirical fitting methods. The derived potential parameters can therefore be split into two families, the non-empirical family where the short range parameters can be calculated directly and the shell and other parameters are obtained by fitting to crystal properties, and the empirical family where all parameters are obtained by fitting to crystal properties.

#### 3.3.1 Non-empirical potentials

These potentials cannot easily be obtained directly from full quantum mechanical calculations but can be extracted from approximate formulations. The most widely used method is based on the density functional treatment of a uniform electron gas [60, 61, 62]. In this approach the total energy of the system is written as

$$E_{total} = E_{elec} + E_{ke} + E_{ex} + E_{cor} \tag{3.9}$$

where $E_{elec}$ is the electrostatic energy, $E_{ke}$ is the kinetic energy, $E_{ex}$ is the exchange energy, and $E_{cor}$ is the short range correlation energy in the region of electron density overlap. Each component is expressed in terms of the electron densities which can be obtained using various methods including Hartree-Fock

wave functions. The terms in equation (3.9) are then calculated yielding the interaction energy at a specific ionic separation and by assuming a given charge the short range energy can be extracted. This is repeated for a range of inter-ionic separations and the potential parameters are obtained by fitting to the functional form required. Methods of calculating the terms in equation (3.9) are review by Catlow, Dixon and Mackrodt in reference [53]. It has been stressed by Mackrodt and coworkers [63] that the wave functions used in such calculations for ionic materials should be "crystal adapted". That is, the solving of the equations should take place in the Madelung potential appropriate to the lattice under investigation. This is particularly important for anions because of the diffuse nature of their wave functions.

This non-empirical approach had two main advantages over the empirical approach described in the next section. Firstly the parameters can be determined for a large range of inter-ionic separations. This is useful when calculating interstitial or migration energies where the inter-ionic separations achieved are often markedly different from those in the perfect lattice. Secondly, empirical methods depend on the availability of crystal data, which may not be available for the desired system.

### 3.3.2 Empirical potentials

Given a set of potential parameters it is possible to calculate a range of crystal properties. These include the elastic, dielectric and piezo-electric constants as well as the phonon dispersion curves. In order to derive a set of potential parameters a trial set of parameters are used to calculate such properties. These are then compared to the experimentally determined values. The parameters can then be adjusted iteratively using a least squares fitting procedure until the desired agreement with these properties is achieved. It should be noted that the parameters are fitted to properties such as the elastic and dielectric constants which do not rely directly on the interionic potential but on the first and second derivatives of the potential itself. Thus the derived parameters must describe not only the

potential energy correctly but also the variation of this energy correctly, hence allowing the potential to be used at different interionic separations.

A reliable set of empirical potentials derived by Catlow and Lewis [50] were available for the materials covered in this thesis and therefore were used. These potentials have been shown to be more reliable than non-empirical potentials when used to model ternary oxides [50] such as the spinels covered in this thesis. This has been attributed to an extra component of flexibility in empirical potentials over calculated potentials [64]. Deficiencies in the potential model may in part be compensated by the fitting procedure.

The potential parameters used throughout this thesis are given in tables 3.1 to 3.4. All these potentials take as their base a single set of $O^{2-} - O^{2-}$ short range parameters derived using a Hartree-Fock method [65], table 3.1. For each cation-anion interaction therefore a separate and different set of shell parameters for the anion is required. These are given along with the short range and shell parameters for the cations in table 3.2. In the case of the silicate forsterite $Mg_2SiO_4$ a three body potential has been found to be necessary, we therefore used the parameters derived by Sanders et al [51] given in tables 3.3 and 3.4.

| Interaction | $A$ (eV) | $\rho$ (Å) | $C$ (eVÅ$^6$) |
|---|---|---|---|
| $O^{2-} - O^{2-}$ | 22764.0 | 0.149 | 27.88 |

Table 3.1: Potential parameters for the Oxygen–Oxygen short range interaction [65].

| Interaction | $A$ (eV) | $\rho$ (Å) | $C$ (eVÅ$^6$) | $Y^+$ ($\|e\|$) | $K^+$ (eVÅ$^{-2}$) | $Y^-$ ($\|e\|$) | $K^-$ (eVÅ$^{-2}$) |
|---|---|---|---|---|---|---|---|
| $Al^{3+} - O^{2-}$ | 1114.9 | 0.3118 | - | 3.0 | 99999 | -2.21 | 27.29 |
| $Cr^{3+} - O^{2-}$ | 1734.1 | 0.3010 | - | 0.97 | 67.0 | -2.21 | 27.29 |
| $Fe^{2+} - O^{2-}$ | 694.1 | 0.3399 | - | 2.0 | 10.92 | -2.15 | 17.75 |
| $Fe^{3+} - O^{2-}$ | 1102.4 | 0.3299 | - | 4.97 | 304.7 | -2.21 | 27.29 |
| $Mg^{2+} - O^{2-}$ | 821.6 | 0.3242 | - | 2.0 | 99999 | -2.0 | 15.74 |
| $Ti^{4+} - O^{2-}$ | 754.2 | 0.3879 | - | 2.89 | 37.2‡ | -2.53 | 86.4‡ |
| $Y^{3+} - O^{2-}$ | 1345.1 | 0.3491 | - | 3.0 | 99999 | -2.21 | 27.29 |

Table 3.2: Potential parameters for Cation–Oxygen interactions [50]. ‡Additional quartic constant of $1.1 \times 10^5$ eVÅ$^{-5}$ [66].

| Interaction | $A$ (eV) | $\rho$ (Å) | $C$ (eVÅ$^6$) | $Y^+$ ($\|e\|$) | $K^+$ (eVÅ$^{-2}$) | $Y^-$ ($\|e\|$) | $K^-$ (eVÅ$^{-2}$) |
|---|---|---|---|---|---|---|---|
| $Mg^{2+} - O^{2-}$ | 1428.50 | 0.29453 | - | 2.0 | 99999 | -2.84819 | 74.92038 |
| $Si^{4+} - O^{2-}$ | 1283.90734 | 0.32052 | 10.66158 | 4.0 | 99999 | -2.84819 | 74.92038 |

Table 3.3: Two-Body potential parameters for Cation–Oxygen interactions in forsterite $Mg_2SiO_4$ [51].

| Interaction | $K$ (eVrad$^{-2}$) | $\theta_0$ |
|---|---|---|
| $O^{2-} - Si^{4+} - O^{2-}$ | 2.09724 | 109.47° |

Table 3.4: Three-Body potential parameters for forsterite $Mg_2SiO_4$ [51].

## Chapter 4

## The surface energies of oxides

In this chapter we shall investigate the energies and structures of the low index surfaces of a range of ceramic oxides. We shall start by considering one of the highly symmetric rocksalt structure oxides, FeO, then go on to consider the surfaces of more complex structures. These include rutile, a normal and inverse spinel, and finally forsterite a member of the olivine group of minerals.

In this work we shall stress the importance of surface relaxation and its effect on surface structure and the relative stability of oxide surfaces. Although as mentioned in the introduction to this thesis new experimental techniques allow us to determine the structures and composition of many surfaces, the experimental measurement of surface energies is as yet unreliable with the many techniques employed giving inconsistent and variable results. Therefore direct comparison between experimental and calculated surface energies is impractical, instead we shall use an indirect method by comparing a predicted equilibrium morphology with experimentally grown crystals.

### 4.1 Surface Methodology

Since the times of Young [67] and Laplace [68] it has been convenient to treat the surface energy of liquids in terms of the surface tension, that is the energy required to expand a surface. This model cannot be applied to solids which do not flow without work and which may contain surface stresses that are not equivalent to surface tension. For solids it is much simpler and more general to consider the specific surface energy directly, that is the energy require to form unit area of surface. Following Rhee [31] we may evaluate the surface energy of a crystal face as follows

Let $W$ be the total amount of energy required to split a crystal into particles (atoms, ions or molecules) and separate them to an infinite distance so that all

interactions between them cease. Now if we firstly divide the crystal into two fragments about some plane, and let $W_1$ be the energy required to split and separate the first fragment and $W_2$ the energy for the second fragment. We may naively expect that

$$W = W_1 + W_2 \tag{4.1}$$

However when a crystal is actually cleaved into two fragments which are then separated to infinity, a certain amount of work, $U_s'$, must be expended to form the two new surfaces, each with area $A$. The total energy for splitting the two fragments into particles will now be smaller by an amount $U_s'$ [69], therefore

$$W = W_1 + W_2 - U_s' + U_s'' \tag{4.2}$$

where $U_s''$ represents a reduction in the energy of the two parts due to relaxation of the surface particles to a new equilibrium position. Thus the surface energy at 0 K will be $U_s = U_s' - U_s''$. If both surfaces formed are identical then the surface specific energy, $\gamma$, of the dividing plane will be

$$\gamma = U_s/(2A) \tag{4.3}$$

The surface energy $U_s$ here represents the work required for a reversible and isothermal formation of the surface layer.

The above description of the surface specific energy is easily translated into two MIDAS calculations as illustrated in figure 4.1. The starting point for these calculations is a bulk energy minimised structure This was calculated in this work using the THBREL code developed by Leslie [70]. In the first calculation we use two MIDAS blocks placed together so that there is no defect or mismatch at the interface. The energy of region I, $E_{bulk}$, will correspond to a piece of bulk crystal, this is equivalent to $W$ above. In the second calculation, we use one of the blocks from the bulk calculation. This now has a region I half the size of region I in the bulk calculation and also has a surface. The choice of the surface termination plane is based on the criteria we discussed in chapter 2, that is such that there is

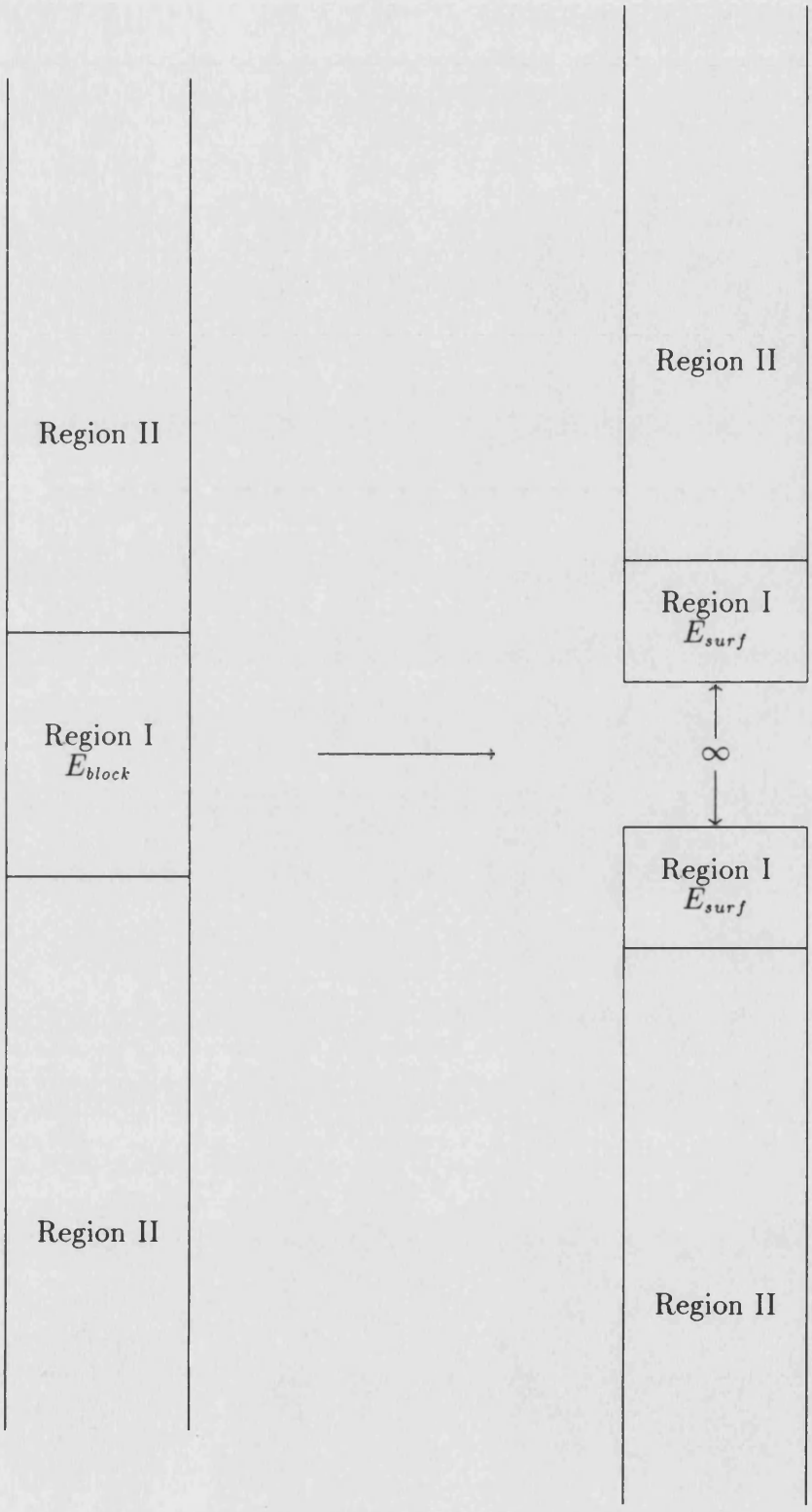


Figure 4.1: Schematic representation of the MIDAS calculations required to calculated the surface energy of a plane.

no net dipole perpendicular to the surface. This means that in most cases the split occurs about a plane of symmetry and thus both of the surfaces formed will be identical. The energy of region I now becomes $E_{surf}$ and corresponds to $W_1 - U_s'$ before energy minimisation or $W_1 - U_s' + U_s''$ after energy minimisation. If the size of the two blocks used to calculate $E_{bulk}$ are identical then the surface energy is simply

$$U_s = E_{block} - 2E_{surf} \tag{4.4}$$

and if the area of the MIDAS block is $A$ the surface specific energy will be given by

$$\gamma = \frac{E_{block} - 2E_{surf}}{2A} \tag{4.5}$$

The energies obtained from MIDAS are static energies, that is they do not include vibrational components and, therefore, the surface specific energy obtained will be that expected at zero temperature neglecting zero point vibrations.

As mentioned above experimental attempts to measure the surface energy have been many and varied. Methods based on fiber elongation [71], multiphase equilibrium [72], contact angle [73], crystal cleavage [74], heats of solution [75] and more recently the elasticity of particle assemblies [76] have all been used. Critical reviews of most of these methods have been given by Rhee [31] and Bikerman [77]. These methods have only been applied to a small sample of the many know oxides and even for this small sample they tend to give inconsistent results. For example the value reported in the literature for the surface energy vary from 0.085 $Jm^{-2}$ to 50 $Jm^{-2}$ for $Al_2O_3$ and from 0.15 $Jm^{-2}$ to 3.5 $Jm^{-2}$ for MgO [78]. Therefore, direct comparison between the calculated and experimentally measured surface energies is not feasible. However it has been shown by Wulff [32] that the equilibrium morphology adopted by a crystal is dependent on the relative stabilities of the crystal surfaces. This allows us to make predictions of the crystal habit from our calculated surface energies which we can then compare with experimentally grown crystals.

## 4.2 The equilibrium form of a crystal – Wulff Theorem

Gibbs in 1878 [79] first proposed that the equilibrium form of a crystal should, for a given volume, possess minimal total surface energy. That is

$$E_{surface} = \sum_i \gamma_i O_i = \text{minimum for constant volume} \tag{4.6}$$

where $\gamma_i$ and $O_i$ are the specific surface energy and surface area of the $i^{th}$ crystallographic face. Wulff [32], starting from the Gibbs proposal, suggested that the shape thus defined would be such that $h_i$, the face normal vector from a point within the crystal (figure 4.2), would be proportional to the specific surface energy of that face $\gamma_i$, or that

$$h_i = \lambda \gamma_i \tag{4.7}$$

where $\lambda$ is a constant that only depends on the absolute size of the crystal. This theorem could not initially be proved but later several different proofs were obtained by Hilton [80], Liebman [81] and von Laue [82] using geometric arguments and by Volmer [83] and Stranski [84] using thermodynamic arguments. Here we shall give a proof taken from Strickland-Constable [85] based on the von Laue approach.

If $V_c$ is the total volume of a crystal, then

$$V_c = \frac{1}{3} \sum_i h_i O_i \tag{4.8}$$

For a small change of crystal shape at constant volume we can see that

$$\partial V_c = \frac{1}{3} \partial \sum_i h_i O_i = 0 \tag{4.9}$$

or that

$$\sum_i h_i \partial O_i + \sum_i O_i \partial h_i = 0 \tag{4.10}$$

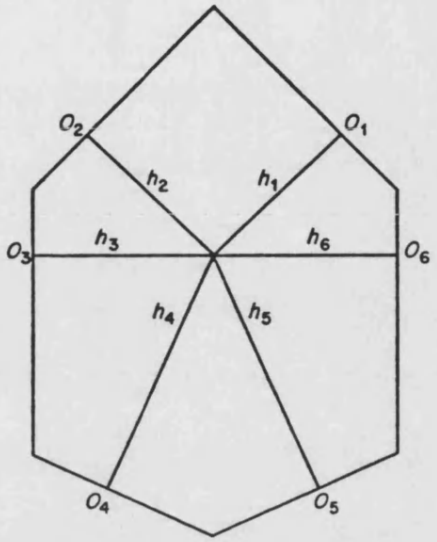


Figure 4.2: Two dimensional representation of a crystal. $h_1$, $h_2$ $\cdots$ $h_i$ are the lengths of the normals a point within the crystal to each face. $O_1$, $O_2$ $\cdots$ $O_i$ are the areas of the faces.

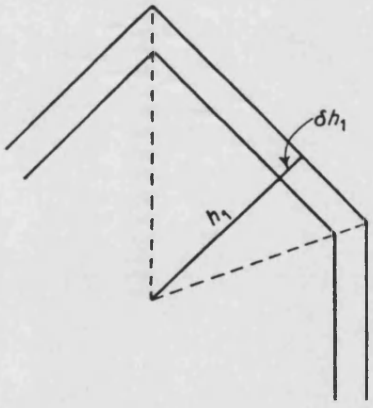


Figure 4.3: Growth of two dimensional crystal by addition of layers of thickness $\partial h$ on each face.

It is geometrically obvious (figure 4.3) that in general

$$\partial V_c = \sum_i O_i \partial h_i \tag{4.11}$$

and therefore when $\partial V_c = 0$

$$\sum_i O_i \partial h_i = 0 \tag{4.12}$$

and

$$\sum_i h_i \partial O_i = 0 \tag{4.13}$$

Now from equation (4.6) we know that

$$\sum_i \gamma_i \partial O_i = 0 \tag{4.14}$$

therefore if we multiply this equation by $\lambda$ and subtracting equation (4.13) we get

$$\sum_i (h_i - \lambda\gamma_i)\partial O_i = 0 \tag{4.15}$$

We cannot deduce Wulff's theorem directly from this equation because the $\partial O_i$ in equation (4.15) are not independent variables. However, we have not yet specified the position of the point within the crystal from which the $h_i$ are drawn. If the position of this point is defined by the intersection of three non-parallel planes, the values of three of the $h_i$ can be chosen arbitrarily and such that $h_1 = \lambda\gamma_1$, $h_2 = \lambda\gamma_2$ and $h_3 = \lambda\gamma_3$. The first three coefficients in equation (4.15) will now be zero and therefore the remaining variations $\partial A_4, \partial A_5 \cdots$ can now be considered arbitrary and accordingly all the coefficients in (4.15) will have to be zero, i.e.

$$h_i - \lambda\gamma_i = 0 \tag{4.16}$$

the Wulff condition for the equilibrium shape of crystals. This expression will only hold for ideal crystals grown with all faces in constant equilibrium with each other. This is very difficult to achieve in practice and few real equilibrium forms

have been produced [86]. However for small crystals where rearrangement of the crystal at each stage of the growth process is possible due to the small distances over which material has to travel will have forms close to equilibrium. Also we would expect some relationship between the equilibrium form and growth form if kinetic effects do not dominate.

Using the above expression it is a simple matter to generate a crystal morphology from a set of surface energies. Dowty developed a computer code to achieve this and in turn based on his published details [87] we have developed our own code based on his methods. The morphologies presented in this thesis were calculated using this code.

### 4.3 The surfaces of Wüstite – FeO

Wüstite, FeO, is one of the many divalent metal oxides such as MgO, CaO, NiO and CoO which adopt a face centered cubic rocksalt structured lattice. FeO itself is only thermodynamically stable with respect to Fe and $Fe_3O_4$ above 570° C [88], the crystalline substance being obtained by rapid quenching from this temperature. Purely stoichiometric FeO can be prepared only under extreme conditions (1050 K and 50 katm [89]). Normally prepared wüstite is iron deficient, $Fe_{1-x}O$, with large variations in $x$. This deviation from stoichiometry results from vacancies on cation sites and trivalent cations interstitials on some tetrahedral sites [90]. Due to the complex nature of this defective structure and in order to simplify our calculations, here we shall only consider the stoichiometric compound.

The stacking sequences perpendicular to the three lowest index surfaces of FeO are illustrated in figure 4.4. We can see that as the index of the surface increases the interplanar spacing decreases. This is accompanied by the expected increase in the area of the surface unit cell. The actually stacking sequences are very simple and choice of surface terminating plane presents no difficulty. The {100} and {110} surfaces both have a single neutral plane as their repeat unit perpendicular to the surface and therefore we have no choice to make. In the

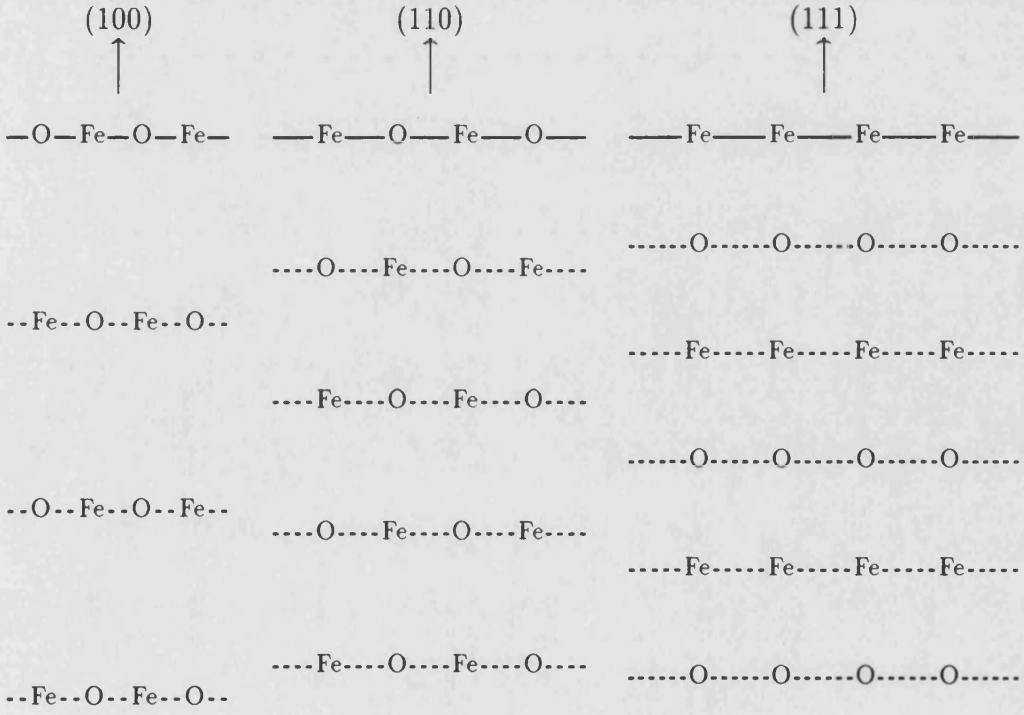


Figure 4.4: The stacking sequences for the low index surfaces of FeO.

| Surface | Unrelaxed Energy ($Jm^{-2}$) | Relaxed Energy ($Jm^{-2}$) |
|---|---|---|
| {100} | 0.941 | 0.936 |
| {110} | 2.944 | 2.491 |
| {111} anion | 7.419 | 2.965 |
| {111} cation | 7.346 | 2.988 |

Table 4.1: Calculated surface energies for the low index surfaces of FeO.

case of the {111} surface the repeat unit is made up of a pair of planes, one consisting of purely anions and the other containing only cations. This unit has a net dipole moment perpendicular to the surface and as we discussed in chapter 2 a neutral block made up of such units will result in a infinite surface energy. We may however remove this dipole and obtain a finite surface energy by halving the charge of the terminating plane [45]. In terms of our surface energy calculation this is achieved by splitting the crystal block through a plane (which must be a mirror plane in the stacking sequence) of ions such that ions of that plane are split half and half between the two surfaces formed. The termination of each surface will then consist half of ions and half of ion vacancies. For the FeO {111} surface both the anion and cation planes are mirror planes and therefore we must consider both possible surface terminations.

The calculated surface energies for these three planes are given in table 4.1. The energies both before and after energy minimisation have been included. The unrelaxed surface energy corresponds to a strict bulk termination and is based on the energy before energy minimisation. The relaxed surface energy, however, is based on the energy of a region I after it has been minimised to zero strain using the methods described in chapter 2. In the case of the {111} surfaces the energies of all possible arrangements of the two surface vacancies were calculated but no variation in the surface energy was found.

We can see from these results that we predict the {100} surface to be by far the most stable surface; the other surfaces are between two and three times less stable. The degree of relaxation at the {100} surface is very small when compared

to the other surfaces considered. This is due to the dense packing of the ions in the {100} direction. The effect on the surface structure of the {100} surface of this relaxation are also small. The surface as a whole does not contract or expand but the ions in the surface plane and the plane below rumple, that is the cations and anions relax in opposite directions. This rumpling effects are illustrated in figure 4.5. The cations in the surface plane relax into the bulk whereas the anions relax outwards whilst polarising towards the cations. The overall displacements are very small being less than 1% of the bulk spacing. The first plane below the surface also undergoes some rumpling but in the opposite direction to the plane above and to a much lesser degree. All these effects are perpendicular to the surface, no movement in the surface plane is observed. Below the first plane the structure remains totally unchanged. Overall, the changes could easily be neglected and the {100} surface treated as a simple bulk termination.

For the {110} and {111} surfaces, however, the amounts of relaxation are much greater, the surface energies changing by 19% and 60% respectively. These larger changes in surface energy reflect larger relaxation effects that extend deeper into the bulk. The relaxed surface structure of the {110} surface is illustrated in figure 4.6. We again see rumpling of the ions on the surface plane and below, here the rumpling is much more exaggerated and extends to four planes below the surface. In addition to the rumpling we see changes in the interplanar spacings with the surface as a whole contracts slightly by 0.13Å, and the distance between the planes alternately contracting. These effects continue until the fifth plane below the surface beyond which the structure maintains its original arrangement. Again all relaxation effects take place perpendicular to the surface, no movement in the plane of the surface is observed. The relaxation of the {111} surfaces followed the same trends as the {110} surface. In the case of the {111}o surface the contraction was 0.47Å and the structure was effected to a depth of six planes.

These results show good agreement with similar calculations carried out by Mackrodt on a range of rocksalt structured oxides [91]. In all cases Mackrodt

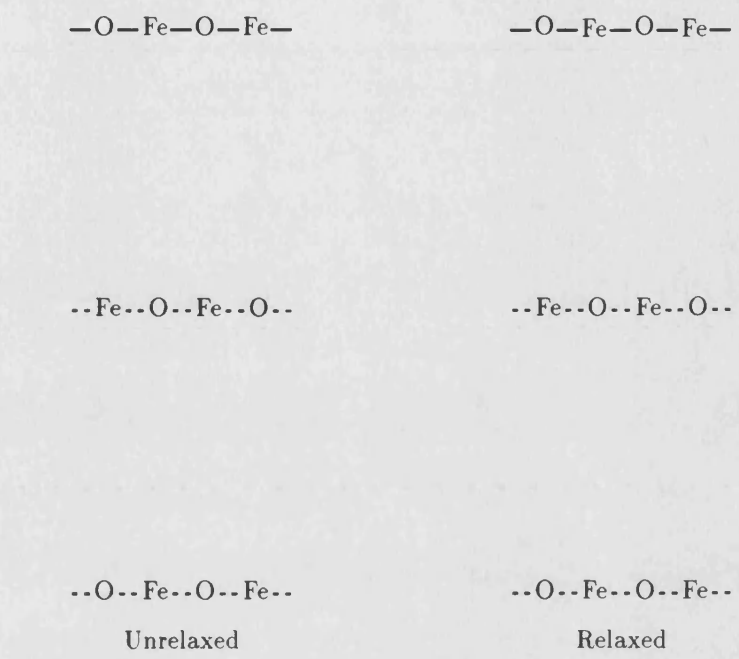


Figure 4.5: Surface relaxation of the {100} surface of FeO. Surface rumpling shown to scale.

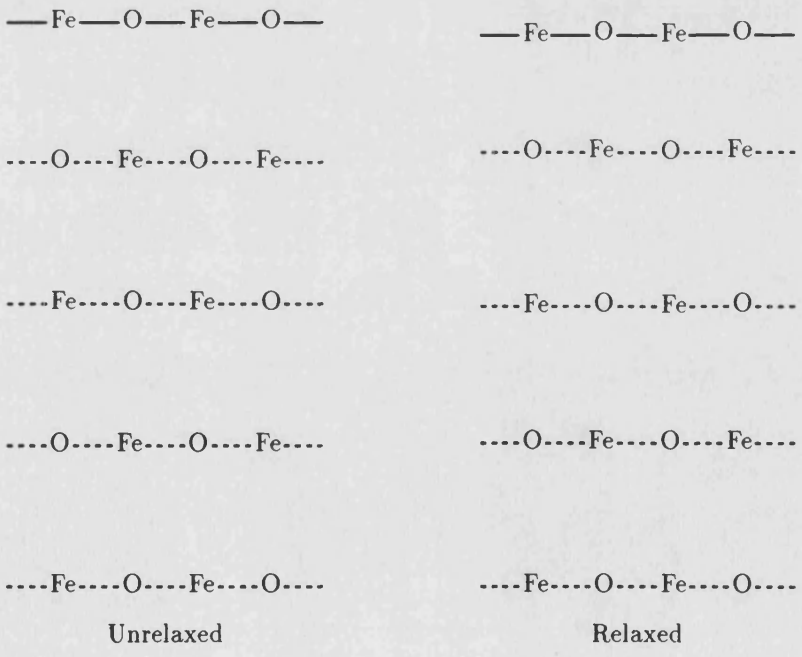


Figure 4.6: Surface relaxation of the {110} surface of FeO.

found the {100} surface to be most stable with energies ranging from 0.65 $Jm^{-2}$ for SrO to 1.07 $Jm^{-2}$ for MgO. As above, surface rumpling was the only relaxation affect observed with all displacements being below 3% of the bulk spacing. The {110} surfaces energies ranged between 1.5 and 3 times the energy of the corresponding {100} surface. These energy differences between the planes are in line with experimental observation where the {100} has been found to be by far the most stable surface [92]. Indeed most rocksalt structured oxides including FeO [93] cleave well along this plane. The stability of the {100} surface is again reflected in the predicted equilibrium morphology with the other surfaces playing no part which results in a simple cubic habit as is the normal crystalline form for many compounds with this type of structure.

The structure of {100} surface of several rocksalt oxides have also been studied using LEED. In line with our observations these experiments show a simple pattern with no reconstruction parallel to the surface or fractional order spots being observed [94]. Similar LEED patterns have also been reported for FeO formed on the surface of iron metal exposed to oxygen [95], although more recently some doubt has been expressed as to the nature of the compound actually being observed [96]. More detailed studies of the {100} surface of MgO have also given some evidence for surface rumpling [97, 98]. Overall we can conclude that simulations of the low index surface of rocksalt structured oxides including the calculations given here show good agreement with experiment. This in part may be due to the simple nature of these surface and the negligible amount of relaxation observed at the {100} surface. We shall see in the remainder of this thesis that these small amounts of surface relaxation are the exception rather than the rule.

## 4.4 The surfaces of Rutile – $TiO_2$

Rutile is one of the three crystalline forms of titania, $TiO_2$, the other forms being Anatase and Brookite. The rutile structure is tetragonal [99] with each

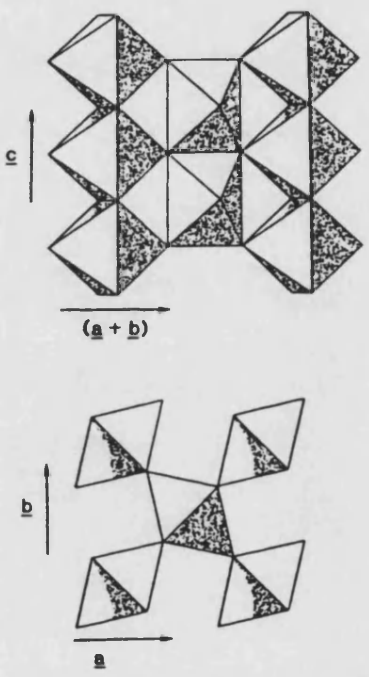


Figure 4.7: The structure of rutile $TiO_2$ [100]

$Ti^{4+}$ ion surrounded by a slightly distorted octahedra of oxide anions and each oxide anion surrounded by three cations which lye in a plane at the corners of an approximately equilateral triangle, figure 4.7. Half the octahedral sites surrounded by anions are empty, this gives rise to open "channels" parallel to the $c$ axis which facilitate the diffusion of H, Li and other small atoms along this axis [101]. Reproducing this structure and its anisotropic dielectric constants using a two body potential has been found to be extremely difficult [100]. The potential we shall use here is due to Catlow, Freeman and Royle [66]. This two body potential reproduces the physical properties accurately but gives a $c/a$ ratio too large by approximately 7%.

The lower symmetry of the rutile structure leads to a larger number of low index surfaces than for the cubic oxides. The stacking sequences perpendicular to the five lowest are shown in figure 4.8. We see that the stacking sequences are much more complex than in the case of FeO and that the {001} plane is the only surface consisting solely of neutral planes. For each of the remaining surfaces a non-dipolar repeat exists and the sequences shown in figure 4.8 are terminated with these repeats. However, in the case of the {111} surface the situation becomes is a bit more complicated. The smallest repeat for this surface consists of the sequence of planes $TiO_2$-O-Ti-O, this at first glance appears dipolar due to its lack of symmetry. However, on closer inspection we note that the first plane, $TiO_2$, is neutral and therefore as the O-Ti-O sequence is symmetric the sequence as a whole is non-dipolar. For the {111} direction therefore we can have two possible non-dipolar surface terminations, either a $TiO_2$ terminating layer as shown in figure 4.8, or a O terminating layer at the top of a O-Ti-O unit. As our method of calculating the surface energy relies on the fact that when we cleave the crystal we obtain two identical surfaces we shall not be able to obtain a specific energy for either of these terminations, however we can obtain an average of the two surface energies.

The calculated surface energies for these low index planes are given in table 4.2. We can see from these results that in the case of rutile all surfaces undergo

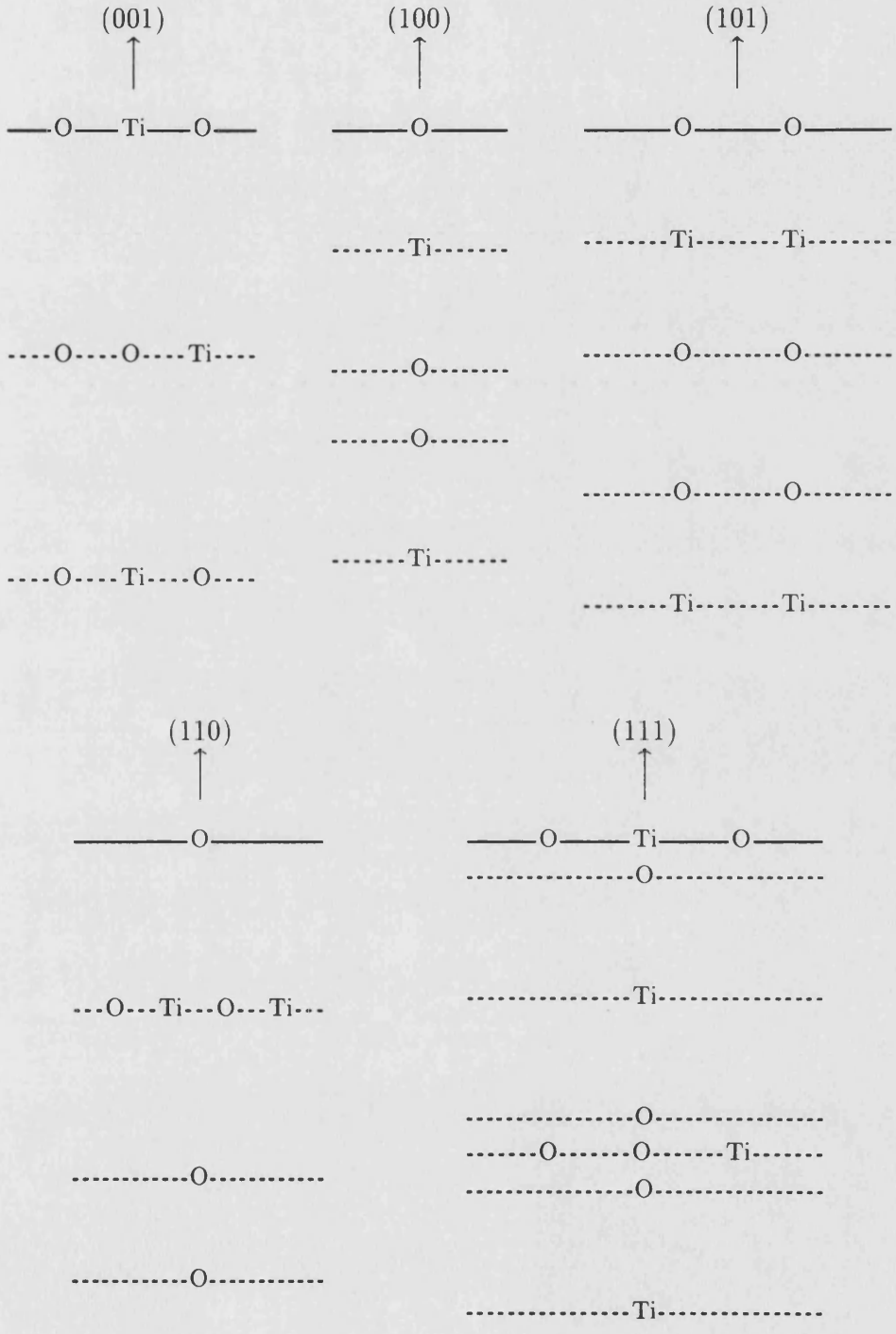


Figure 4.8: The stacking sequences for the low index surfaces of rutile $TiO_2$.

| Surface | Unrelaxed Energy ($Jm^{-2}$) | Relaxed Energy ($Jm^{-2}$) |
|---|---|---|
| {001} | 4.66 | 2.09 |
| {100} | 3.60 | 1.33 |
| {101} | 2.93 | 1.30 |
| {110} | 3.29 | 0.99 |
| {111} average | 7.67 | 1.05 |

Table 4.2: Calculated surface energies for the low index surfaces of rutile $TiO_2$.

significant relaxation and that the degree of relaxation is surface specific. The amounts of relaxations are large in comparison with those seen in FeO ranging from a 55% reduction for the {001} surface energy to a 86% reduction for the case of the {111} surfaces. As a result of these varying amounts of relaxation the order of stability of surfaces before and after relaxation are different. The order before relaxation is

$$\{101\} < \{110\} < \{100\} < \{001\} < \{111\}$$

which upon relaxation becomes

$$\{110\} < \{111\} < \{101\} < \{100\} < \{001\}$$

This change in the order of stability will have a large effect on the predicted equilibrium morphology as we shall see later. We note that before relaxation we predict the {101} surface to be the most stable, however, after relaxation the {110} surface becomes the most stable. This is in line with the generally accepted opinion that the {110} surfaces of rutile structured oxides are the most stable [92].

The effect of the large changes in surface energy on the structures of the {110} and {100} surfaces are illustrated in figures 4.9 to 4.12. It can be seen from these figures that these large energy changes are the result of small changes in structure. The effect on the stacking sequence perpendicular to the {110} surface is illustrated in figure 4.9. The surface as a whole contracts slightly by 0.12Å, with the interlayer spacings near to the surface shrinking. The largest noticeable

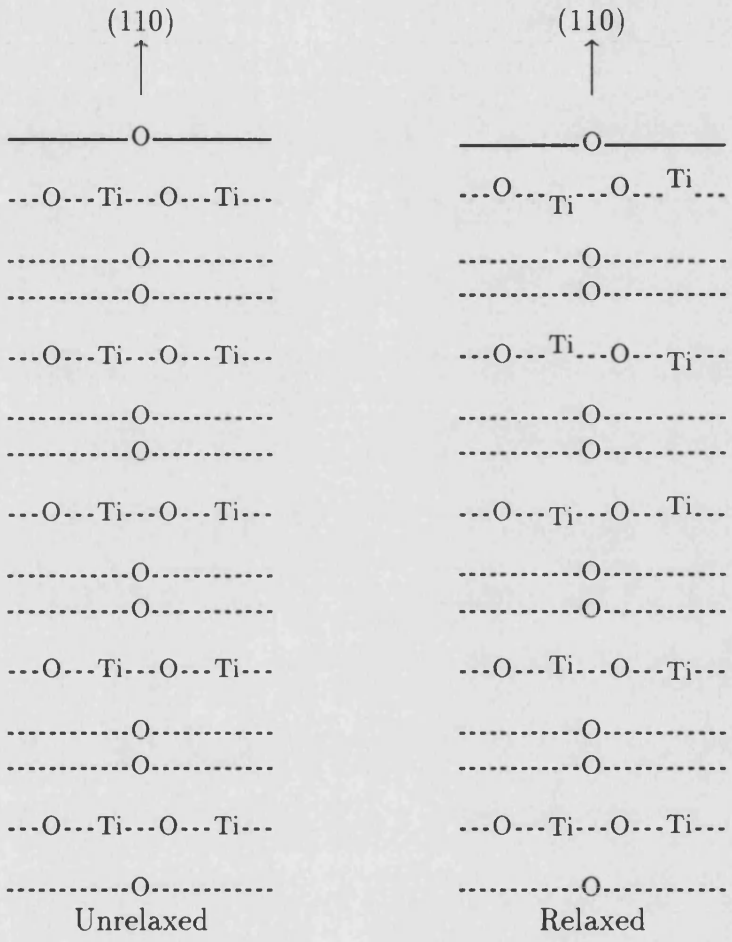


Figure 4.9: Surface relaxation perpendicular to the {110} surface of rutile $TiO_2$.

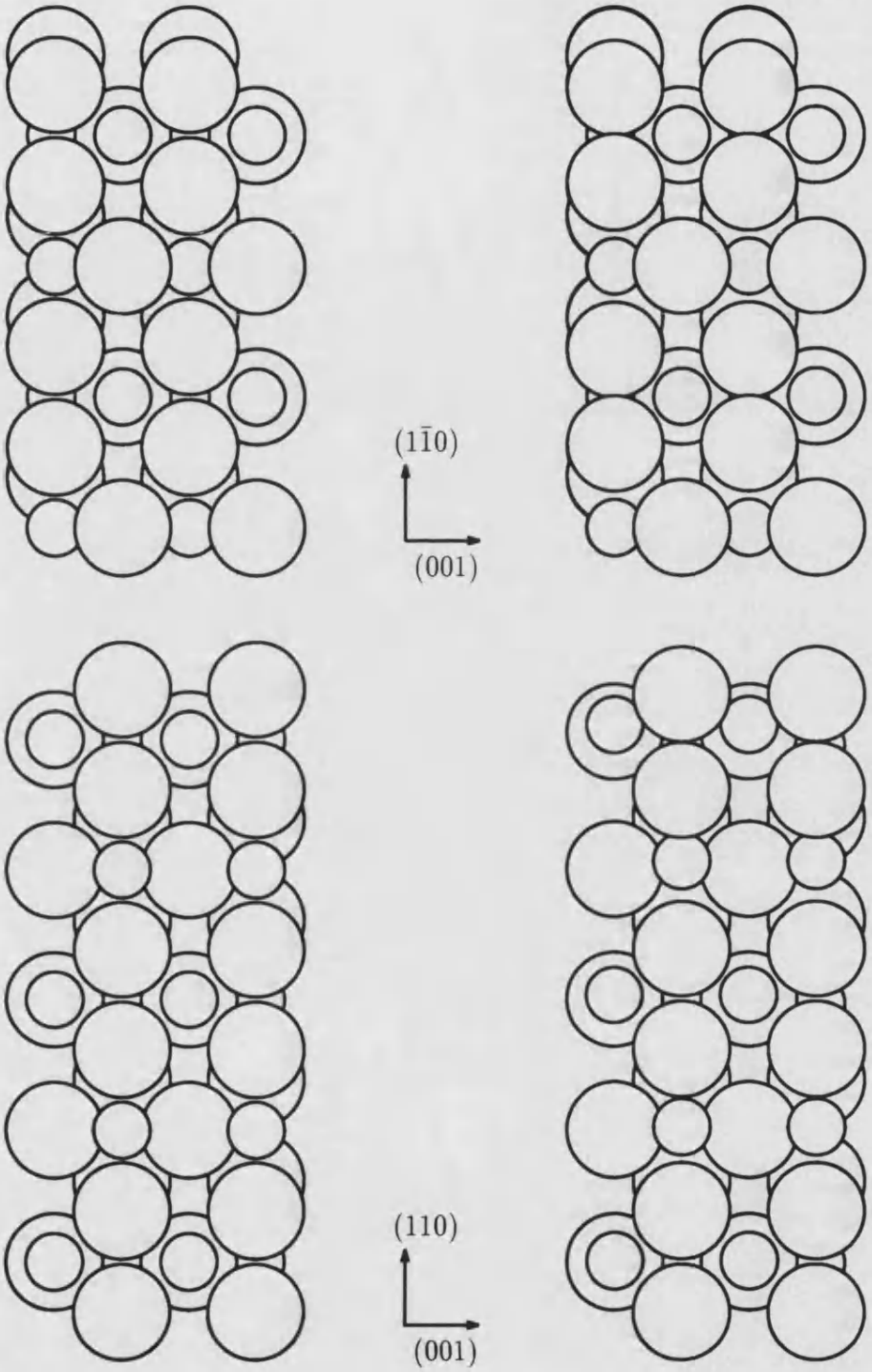


Figure 4.10: Surface relaxation of the {110} surface of rutile $TiO_2$. Top view looking down on surface. Bottom view perpendicular to surface. Surface unit cell scaled $2 \times 2$.

effect occurs within the cation lattice. On each layer containing cations one moves towards the surface whilst the other relaxes into the bulk. This is not surprising if we examine the structure of the surface at an ionic scale, figure 4.10. Now we can see that the {110} surface does not terminate in close packed structure, but consists of rows of anions with large separations. The first layer below the surface can be seen to consists of alternate rows of 5-fold and 6-fold coordinate $Ti^{4+}$ cations (structures identical to this have been proposed by several authors [102, 103]). On relaxation the 6-fold ions relax upwards and the 5-fold ions (obscured in figure 4.10) move into the bulk. This is in line with the rumpling effects we saw with FeO in the previous section. The 5-fold coordinated cations are effectively at the surface so we would expect them to relax into the surface. The 6-fold coordinated cations can be considered to be one layer below the surface and so relax upwards. Below the surface layers the cations relax in the opposite direction to the cation directly above them. We effectively have columns of cations relaxing alternately into and out of the bulk. In addition to this cation movement we see some movement of the upper anions in the plane of the surface. These relaxation processes continue deep into the crystal, extending to 5 repeat units (15Å) below the surface.

The effects of relaxation on the structure of the {100} surface are much less pronounced than in the case of the {110} surface described above even though the change in surface energies are comparable. The {100} surface again shows a small contraction 0.01Å, figure 4.11, with several layer below the surface moving upwards towards the surface. The relaxation process is well illustrated in figure 4.12. The surface anions relax towards the exposed surface cation which in turn relaxes into the anions to the left, figure 4.12. The movement of the cation draws up the oxide ions from below and to the right. The overall result is to increase slightly the coordination of the $Ti^{4+}$ at the surface helping to shield this highly charged ion. The relaxation effects diminish rapidly below the surface and after 2 repeat units (6Å) there is no effect on the structure. Similar effects were observed

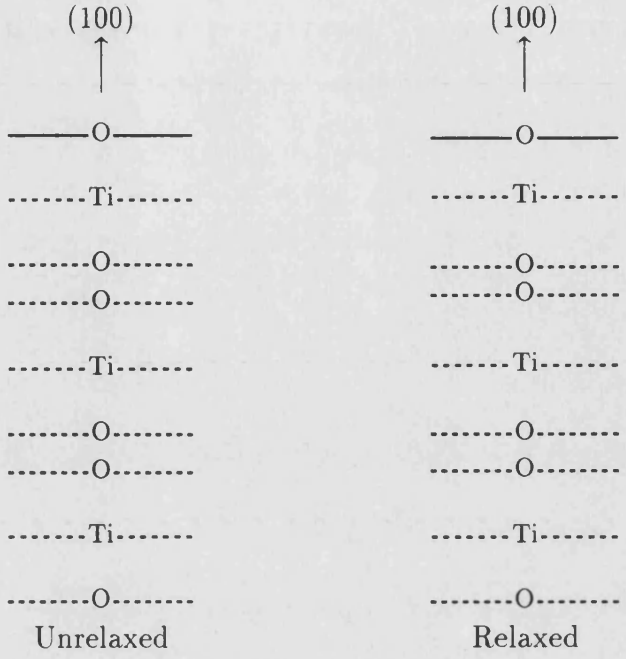


Figure 4.11: Surface relaxation perpendicular to the {100} surface of rutile $TiO_2$.

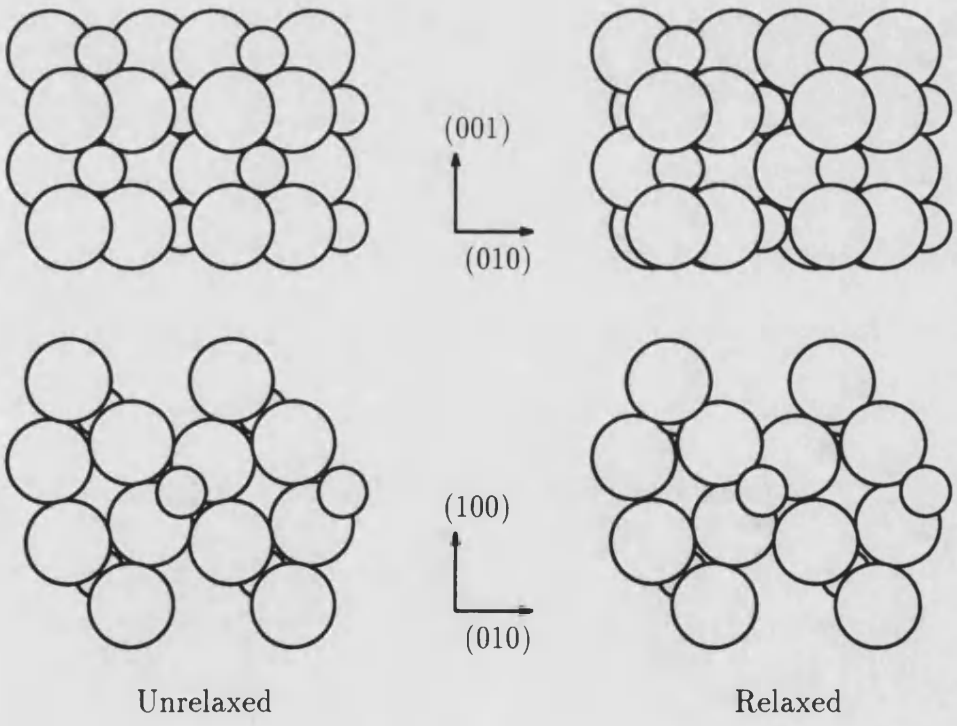


Figure 4.12: Surface relaxation of the {100} surface of rutile $TiO_2$. Top view looking down on surface. Bottom view perpendicular to surface. Surface unit cell scaled $2 \times 2$.

in the remaining low index surfaces with large amounts rumpling being seen in the case of the {001} surface. In all cases the $Ti^{4+}$ cation is seen to relax into the surface thus increasing its shielding. It should be noted that although the changes in surface energy on relaxation are large, the overall effects on the surface structure are very small, as we have seen with the {110} and {100} surfaces. Thus the structural changes brought about by relaxation would be difficult to detect experimentally.

The {110}, {100} and the {001} surfaces of rutile have all been studied experimentally using LEED. In line with our results above, the {110} surface shows a simple unreconstructed (1 × 1) pattern which remains stable over a wide range of conditions [104]. A (2 × 1) pattern has also been observed [105] for this surface but at present no explanation for this pattern has been found, the electronic spectrum for this surface being identical to that for the (1 × 1) pattern. For the {100} and {001} surfaces no simple unreconstructed patterns have been observed. The {100} surface shows with increasing temperature a (1 × 3), a (1 × 5) and a (1 × 7) pattern [104]. This apparently disagrees with our calculations which even using large surface unit cells did not show any change in surface energy or any surface reconstruction. However we note that the surfaces observed in the LEED experiment were found to be defective with an increase in the Ti/O ratio and some $Ti^{3+}$ being detected at the surface. Therefore the experimental {100} surface cannot be directly compared to the perfect surface used in our calculations. In the case of the {001} surface the reconstruction is even more extreme. This surface has been found to be unstable when annealed at high temperature where it facets into primarily {011} and {114} faces [106, 107]. We would not expect to observe such large changes in our calculations due to their constant area nature and the small surface areas considered. However we note that we do calculate the {001} surface to be the least stable, its calculated surface energy being over twice that calculated for the {110} surface.

In figure 4.13 we see the predicted equilibrium morphologies of rutile based on the calculated surface energies given in table 4.2. This figure illustrates well

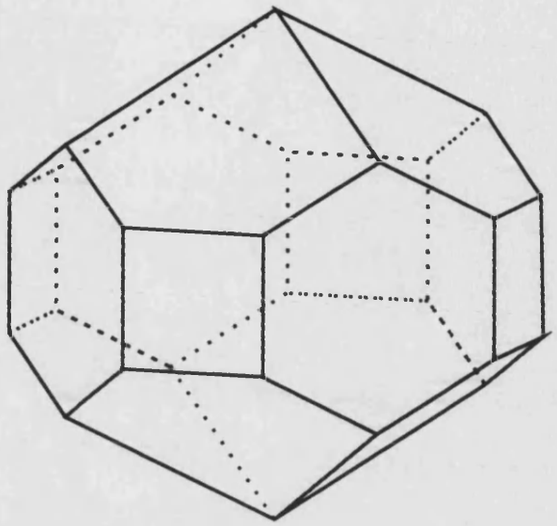

Unrelaxed

(001)

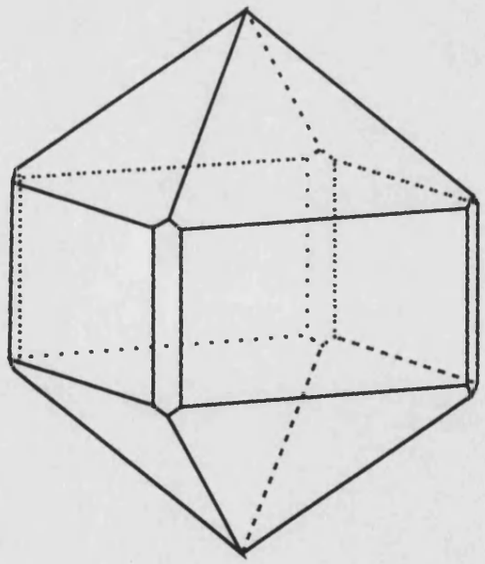

Relaxed

Figure 4.13: Predicted equilibrium morphologies for rutile $TiO_2$.

the large effects surface relaxation can have. For the unrelaxed surface energies (strict bulk terminations) we see a crystal prism consisting of {110} and {100} faces terminated by a pyramid of {101} faces. Upon relaxation we see a large reduction in the area of {100} faces with a corresponding increase in {110} faces. In addition the column is now terminated in {111} faces with no {101} present. Mineralogical crystals of rutile also show a prismatic nature [108] with the large {110} surface areas combined with small areas of {100} [108, 109, 110] similar to relaxed morphology in figure 4.13. However these crystals are more elongated and the prism is terminated in a mixture of {101} and {111} faces. This elongation can be attributed to the growth kinetics, whisker like crystals have been grown under special conditions [111]. The presence of the {101} faces may also be due to growth phenomena. Correns [112] make no mention of the {101} as a crystal faces for rutile but does mention it as a common twinning plane as do others [108, 109]. Furthermore mineralogical crystals contain impurities, most rutile samples contain some iron [110] which may effect surface energies by segregation. High purity rutile crystals have been grown which show no {101} faces [113] but did show some {101} twinning. In summary we can say that the morphology predicted by the relaxed surface energy shows good agreement with mineralogical and laboratory grown crystals although some doubt may still remain about the lack of {101} faces. This doubt could be removed if true equilibrium crystals were available but this is not the case. All experimental crystals mentioned here were relatively large and we could therefore expect some deviation from the equilibrium form.

## 4.5 The surfaces of Spinel – $MgAl_2O_4$

The mineral spinel, $MgAl_2O_4$, has given its name to the structure adopted by a large group of ternary oxides of the type $M^{II}M^{III}_2O_4$. The structure is based on an approximately cubic close packed array of oxide ions in which one eighth of the tetrahedral holes (of which there are two per anion) and one half of the octahedral

holes (of which there are one per anion) are occupied by cations. The distribution of the cations amongst these sites is dependent on the cations involved. Spinel itself adopts the so called *normal* arrangement with the $Mg^{2+}$ ions occupying the tetrahedral sites and $Al^{3+}$ ion occupying the octahedral sites. This contrasts with the *inverse* arrangement where half the trivalent cations occupy the tetrahedral sites and the remaining trivalent and divalent cations occupy the octahedral sites. This inverse arrangement is adopted by Magnetite, $Fe_3O_4$, which we shall consider in the next section. The full unit cell for this structure contains 32 oxide ions and 24 cations and is face centered cubic. In the calculations presented here the high symmetry of this lattice was utilised by using a reduced unit cell containing one quarter of the ions in the full unit cell. Use of this smaller unit cell helps to reduce the amount of computer resources required for each of the large number of energy calculations.

As with FeO we shall consider the three low index planes of cubic structures, that is the {100}, {110} and {111} surfaces. The stacking sequences perpendicular to the surface for these three planes are given in figure 4.14. A major difference with the materials discussed previously in that all three of these sequences have dipolar repeats. Therefore, as with the {111} surface of FeO, we have two possible terminations for each direction. These are marked as *a* or *b* in figure 4.14. Whilst considering these surfaces it became apparent that, unlike the {111} surface of FeO, the calculated surface energies were dependent on the arrangement of the surface vacancies used to remove the surface dipole. Due to this dependency and the fact that some surface terminations contain an odd number of ions, the surface unit cell was scaled to allow a greater number of arrangements to be considered. However to keep the number of calculations to a minimum this scaling was restricted to a doubling of the surface unit cell area.

### 4.5.1 The {100} surfaces

Figure 4.15 illustrates the plan view of the {100} surface of spinel terminated with the *a* and *b* planes. In this figure the ions in the surface plane are numbered

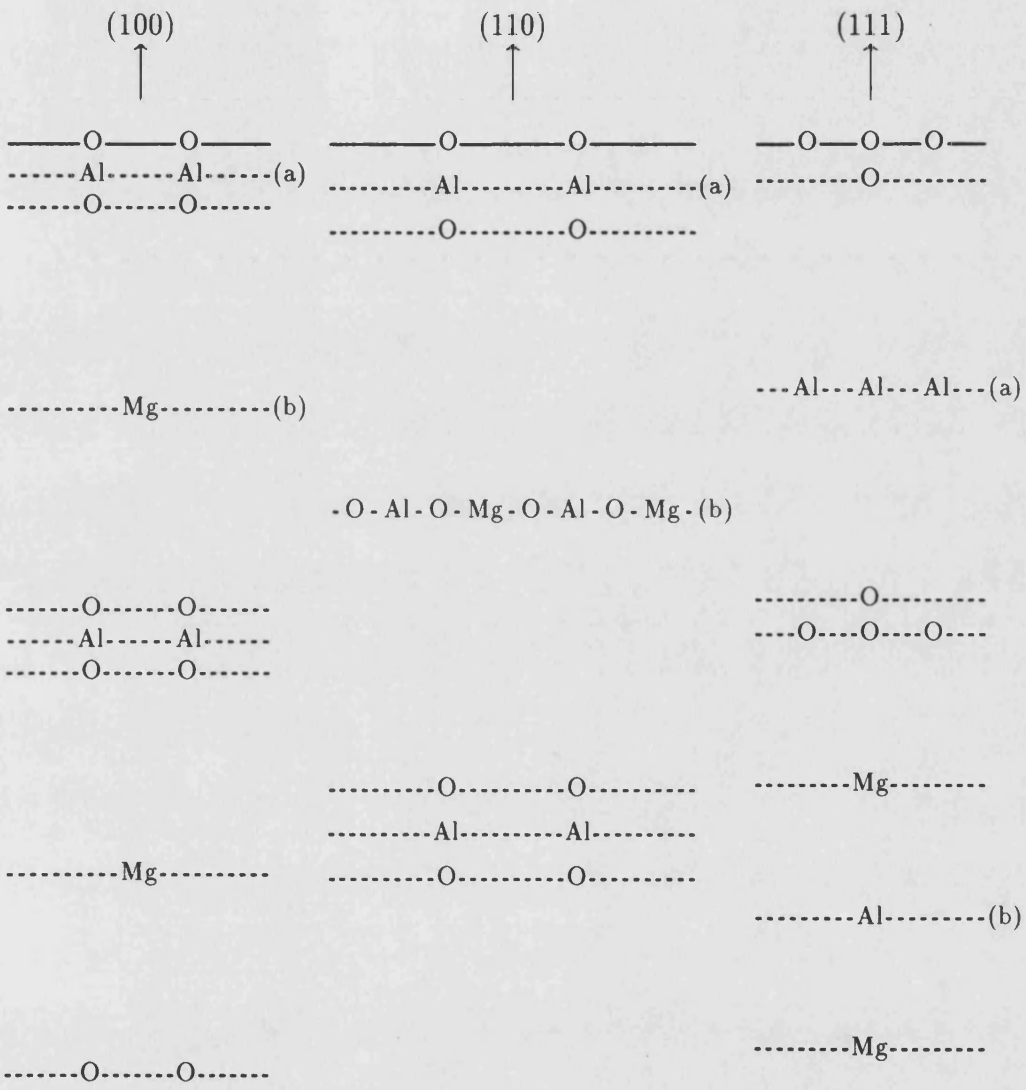


Figure 4.14: The stacking sequences for the low index surfaces of spinel $MgAl_2O_4$.

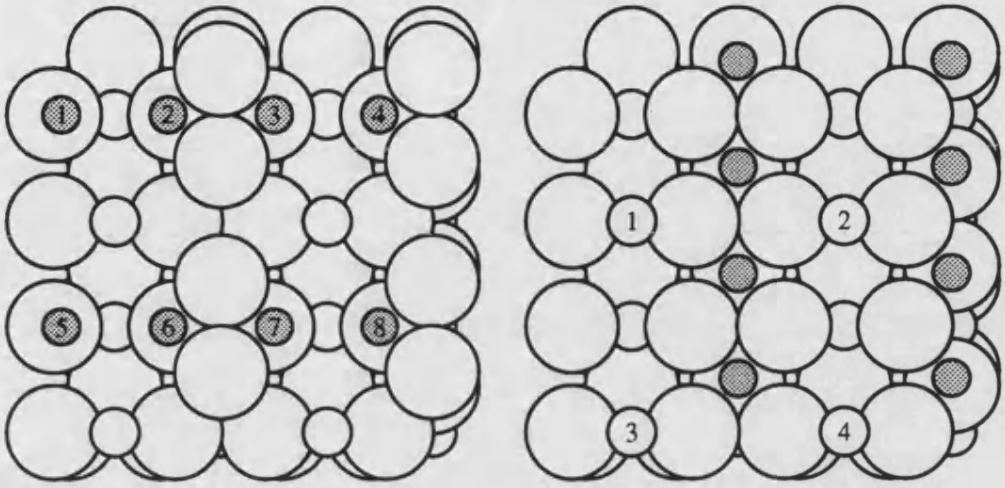


{100}a {100}b

Figure 4.15: Surface structure looking down upon the {100} surfaces of spinel. Surface unit cells scaled $2 \times 2$. $Al^{3+}$ cations shown shaded.

| Surface | Vacancy Sites | Unrelaxed Energy ($Jm^{-2}$) | Relaxed Energy ($Jm^{-2}$) |
|---|---|---|---|
| {100}a | 1,2,3,4 | 19.69 | 3.25 |
| | 1,2,7,8 | 13.65 | 3.48 |
| | 1,3,5,7 | 10.39 | 3.87 |
| | 1,3,6,8 | 10.31 | 3.95 |
| | 1,2,5,6 | 15.00 | 5.43 |
| | 1,4,5,8 | 15.00 | 6.99 |
| | 1,4,6,7 | 13.65 | 7.14 |
| {100}b | 1,2 | 4.11 | 2.33 |
| | 1,3 | 4.11 | 2.41 |
| | 1,4 | 3.81 | 2.28 |

Table 4.3: Calculated surface energies for the {100}a and {100}b surfaces of spinel $MgAl_2O_4$.

in order to make descriptions of the defect arrangements simpler. For the {100}a surface we see that the surface ions are arranged in rows with a larger separation in one direction. For a doubled surface unit cell there are 7 distinct arrangements of vacancies at the {100}a surface and 3 distinct arrangements at the {100}b.

The calculated surface energies for all these arrangements are given in table 4.3. From this table we can see a large variation in the surface energies depending on the vacancies used. Also we note that no simple relationship can be deduced from the unrelaxed surface energies, there are several pairs of energies which are identical before energy minimisation but differ significantly for the relaxed structure. Overall the {100}b surface is the more stable termination both before and after relaxation, even though all of the {100}a surfaces relax to a greater degree. This stability of the {100}b surface is understandable in term of lower charge of the surface cations and the coordination of these ions at the surface. For the {100}b termination the $Mg^{2+}$ ions at the surface are two coordinate as opposed to four in the bulk, on relaxation however these surface ions can relax into the surface between the rows of oxide ions increasing their coordination, figure 4.16. For the {100}a termination however, the surface $Al^{3+}$ cations have their coordination decreased by a larger amount (from six to three) and relaxation alone provides no simple way of increase their coordination. An additional feature of the {100}a termination is that there are a greater number of cations per unit area.

The above reasoning lead us to consider that inverting the cation arrangement at the surface could stabilise the surfaces terminated by trivalent cations. The inversion increasing the coordination of the trivalent cations. For each surface terminated in $Al^{3+}$ there is layer containing $Mg^{2+}$ cations in close proximity below the surface. We can therefore invert the cation arrangement by swapping any surface trivalent cation left after vacancies have been imposed with these divalent ions. The overall effect is to have a thin layer of *inverse* spinel on top of a *normal* spinel lattice. The surface energies for these "inverted" {100}a surfaces are

| Surface | Vacancy Sites | Unrelaxed Energy ($Jm^{-2}$) | Relaxed Energy ($Jm^{-2}$) |
|---|---|---|---|
| {100}ai | 1,2,3,4 | 17.21 | 3.48 |
| | 1,2,7,8 | 15.12 | 6.87 |
| | 1,3,5,7 | 14.52 | 3.76 |
| | 1,3,6,8 | 13.08 | 3.30 |
| | 1,2,5,6 | 13.04 | 3.27 |
| | 1,4,5,8 | 15.12 | 4.11 |
| | 1,4,6,7 | 14.52 | 4.66 |

Table 4.4: Calculated surface energies for the inverted {100}a surface of spinel $MgAl_2O_4$.

given in table 4.4. We can see that although the most stable of these surfaces is less stable than the best of the "normal" surfaces given in table 4.3 some of the arrangements are more stable than the corresponding identical "normal" arrangement. Although we have failed to find a more stable arrangement for the {100}a surface we shall see that in the case of the {110} and {111} surfaces these "inverted" arrangements become more important.

Taking all the surface energies given in tables 4.3 and 4.4 we can see that overall the {100}b surface with vacancies arranged diagonally at sites 1 and 4 is the most stable. The effects of relaxation on the structure of this surface are illustrated in figure 4.16. The surface as a whole contracts slightly, this is due to the relaxation of the surface cations into the surface. The surface anions rumple, with anions around the vacancies moving into the surface and anions surrounding the surface cations relaxing upwards. In addition to this vertical movement the anions surrounding the vacancy sites relax in the surface plane towards the remaining surface cations. These relaxation effect diminish rapidly as we move into the bulk, the effects being negligible four repeat units (8Å) below the surface.

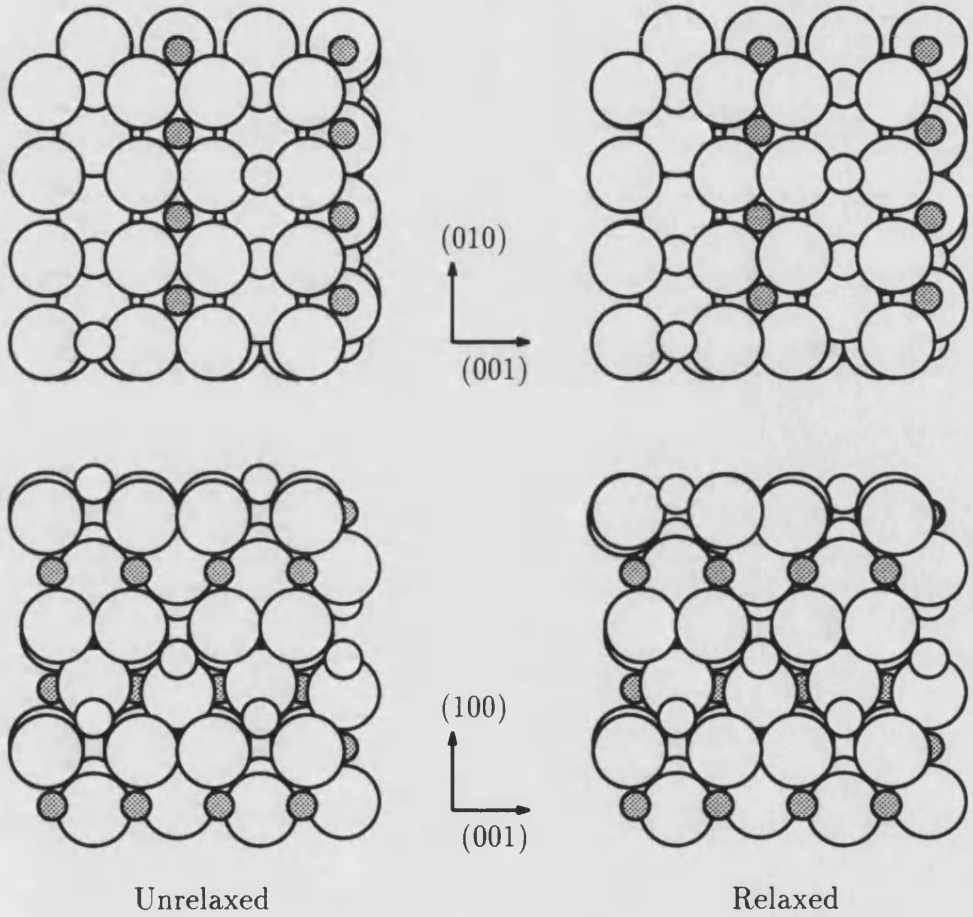


Figure 4.16: Relaxation of the (100)b surface. Views, top - looking down on the surface, bottom - perpendicular to the surface. $Al^{3+}$ cations shown shaded.

### 4.5.2 The {110} surfaces

The arrangement of ions at the two {110} surface terminations are shown in figure 4.17. As with the {100} terminations we have numbered the surface ions. In the case of the {110}b termination our calculations were restricted to a single surface unit cell as shown due to the large number of ions present. Using a double surface unit cell for the *a* terminations results in five distinct arrangements of defects, where as a single surface unit cell for the *b* termination results in six possible vacancy arrangements. The energies for these eleven possible surfaces are given in table 4.5. Both possible surface terminations give similar energies ranging from 5.3 $Jm^{-2}$ to 2.8 $Jm^{-2}$. The most stable arrangement being the {110}b termination with vacancies at sites 1, 3, 5 and 7/8. This is only 0.05 $Jm^{-2}$ more stable that the most stable {110}a arrangement.

As with the {100}a surface we also considered inverting the cation layers at the {110}a surface. The energies for these "inverted" surfaces are given in table 4.6. This time we see that for the {110}a surfaces the inversion has resulted in more stable surface energies. In fact some arrangements are up to 1 $Jm^{-2}$ more stable than the corresponding normal structure. The most stable surface overall is now the {110}ai surface with vacancies at sites 1, 2, 5 and 6 with a surface energy of 2.5 $Jm^{-2}$. The relaxed structure of this surface is given in figure 4.18. We can see from this diagram that the unrelaxed structure contains valleys whose sides are occupied by cations. The relaxation process results in a complex reconstruction of the surface anions as can been seen from the view looking down upon the surface, the effect of which is to destroy the valleys. This appears to generate an approximately flat surface. However, as can be seen from figure 4.19 looking down the $(\bar{1}10)$ axis, the relaxation process has generated a more shallow valley perpendicular to the original valleys along the line of the surface vacancies. Again these effects diminish rapidly as we move into the bulk, the structure three repeat units (8Å) below the surface being unchanged.

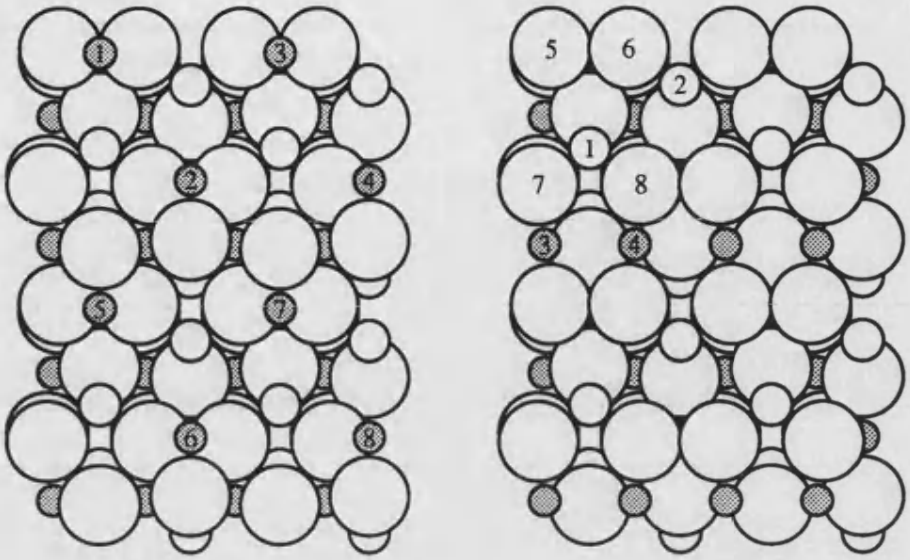


{110}a {110}b

Figure 4.17: Surface structure looking down upon the {110} surfaces of spinel. Surface unit cells scaled $2 \times 2$. $Al^{3+}$ cations shown shaded.

| Surface | Vacancy Sites | Unrelaxed Energy ($Jm^{-2}$) | Relaxed Energy ($Jm^{-2}$) |
|---|---|---|---|
| {110}a | 1,2,3,4 | 12.02 | 3.81 |
| | 1,2,5,6 | 10.23 | 2.90 |
| | 1,2,7,8 | 10.01 | 4.01 |
| | 1,3,5,7 | 9.34 | 3.69 |
| | 1,3,6,8 | 12.02 | 5.21 |
| {110}b | 1,3,5,6 | 15.54 | 3.75 |
| | 1,3,5,7 | 5.25 | 2.85 |
| | 1,3,5,8 | 8.41 | 2.85 |
| | 1,3,6,7 | 8.41 | 3.36 |
| | 1,3,6,8 | 12.36 | 5.31 |
| | 1,3,7,8 | 8.99 | 3.22 |

Table 4.5: Calculated surface energies for the {110}a and {110}b surfaces of spinel $MgAl_2O_4$.

| Surface | Vacancy Sites | Unrelaxed Energy ($Jm^{-2}$) | Relaxed Energy ($Jm^{-2}$) |
|---|---|---|---|
| {110}ai | 1,2,3,4 | 13.71 | 3.14 |
| | 1,2,5,6 | 10.82 | 2.50 |
| | 1,2,7,8 | 9.88 | 3.09 |
| | 1,3,5,7 | 9.25 | 3.17 |
| | 1,3,6,8 | 9.96 | 3.44 |

Table 4.6: Calculated surface energies for the inverted {110}a surface of spinel $MgAl_2O_4$.

### 4.5.3 The {111} surfaces

The surface structures of the {111} terminations are shown in figure 4.20. The surface energies for all the distinct arrangements of vacancies at these surfaces are given in table 4.7. Note the high symmetry of these surfaces; all of the vacancy arrangements at the {111}b surfaces are equivalent for a double surface unit cell. For the {111}a surface we have five possible arrangements of vacancies at the surface but it can be seen from the energies in table 4.7 that the relaxed structures all have similar energies. As a whole we can see that the {111}b surface is more stable. This extra stability is probably due to there fewer surface cations present at this surface.

Both surfaces terminate in trivalent cations, therefore "inverted" surfaces are possible in either case. The surfaces energies of these "inverted" surface structures are given in table 4.8. We can see that in all cases the "inverted" surfaces are more stable that the corresponding "normal" surfaces with the {111}bi surface being 0.86 $Jm^{-2}$ more stable than the {111}b surface. The structure of the unrelaxed and relaxed {111}bi surface with vacancies at locations 1 and 3 is given in in figure 4.21. We can see that the surface undergoes a minimum of reconstruction. The surface contracts slightly with the surface cations (now $Mg^{2+}$ following inversion) maintaining their position. This failure of the surface cations to burrow into the surface is due to the close packing of the anions below them. The anions surrounding the vacancies relax into the surface and towards the nearest cations.

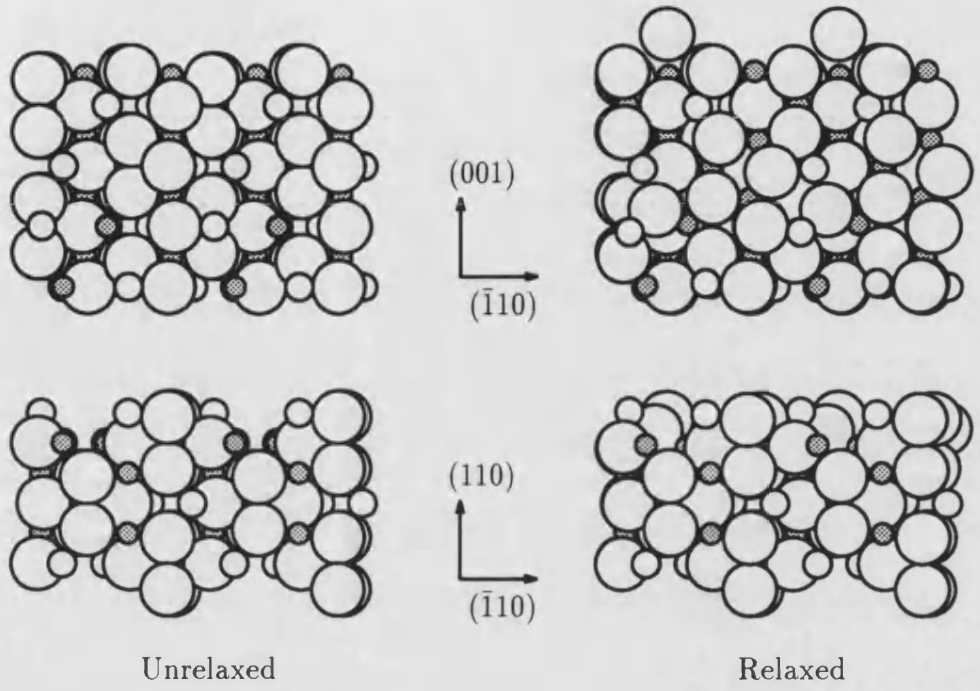


Figure 4.18: Relaxation of the (110)ai surface. Views, top - looking down on the surface, bottom - perpendicular to the surface. $Al^{3+}$ cations shown shaded.

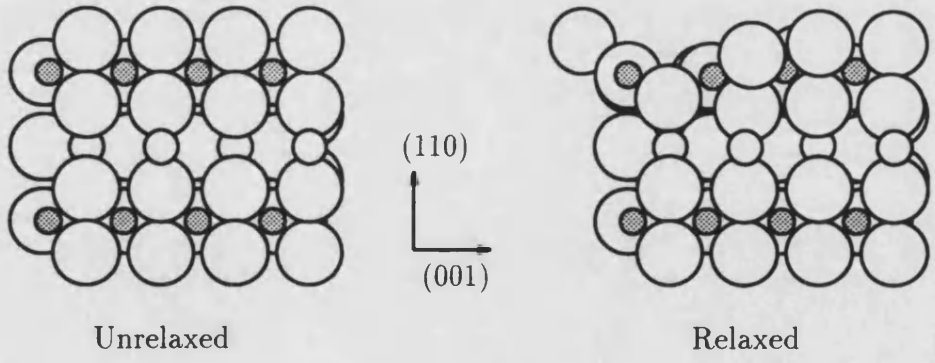


Figure 4.19: Relaxation of the (110)ai surface. View in the (1̄10) direction. $Al^{3+}$ cations shown shaded.

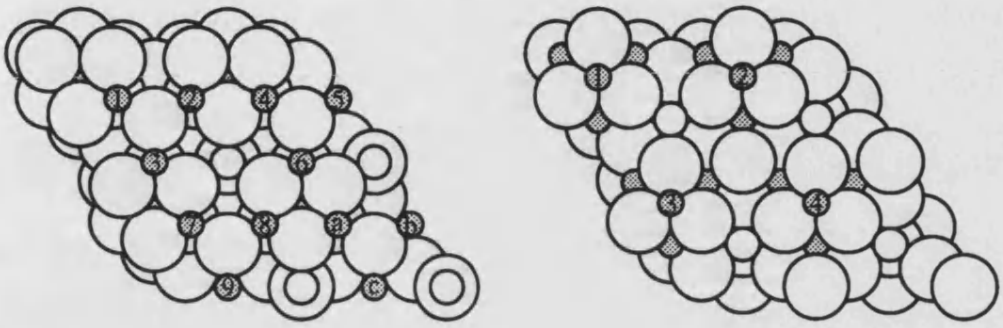

{111}a {111}b

Figure 4.20: Surface structure looking down upon the {111} surfaces of spinel. Surface unit cells scaled 2 × 2. $Al^{3+}$ cations shown shaded.

| Surface | Vacancy Sites | Unrelaxed Energy ($Jm^{-2}$) | Relaxed Energy ($Jm^{-2}$) |
|---|---|---|---|
| {111}a | 1,2,3,4,5,6 | 24.59 | 4.09 |
| | 1,2,4,5,7,a | 15.58 | 3.88 |
| | 1,2,4,7,8,a | 15.58 | 3.85 |
| | 1,2,4,7,a,b | 15.58 | 3.94 |
| | 1,2,6,7,8,c | 15.82 | 4.01 |
| {111}b | 1,2 | 7.75 | 3.46 |

Table 4.7: Calculated surface energies for the {111}a and {111}b surfaces of spinel $MgAl_2O_4$.

| Surface | Vacancy Sites | Unrelaxed Energy ($Jm^{-2}$) | Relaxed Energy ($Jm^{-2}$) |
|---|---|---|---|
| {111}ai | 1,2,3,4,5,6 | 17.42 | 3.09 |
| | 1,2,4,5,7,a | 11.41 | 3.46 |
| | 1,2,4,7,8,a | 12.44 | 3.34 |
| | 1,2,4,7,a,b | 12.38 | 3.38 |
| | 1,2,6,7,8,c | 11.66 | 3.21 |
| {111}bi | 1,2 | 7.08 | 2.60 |

Table 4.8: Calculated surface energies for the inverted {111}a and {111}b surfaces of spinel $MgAl_2O_4$.

The anions coordinated to the surface cations relax into the surface to a lesser degree allowing the cations to move into the surface slightly. Below the surface we see that the trivalent cation relax towards the bulk to larger extent than the divalent cations. This movement of the trivalent cations disrupts the planar nature of the lower oxide ions.

The lowest energies for each surface both before and after relaxation are summarised in table 4.9. Overall from these results we can see that we predict that the most stable configuration for each of the three surfaces contains only $Mg^{2+}$ cations in the terminating layer. This is achieved for the {110} and {111} surfaces by modifying the cation distribution in the near surface region by inversion. Unfortunately studies of the spinel surfaces have been limited, and hence no experiments have been performed to determined their structure or composition. A TEM study has been performed on stepped surfaces by Susnitzky et al [114] but this is of too low a resolution to be of much use here. A high resolution study has been performed by Hutchinson and Briscoe [115] on single crystals of the catalyst $ZnCrFeO_4$ which has a normal spinel structure. In this experiment differences in the terminating structure of each type of surface were noted. The {100} facet was seen to consist of ionic scale ledges, the {111} facet was atomically flat, and the {110} surfaces were seen as a hill and valley structure. These observations show

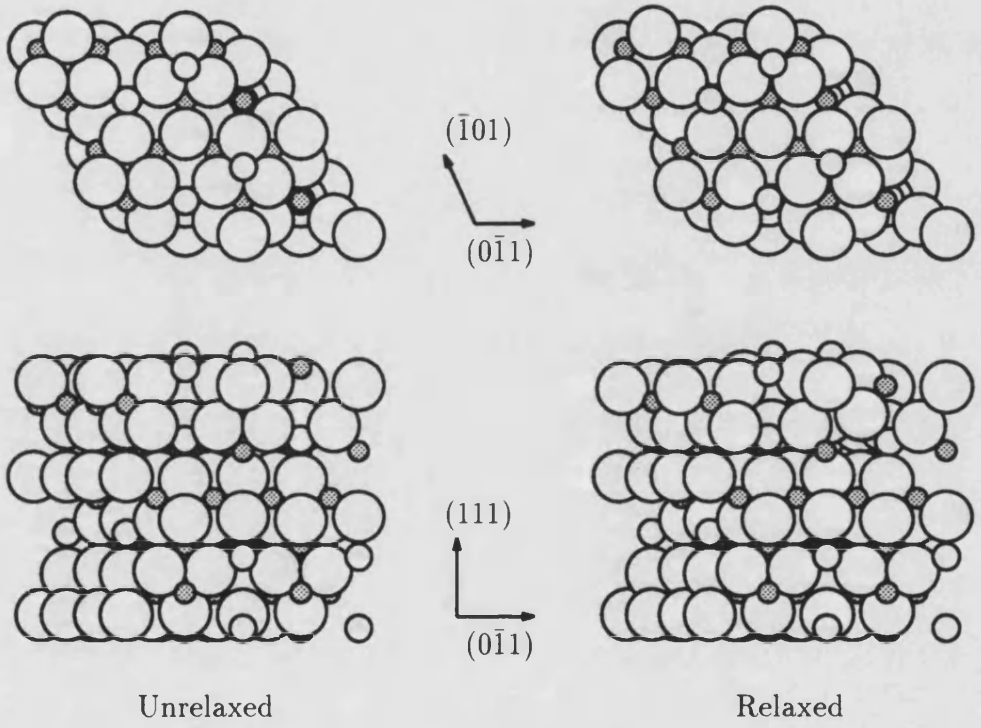


Figure 4.21: Relaxation of the (111)bi surface. Views, top - looking down on the surface, bottom - perpendicular to the surface. $Al^{3+}$ cations shown shaded.

| Surface | Unrelaxed Energy ($Jm^{-2}$) | Relaxed Energy ($Jm^{-2}$) |
|---|---|---|
| {100} | 3.81 ({100}b 1,2) | 2.28 ({100}b 1,2) |
| {110} | 5.25 ({110}b 1,3,5,7) | 2.50 ({110}ai 1,2,5,6) |
| {111} | 7.08 ({111}bi 1,2) | 2.60 ({111}bi 1,2) |

Table 4.9: Best of the calculated surface energies for the low index surfaces of $MgAl_2O_4$.

some agreement with the our calculated relaxed structured above. For the {100} surface we found the {100}b termination to be the most stable. This termination on relaxation is approximately flat, and could correspond to the ledges observed. For the {100}a termination the effects of relaxation are much larger, the surface is not flat and would not appear as a ledge. Our relaxed {110}ai surface as noted above also show a valley structure as observed by Hutchinson and Briscoe. These agreements suggest that we have predicted the correct termination for these two surfaces. In the case of the {111} surface however there is some disagreement. We found the {111}bi surface to be the most stable and the description of its relaxed structure given earlier shows that the surface cannot be described as flat. However we did find that the {111}a terminations formed a flat surface structure on relaxation and this is the termination suggested by Hutchinson and Briscoe to be the most likely for the {111} surface of $ZnFeCrO_4$. The extra stability of the {111}a surface may be due to the mixture of trivalent ions in this compound.

Perhaps due to the lack of experimental data on the surfaces of spinel structured compounds, theoretical calculations of their surface energies have been performed in the past. Mishra and Thomas [116] calculated the surface energies of several spinels including spinel itself. They found the {111} to be seven times more stable than the {100} surface which in turn was twice as stable as the {110} surface. Ebert and Kung [117] have also calculated surface energy for a general spinel limiting the calculation to the Coulombic terms only. They found the order of stability to be {100} followed by the {111} and then the {110} to be the least stable for a normal spinel. Both sets of calculations disagree with the results pre-

sented here, and in the case of the Mishra results there is no agreement what so ever. There are several reasons for this: (i) both of the previous calculations used an idealised spinel structure, they failed to take into account the distortion of the oxide lattice, (ii) both sets of calculations did not include relaxation phenomena and (iii) in the case of Mishra the choice of the terminating layer and calculation of the Coulombic contribution did not take into account dipolar considerations. For these reasons these previous calculations should be ignored.

In addition to the lack of experimental surface structural information, we are also limited in the morphological evidence to back up our calculations. The predicted equilibrium morphologies for spinel based on the surface energies given in table 4.9 are given in figure 4.22. We see that for the unrelaxed surfaces we predict a cubic crystal with some truncation of the edges by {110} faces. For the relaxed energies however, we see the presences of all three faces with the {100} faces still dominant but with large areas of {110} and {111} faces. The traditional form taken by most crystals of the spinel family is an octahedra, i.e. all {111} faces [109]. This would appear to contradict our prediction, however we must remember that we are considering equilibrium morphologies which only apply to small crystals. For spinel most crystals contain only the {111} faces but they do occasionally exhibit dodecahedral ({110}) and cubic ({100}) truncations [110, 108, 112]. This is inline with our predicted morphology if we assume that the {111} faces dominate due to kinetic effects.

## 4.6 The surfaces of Magnetite – $Fe_3O_4$

Magnetite as mentioned earlier adopts the *inverse* spinel structure. Its spinel nature becomes more obvious if we note that the iron present is in two oxidation states, $Fe^{II}Fe_2^{III}O_4$. In the inverse structure half of the trivalent cations occupy the tetrahedral sites while the remaining trivalent and divalent cations occupying the octahedral sites. Again as with spinel in the previous section we shall not use the full unit cell but a reduced unit cell. This cell contains four octahedral sites

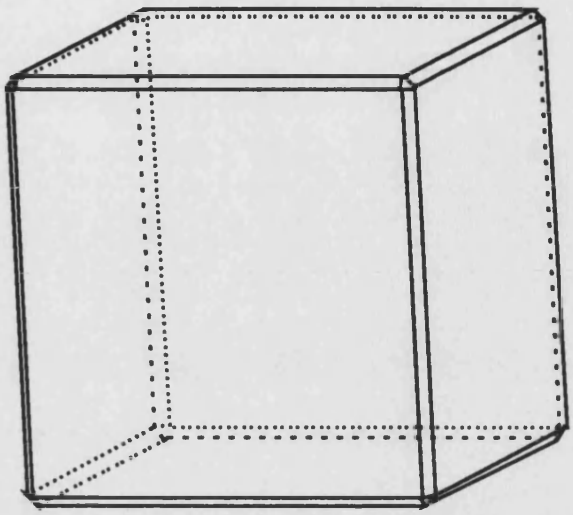

Unrelaxed

(001)

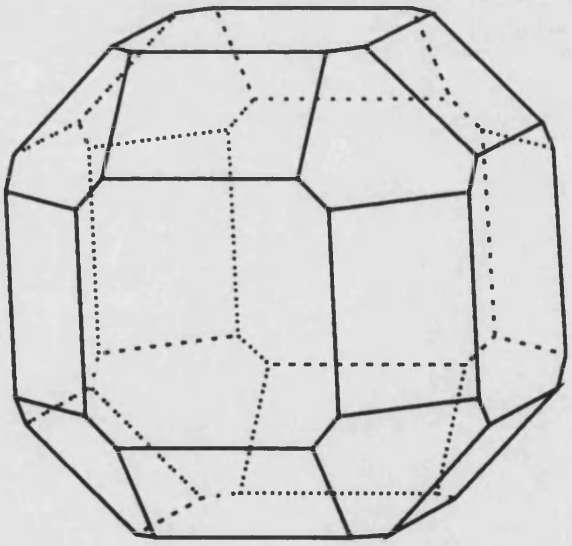

Relaxed

Figure 4.22: Predicted equilibrium morphologies for spinel $MgAl_2O_4$.

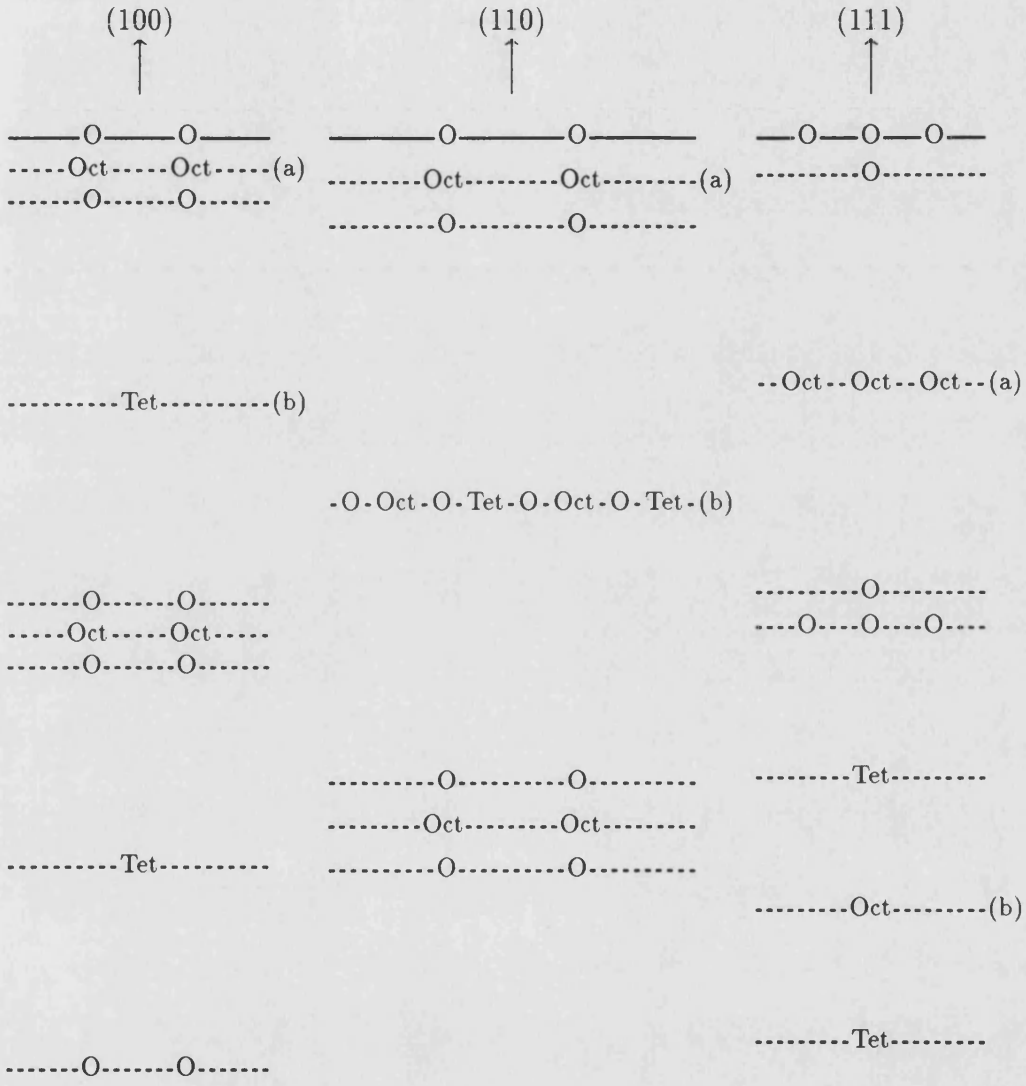


Figure 4.23: The stacking sequences for the low index surfaces of the spinel structure showing types of cation sites.

and therefore, there are six possible ways of arranging the mix of cations at these sites. In the bulk all these arrangement are equivalent, but when we introduce two dimensional periodicity the arrangement of the cations amongst these sites becomes more important. This is easily understood if we consider the type of cation sites in the spinel stacking sequences shown in figure 4.23.

If we consider the {100}a termination in figure 4.23 we can see that it contains two octahedral sites. Therefore depending on the distribution of cations, we can have three possible terminating layers: a $Fe^{2+}Fe^{2+}$ layer, a $Fe^{3+}Fe^{3+}$ layer or a $Fe^{2+}Fe^{3+}$ layer. These will have different surfaces energies and hence must be considered independently. Further complication would arise if we were to allow the lattice to change its octahedral cation distribution on a unit cell by unit cell basis as we move into the bulk. This would require a huge number of calculations and this possibility has therefore been ignored. Furthermore for mixed occupancy terminating layers, we are constrained by the symmetry of the original surface unit cell when scaling the surface.

### 4.6.1 The {100} surfaces.

We shall use the same numbering scheme for surface vacancies as we did in the previous section for spinel itself. As mentioned above we have three possible {100}a terminations. For the {100}b surface we have a single possible termination, however it should be noted that in order to maintain the {100}b layer as a mirror plane the occupancy of the {100}a layer below this surface must be $Fe^{2+}Fe^{3+}$. The calculated surface energies for these four possible {100} surfaces are given in table 4.10. We can see that again the {100}b termination is the most stable as was the case with spinel. However in the case of magnetite the surface is terminated in trivalent ions and the most stable arrangement has the vacancies along a row. For the {100}b surfaces we see that the mixed occupancy termination is the least stable with the divalent layer being the most stable of the three possibilities.

The relaxed structure of the most stable {100} surface is given in figure 4.24. Ions in the upper layer of the surface undergo considerable movement. The sur-

| Surface | Composition | Vacancy Sites | Unrelaxed Energy ($Jm^{-2}$) | Relaxed Energy ($Jm^{-2}$) |
|---|---|---|---|---|
| {100}a | $Fe^{2+}Fe^{2+}$ | 1,2,3,4 | 12.21 | 2.90 |
| | | 1,2,5,6 | 10.22 | 3.64 |
| | | 1,2,7,8 | 9.74 | 2.62 |
| | | 1,3,5,7 | 8.42 | 2.19 |
| | | 1,3,6,8 | 8.40 | 2.12 |
| | | 1,4,5,8 | 10.22 | 5.04 |
| | | 1,4,6,7 | 9.74 | 6.11 |
| {100}a | $Fe^{3+}Fe^{3+}$ | 1,2,5,6 | 11.25 | 2.33 |
| | | 1,2,7,8 | 9.97 | 2.31 |
| | | 1,3,5,7 | 7.21 | 2.33 |
| | | 1,3,6,8 | 7.13 | 2.29 |
| | | 1,4,5,8 | 11.25 | 3.29 |
| | | 1,4,6,7 | 9.97 | 3.09 |
| {100}a | $Fe^{2+}Fe^{3+}$ | 1,2,3,4 | 15.58 | 3.40 |
| | | 1,2,5,6 | 12.86 | 2.80 |
| | | 1,2,7,8 | 12.01 | 4.88 |
| | | 1,3,5,7 | 10.97 | 2.84 |
| | | 1,3,6,8 | 14.46 | 7.50 |
| | | 1,4,5,8 | 12.86 | 2.59 |
| | | 1,4,6,7 | 12.01 | 2.48 |
| {100}b | $Fe^{3+}$ | 1,2 | 5.50 | 1.68 |
| | | 1,3 | 5.50 | 1.78 |
| | | 1,4 | 4.91 | 2.03 |

Table 4.10: Calculated surface energies for the {100} surfaces of magnetite $Fe_3O_4$.

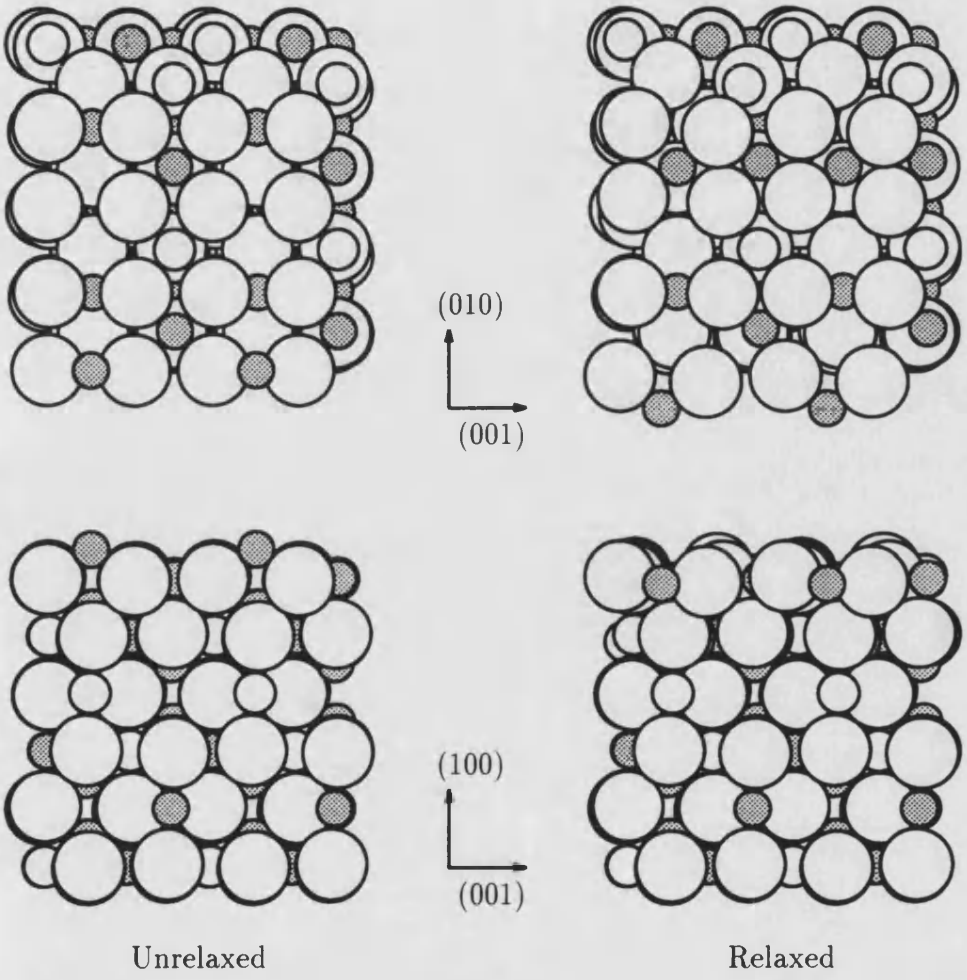


Figure 4.24: Relaxation of the (100)b surface. Views, top - looking down on the surface, bottom - perpendicular to the surface. $Fe^{3+}$ cations shown shaded.

face cations burrow deep into the surface whilst also moving diagonally. This is accompanied by movement of the anions with the surface cations. In addition, the cations below the surface near the vacancy sites move towards these sites distorting the anion structure above. There is much more relaxation than in the case of the $MgAl_2O_4$ {100}b surface where the relaxation process was limited to surface cations moving into the surface. The extra relaxation in the case of $Fe_3O_4$ may be due to the higher charge of the surface cations and the less symmetric nature of the under lying lattice, the next layer of cations being mixed. The extra relaxation at the surface also extends further into the bulk, the effects becoming minimal six repeat units (10 Å) below the surface.

### 4.6.2 The {110} surfaces.

The energies for the six possible {110} surfaces are given in table 4.11. We can see that as with the {100}a surface we have three possible surface terminating layers for the {110}a direction. There are also three possible terminating layers for the {110}b surface. In the case of the mixed cation {110}b layer we find that the layer is split into three, with half the anions and tetrahedrally coordinated cations moving above the layer of octahedral sites and the other half moving below. The structure is therefore symmetric about a $Fe^{2+}Fe^{3+}$ layer of octahedral (in the bulk) sites which now becomes the surface layer. The vacancy arrangements at this surface will follow the pattern of the {110}a surface and will therefore be numbered accordingly.

We can see from table 4.11 that, in general, the {110}a surfaces are more stable than the {110}b surfaces. The most stable surface is the {110}a terminated by a layer of divalent cations. This surface is at least 0.2 $Jm^{-2}$ more stable than any other {110} surface considered. The structure of this surface after relaxation is illustrated in figure 4.25. Upon relaxation we can see that this surface forms a highly symmetric structure, which matches the symmetry of the vacancy arrangement. The result is that the oxide anions coordinated to the remaining surface cations rotate about these cations whilst moving into the valleys present in the

| Surface | Composition | Vacancy Sites | Unrelaxed Energy ($Jm^{-2}$) | Relaxed Energy ($Jm^{-2}$) |
|---|---|---|---|---|
| {110}a | $Fe^{2+}Fe^{2+}$ | 1,2,3,4 | 7.35 | 2.09 |
| | | 1,2,5,6 | 8.02 | 2.47 |
| | | 1,2,7,8 | 7.27 | 1.84 |
| | | 1,3,5,7 | 7.00 | 1.82 |
| | | 1,3,6,8 | 7.35 | 2.09 |
| {110}a | $Fe^{3+}Fe^{3+}$ | 1,2,3,4 | 13.63 | 2.22 |
| | | 1,2,5,6 | 11.95 | 2.39 |
| | | 1,2,7,8 | 11.77 | 2.11 |
| | | 1,3,5,7 | 11.22 | 2.80 |
| | | 1,3,6,8 | 13.63 | 2.11 |
| {110}a | $Fe^{2+}Fe^{3+}$ | 1,2,3,4 | 10.68 | 2.55 |
| | | 1,2,5,6 | 9.56 | 2.16 |
| | | 1,2,7,8 | 9.39 | 2.13 |
| | | 1,3,5,7 | 10.25 | 2.03 |
| | | 1,3,6,8 | 10.68 | 2.13 |
| {110}b | $Fe_4^{3+}O_4^{2-}$ | 1,3,5,6 | 17.53 | 4.62 |
| | | 1,3,5,7 | 6.52 | 2.17 |
| | | 1,3,5,8 | 9.22 | 2.97 |
| | | 1,3,6,7 | 9.22 | 2.85 |
| | | 1,3,6,8 | 12.65 | 2.75 |
| | | 1,3,7,8 | 6.81 | 2.30 |
| {110}b | $Fe_2^{2+}Fe_2^{3+}O_4^{2-}$ | 1,3,5,6 | 15.79 | 6.56 |
| | | 1,3,5,7 | 6.29 | 2.50 |
| | | 1,3,5,8 | 7.61 | 3.00 |
| | | 1,3,6,7 | 7.61 | 2.21 |
| | | 1,3,6,8 | 9.56 | 2.07 |
| | | 1,3,7,8 | 6.13 | 2.39 |
| {110}b | $Fe^{2+}Fe^{3+}$ | 1,2,3,4 | 11.36 | 2.68 |
| | | 1,2,5,6 | 7.52 | 2.38 |
| | | 1,2,7,8 | 7.38 | 2.29 |
| | | 1,3,5,7 | 5.49 | 2.36 |
| | | 1,3,6,8 | 5.91 | 2.39 |

Table 4.11: Calculated surface energies for the {110} surfaces of magnetite $Fe_3O_4$.

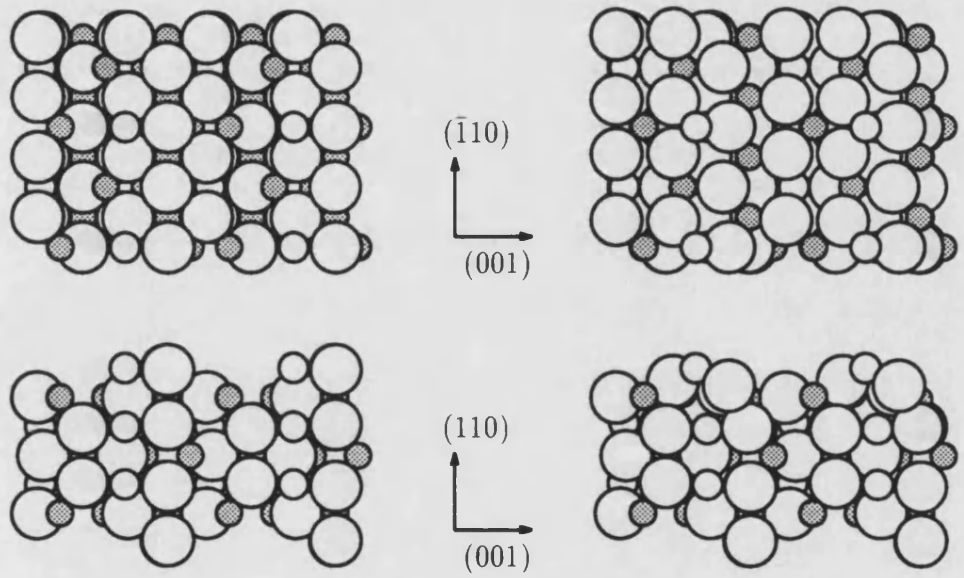


Figure 4.25: Relaxation of the (110)a surface. Views, top - looking down on the surface, bottom - perpendicular to the surface. $Fe^{3+}$ cations shown shaded.

{110}a structure. However the magnitude of the relaxation are such that only the top few layers of ions are involved, below the second repeat (4 Å) the structure remains unchanged.

### 4.6.3 The {111} surfaces.

The {111} surfaces of spinel both terminate in layers containing only octahedral sites. The {111}a termination contains three octahedral sites which allows us two possible compositions, $Fe^{2+}Fe_2^{3+}$ and $Fe_2^{2+}Fe^{3+}$, whereas the {111}b terminates is a single octahedral site which may contain either type of cation. The calculated surface energies for these surfaces are given in table 4.12. Note that in the case of the {111}b not all vacancy arrangements are equivalent, as they are in spinel, due to the mixed cation occupancy of the {111}a layer below the surface.

From these energies we can see that, as with $MgAl_2O_4$ the {111}b surface terminated by divalent cations is the most stable. It is approximately 1 $Jm^{-2}$ more stable than the equivalent surface terminated in trivalent ions. In addition, the {111}a surface containing a majority of divalent cations is slightly more stable than than the same surface containing a majority of trivalent cations. The relaxed structure of the most stable {111}b surface is shown in figure 4.26. As expected, the surface cations relax into the surface. This is accompanied by a movement of the surface anion coordinated to these cations away from the bulk. The anions surrounding the vacant surface cation sites relax into the surface and spread outwards. This results in a two level surface, the upper layer along the line of remaining surface cations. Overall the relaxation effects continue until two repeat units (5Å) below the surface.

Collecting all these results together we obtain the most stable energy for each of the surfaces. These are given in table 4.13 both for the unrelaxed and relaxed surfaces. Comparing these results to the earlier spinel calculations, we see that for both substances the most stable termination for each surface is identical. The

| Surface | Composition | Vacancy Sites | Unrelaxed Energy ($Jm^{-2}$) | Relaxed Energy ($Jm^{-2}$) |
|---|---|---|---|---|
| {111}a | $Fe^{2+}Fe_2^{3+}$ | 1,2,3,4,5,6 | 16.37 | 2.78 |
| | | 1,2,4,5,7,a | 9.29 | 2.63 |
| | | 1,2,4,7,8,a | 10.61 | 2.58 |
| | | 1,2,4,7,a,b | 9.86 | 2.81 |
| | | 1,2,6,7,8,c | 11.27 | 4.63 |
| {111}a | $Fe_2^{2+}Fe^{3+}$ | 1,2,3,4,5,6 | 12.99 | 2.67 |
| | | 1,2,4,5,7,a | 9.31 | 2.46 |
| | | 1,2,4,7,8,a | 9.26 | 2.46 |
| | | 1,2,4,7,a,b | 9.26 | 2.86 |
| | | 1,2,6,7,8,c | 8.56 | 2.36 |
| {111}b | $Fe^{2+}$ | 1,2 | 4.92 | 2.22 |
| | | 1,4 | 4.91 | 2.24 |
| {111}b | $Fe^{3+}$ | 1,2 | 8.45 | 3.38 |
| | | 1,4 | 8.40 | 3.18 |

Table 4.12: Calculated surface energies for the {111} surfaces of magnetite $Fe_3O_4$.

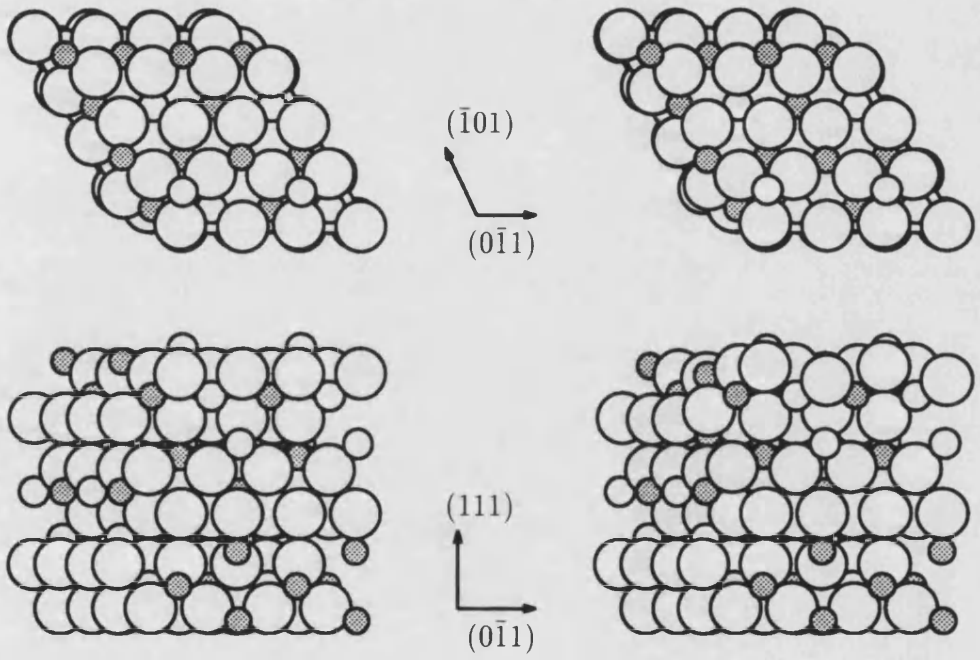


Figure 4.26: Relaxation of the (111)b surface. Views, top - looking down on the surface, bottom - perpendicular to the surface. $Fe^{3+}$ cations shown shaded.

| Surface | Unrelaxed Energy ($Jm^{-2}$) | Relaxed Energy ($Jm^{-2}$) |
|---|---|---|
| {100} | 4.91 ({100}b $Fe^{3+}$ 1,4) | 1.68 ({100}b $Fe^{3+}$ 1,2) |
| {110} | 5.49 ({110}b $Fe^{2+}Fe^{3+}$ 1,3,5,7) | 1.82 ({110}a $Fe_2^{2+}$ 1,3,5,7) |
| {111} | 4.91 ({111}b $Fe^{2+}$ 1,4) | 2.22 ({111}b $Fe^{2+}$ 1,2) |

Table 4.13: Best of the calculated surface energies for the low index surfaces of $Fe_3O_4$.

only difference occurs with the {100} surface where in the case of spinel, $MgAl_2O_4$, the {100}a surface terminates in divalent cations whereas for magnetite it terminates with trivalent cations. Although we predict the same terminations for both compounds, the arrangement of the vacancies at these surfaces are different.

As with spinel there is a lack of experimental data on the surface structure of magnetite. Mössbauer studies on thin {111} layers grown on alumina have shown that the disruption to the lattice structure is restricted to the top 5Å of the layer [118]. Also some parts of the $Fe^{2+}$ spectra remain unexplained. Although structural studies of the surface of magnetite have not been performed there has been some interest in the size dependence of the magnetic properties of magnetite. This has lead to several attempts to grow small crystals [119]. These crystals should be comparable to the predicted equilibrium morphology. The predicted equilibrium morphologies based on the surface energies of table 4.13 are given in figure 4.27. For the unrelaxed surfaces we find a large amount of {111} faces which using the relaxed surface energies almost disappear completely. The relaxed morphology is basically cubic with large {110} faces. As is normal for spinels, large magnetite crystals adopt an octahedral habit [109, 110] but in the case of magnetite purely dodecahedral crystals are quite common [108, 112]. Cubic habit does occur for large crystals but this is uncommon [112]. In contrast for small crystals pure cubic habit has been seen [120] but in most cases mixed habits are formed. Viswanathiah et al [121] have grown crystals of sizes between 0.1 and 0.2 mm, these show an octahedral habit but with {110} faces present. Smaller crystals prepared by Heider and Bryndzia [119] show a rounded form with crystals

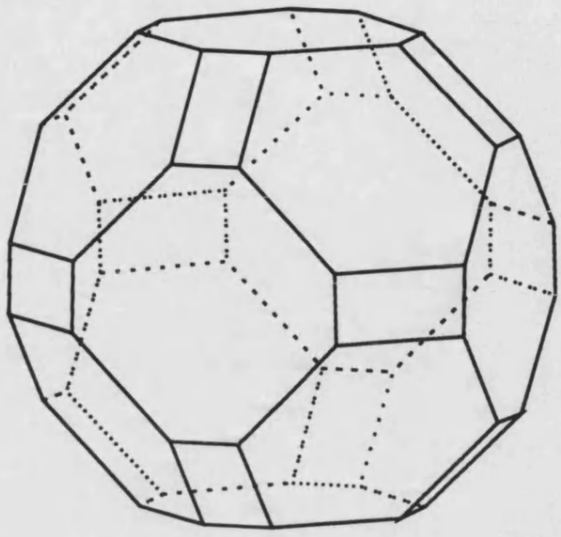

Unrelaxed

(001)

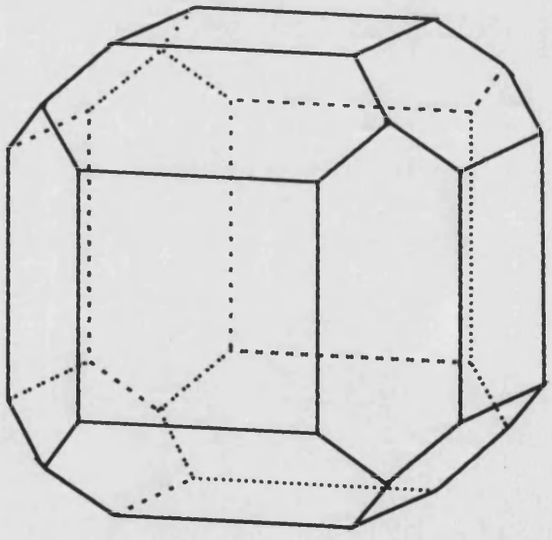

Relaxed

Figure 4.27: Predicted equilibrium morphologies for magnetite $Fe_3O_4$.

of approximately 12 $\mu$m showing a mixture of all three types of faces. From these experiments we can speculate that the {111} faces becomes dominant as the crystal size increases. This effect is also seen in the work of Hirano and Somiya [122]. They found that the size and habit of crystals grown in the same capsule varied with location in the capsule which in turn related to the temperature at which the growth occurred. Crystals of approximately 50 $\mu$m had a rounded habit whereas crystals grown at the top of the capsule, which were in the size range of around 100 $\mu$m, show octahedral habit. Fine particles of magnetite with an average diameter of 240Å have also been prepared [123]. These have a good crystal habit although detailed determination of this habit was not performed. However examination of a TEM image include in this paper suggests a mixture of faces. Overall all these experiments suggest that the {111} dominates due to kinetic effects and thus our result of a habit containing very small quantities of {111} can be justified.

## 4.7 The surfaces of Forsterite – $Mg_2SiO_4$

Forsterite is a member of the olivine group of minerals. This group varies in composition from forsterite $Mg_2SiO_4$ to fayalite $Fe_2SiO_4$ there being a complete diadochy between $Mg^{2+}$ and $Fe^{2+}$ in the structure. The whole group shows orthorhombic symmetry and consists of independent $SiO_4$ tetrahedra linked by divalent cations in octahedral coordination [109]. The divalent cations occupy two crystallographically distinct sites, M(1) and M(2), figure 4.28A. The oxygen lattice deviates significantly from hexagonal close packing, there is therefore a large variation in the metal-oxide bond distances, the M(1) octahedra having the smaller average metal-oxides bond distance [124].

The deviation of the lattice from ideal packing results in a series of complex stacking sequences perpendicular to the low index surfaces, figures 4.29 (non-dipolar repeats) and 4.30 (dipolar repeats). In many of these sequences we can see the presence of ion layers in close proximity to each other, these may appear

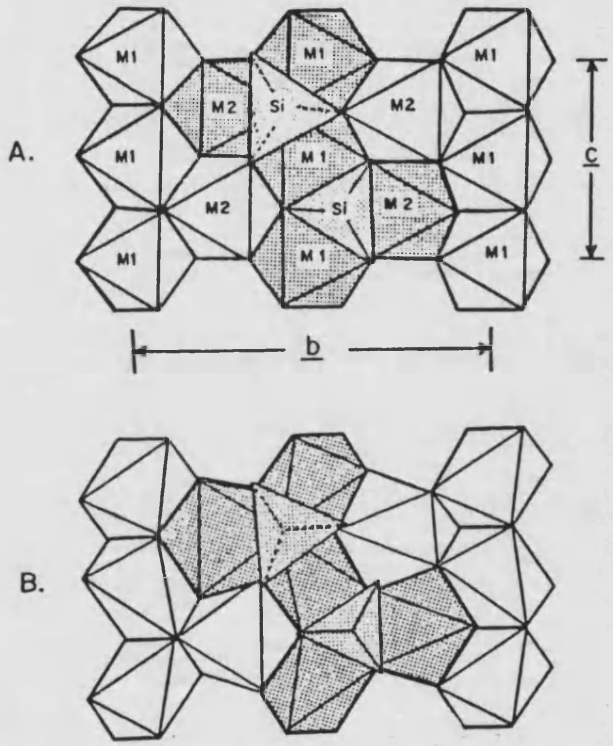


Figure 4.28: Olivine crystal structure, (A) ideal HCP model, (B) actual structure [124].

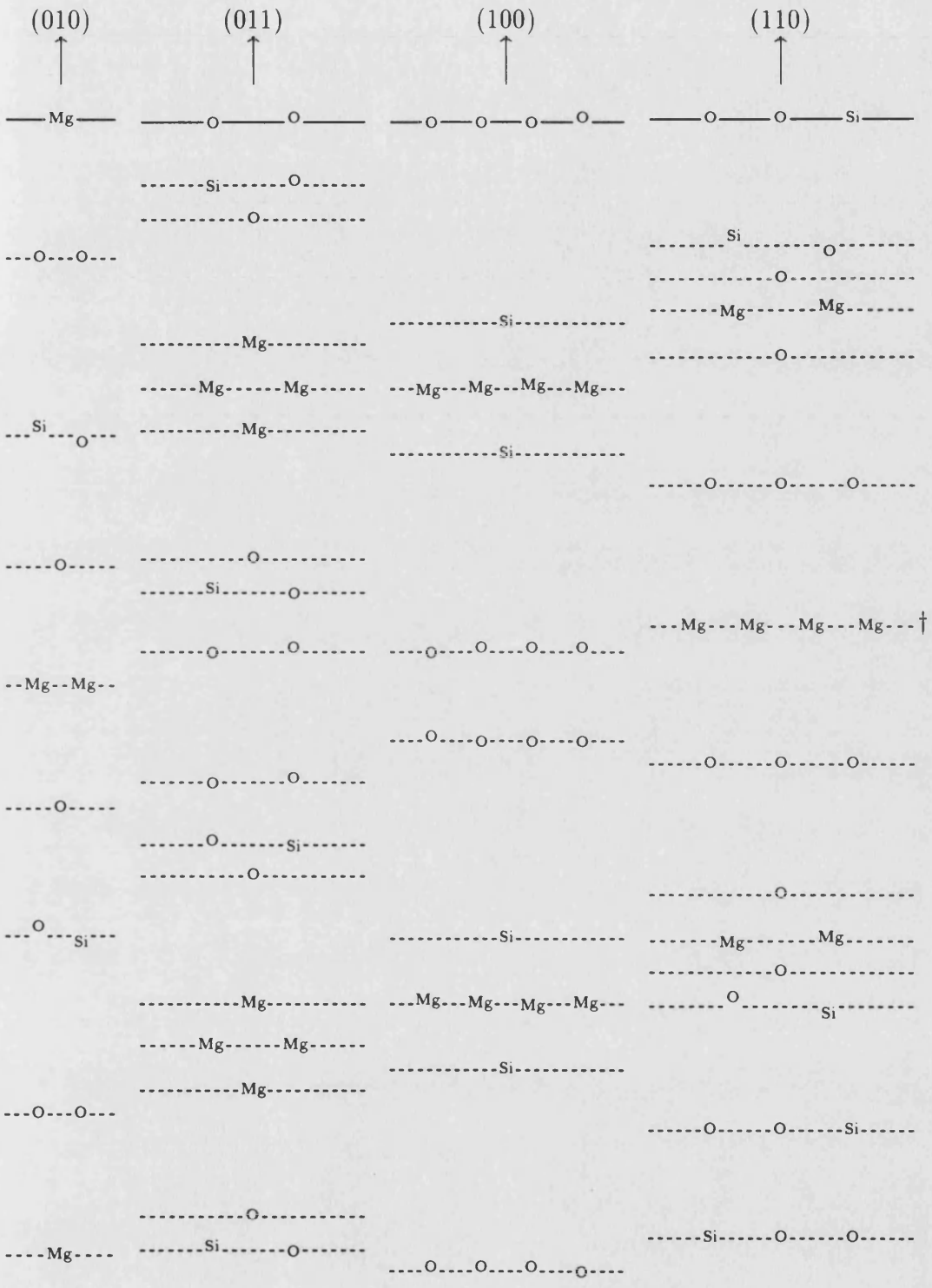


Figure 4.29: The stacking sequences for the low index non-dipolar surfaces of forsterite $Mg_2SiO_4$.

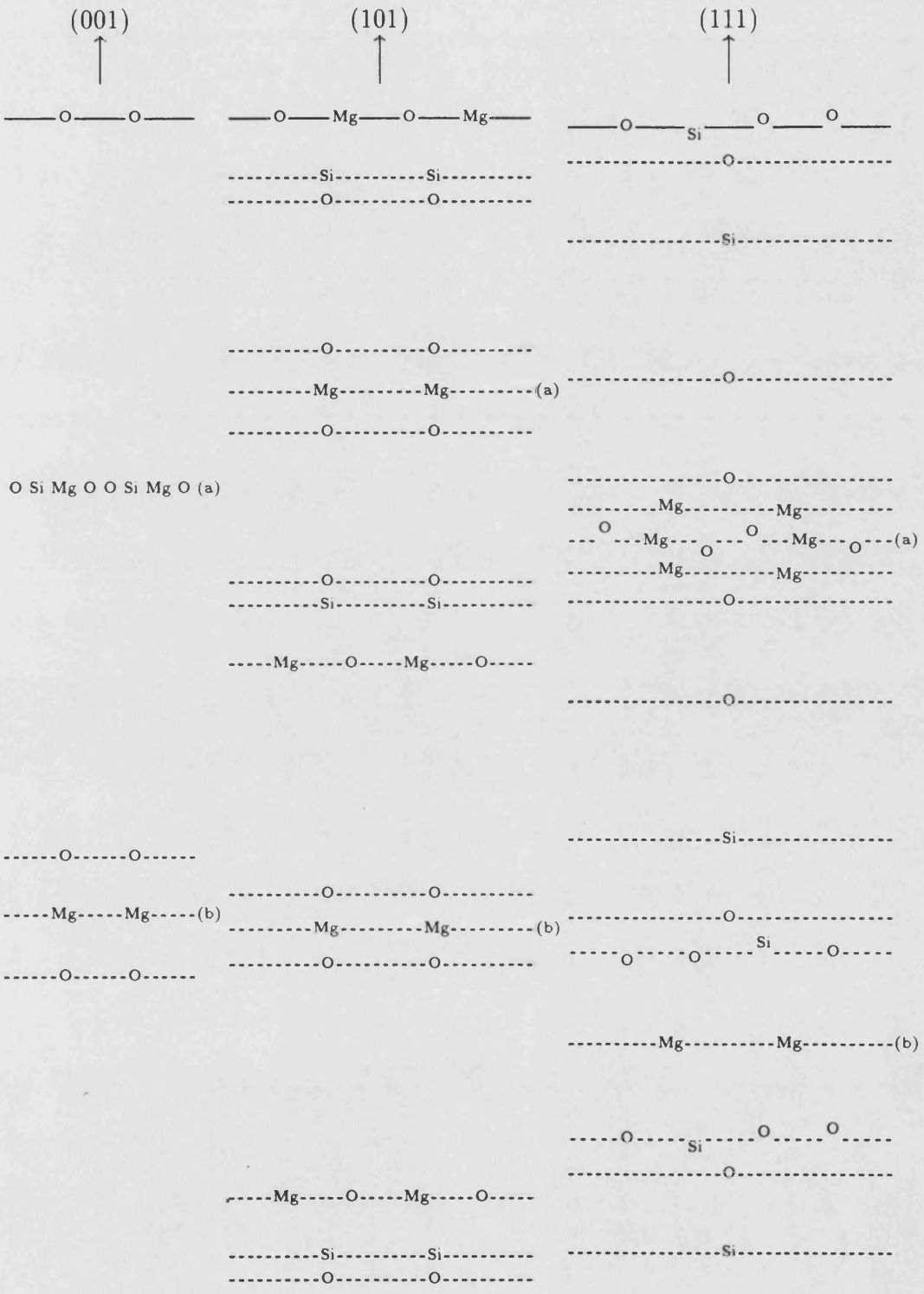


Figure 4.30: The stacking sequences for the low index dipolar surfaces of forsterite $Mg_2SiO_4$.

at first glance to be coplanar. For instance the {100} surface is terminated by a single oxide ion which lies 0.02Å above another single oxide ion layer, this in turn is 0.002Å above a layer containing two oxide ions!. All four appear together in figure 4.29 with the surface anion raised slightly. The {111}b surface is also complicated with a large number of ions in the vicinity of this termination. The actual terminating layer in the case of the {111}b surface consists of two $Mg^{2+}$ ions. The terminations in the remaining surface are more distinct.

The modelling of forsterite is further complicated by the presence of highly covalent $SiO_4$ tetrahedra. As mentioned in chapter 2, such structures are best modelled using a three body bond bending potential. However the MIDAS code as supplied by Harwell does not support three body potentials and therefore initial calculations were carried out using a two body potential. At a latter date I extended MIDAS to include bond bending three body potentials and the calculations were repeated. Here we shall include both sets of results so that we may see the effect of the three body potential on the calculated surface energies and the relaxed structures. The calculated surface energies of the seven low index surfaces of forsterite using both potentials are presented in tables 4.14 and 4.15. In the case of the dipolar surfaces we have included the energies of the most stable vacancy arrangement only. In addition, due to the presence of $Si^{4+}$ at the non-dipolar {110} termination we have also considered the dipolar {110}† termination, figure 4.29.

In both sets of results we observe that for all but the {010} surface the non-dipolar terminations are less stable than the dipolar terminations. In the special case of the {110} we see that the non-dipolar termination is over 1 $Jm^{-2}$ less stable than the dipolar {110}† termination. Both tables show the {010} surface to be the most stable. This agrees with the experimental fact that the {010} surface has been found to be the major cleavage plane for the olivines [108, 109]. Comparing the results in tables 4.14 and 4.15 on a surface by surface basis we see that in most cases there is good agreement. This is reflected in the order of stability of

| Surface | Unrelaxed Energy ($Jm^{-2}$) | Relaxed Energy ($Jm^{-2}$) |
|---|---|---|
| {010} | 2.28 | 1.26 |
| {011} | 11.59 | 2.23 |
| {100} | 7.78 | 2.56 |
| {110} | 17.03 | 2.81 |
| {110}† | 3.56 | 1.59 |
| {001}a | 5.08 | 2.16 |
| {001}b | 3.81 | 1.55 |
| {101}a | 5.92 | 2.46 |
| {101}b | 7.44 | 2.21 |
| {111}a | 11.13 | 1.70 |
| {111}b | 7.01 | 1.97 |

Table 4.14: Calculated surface energies of the low index surfaces of forsterite using two body potentials.

| Surface | Unrelaxed Energy ($Jm^{-2}$) | Relaxed Energy ($Jm^{-2}$) |
|---|---|---|
| {010} | 2.20 | 1.23 |
| {011} | 11.70 | 2.68 |
| {100} | 7.22 | 2.52 |
| {110} | 17.00 | 2.65 |
| {110}† | 3.47 | 1.66 |
| {001}a | 5.10 | 2.62 |
| {001}b | 3.80 | 1.69 |
| {101}a | 5.95 | 2.46 |
| {101}b | 7.15 | 5.39 |
| {111}a | 11.16 | 2.43 |
| {111}b | 6.86 | 1.86 |

Table 4.15: Calculated surface energies of the low index surfaces of forsterite using three body potentials.

the surfaces both before and after relaxation. Taking the most stable termination where a choice is possible, both potentials give the same order of stability before relaxation, i.e.

$$\{010\} < \{110\} < \{001\} < \{101\} < \{111\} < \{100\} < \{011\}$$

This is in agreement with the order predicted using the analytical periodic bond chain technique [125] to estimate the relative surface stabilities. After relaxation there is slight disagreement between the two potential models at the less stable end of the order. The order of stability for the two body potential after relaxation being

$$\{010\} < \{001\} \approx \{110\} < \{111\} < \{101\} < \{011\} < \{100\}$$

whereas the three body potential predicts the {100} surface to be slightly more stable than the {011} surface.

Despite this general agreement between the potentials there are some notable disagreements. The most extreme case occurs with the {101}b surface where the difference in the surface energies is over 3 $Jm^{-2}$. This may be attributed to the fact that when we cleave this surface at the {101}b termination we split a $SiO_4$ tetrahedron, and thus the $Si^{4+}$ nearest the surface is only bonded to two oxide ions. The bond bending potential restricts the movement of this $Si^{4+}$ and therefore the relaxation of the surface is less than for the two body potential where bond angle restrictions do not apply. On closer examination of the other surfaces similar $SiO_4$ tetrahedra splitting is seen in the majority of cases. The surfaces where this does not occur are the {010}, {110}† and both the {001} terminations. Not unexpectedly these surfaces are predicted to be the three most stable both before and after relaxation. From these results we can see that disruption of the $SiO_4$ tetrahedra reduces the stability of the surface and therefore if we were to maintain these tetrahedra we would expect enhanced surface stability.

This may be achieved in the majority of cases by transferring the oxide anions whose bonds are normally broken by surface formation between the two surfaces.

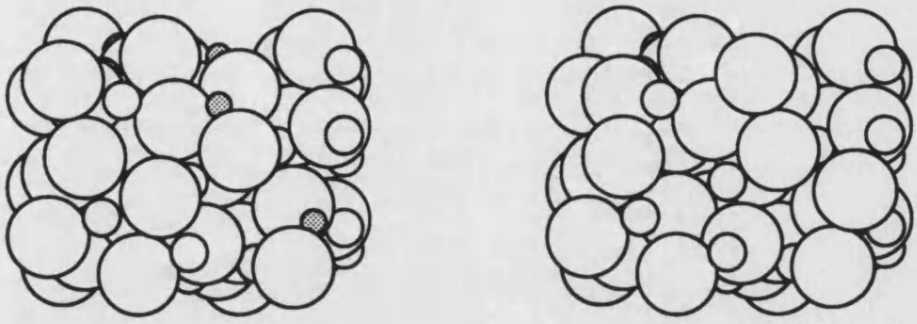

(a) (b)

Figure 4.31: Surface structure for the {101}b surface of forsterite. $Si^{4+}$ cations shown shaded. (a) Strict cleavage termination. (b) Transfer of oxide ions to maintain tetrahedral coordination of silicon cation.

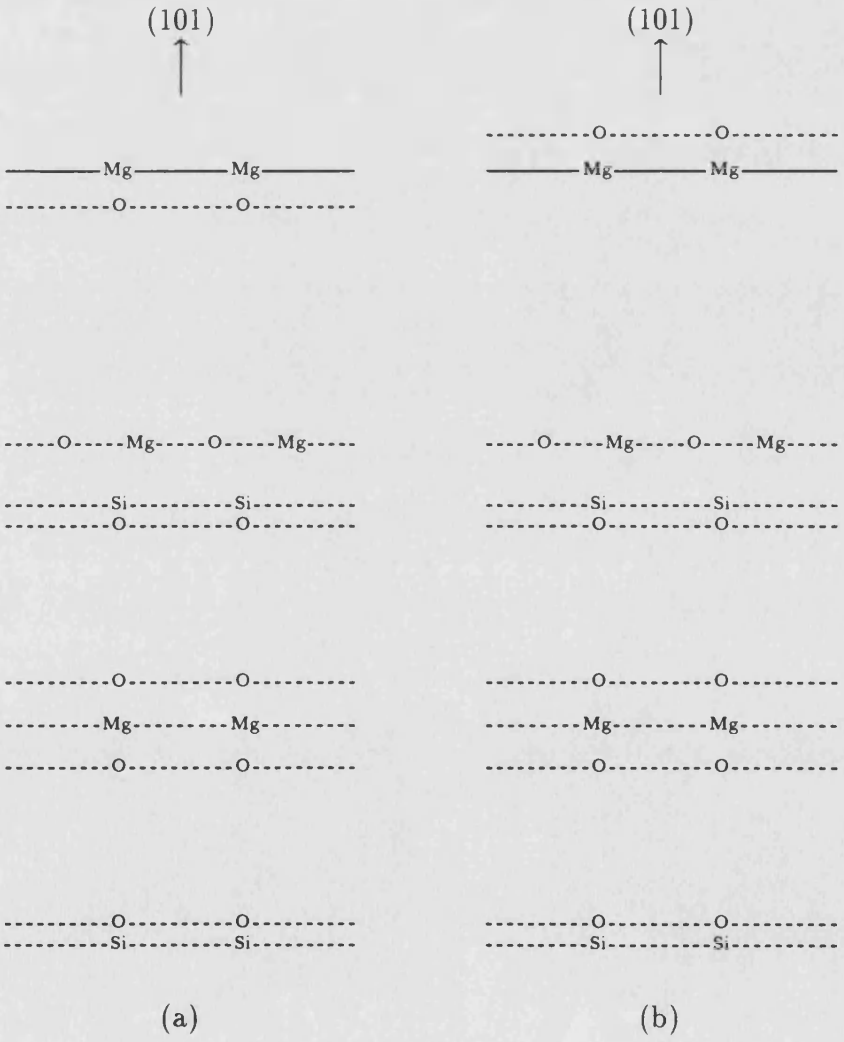


(a) (b)

Figure 4.32: Change in stacking sequence for th {101}b surface to maintain $SiO_4$ tetrahedra. (a) Original stacking sequence, (b) modified stacking sequence.

| Surface | Unrelaxed Energy ($Jm^{-2}$) | Relaxed Energy ($Jm^{-2}$) |
|---|---|---|
| {011} | 6.50 | 1.84 |
| {100} | 8.70 | 2.79 |
| {110} | 9.52 | 2.43 |
| {101}a | 8.37 | 2.11 |
| {101}b | 4.70 | 1.77 |
| {111}a | 4.04 | 1.73 |
| {111}b | 5.53 | 1.69 |

Table 4.16: Calculated surface energies of the low index "completed" surfaces of forsterite using two body potentials.

| Surface | Unrelaxed Energy ($Jm^{-2}$) | Relaxed Energy ($Jm^{-2}$) |
|---|---|---|
| {011} | 6.51 | 1.85 |
| {100} | 8.44 | 2.51 |
| {110} | 9.10 | 2.37 |
| {101}a | 8.01 | 2.19 |
| {101}b | 4.83 | 1.83 |
| {111}a | 3.97 | 1.83 |
| {111}b | 5.41 | 1.75 |

Table 4.17: Calculated surface energies of the low index "completed" surfaces of forsterite using three body potentials.

The total number of ions in surface region remains the same as the transfer is symmetric, i.e. each surface gains as many anions as it loses. The effect of this transfer on the surface structure and stacking sequence for the {101}b surface is shown in figures 4.32 and 4.31. We can see that the top oxide layer has transferred between the two surfaces formed on cleavage. This would appear to make the oxide layer the surface termination which it strictly is, however, for removal of the surface dipole considerations the magnesium ions are still considered to be the terminating layer. The same effect can be achieved for all other surfaces in which the $SiO_4$ tetrahedra are disrupted with the exception of the {001}a termination in which the silicon cations make up part of the terminating plane.

The energies of the surfaces containing "completed" tetrahedra are given in tables 4.17 and 4.16. For the two body potential the "completed" energies are, in the majority of cases, more stable than the corresponding surface energies in table 4.14. The differences are particularly large for some of the unrelaxed surface energies. In the case of the three body potentials all of the "completed" surface energies are more stable than the "incomplete" energies given in table 4.15. The {101}b termination now gives similar energies for both potentials. The completion of the tetrahedra has also stabilised this surface by 0.5 $Jm^{-2}$ for the two body potential and it is now predicted to be more stable than the {101}a surface. Thus by ensuring the surface silicon cations are totally saturated the orders of stability of the surfaces before and after relaxation have become independent of the potential used. Despite the various changes in each of the surface energies considered, the overall order of stability is unaffected and remains as that listed for the two body potential earlier.

The similarity of the calculated surface energies using either potential is reflected in the relaxed surfaces structures. In figures 4.33 and 4.34 we show the effect of relaxation on the structure of the {010} surface using the two and three body potentials respectively. We can see that in both cases the relatively small changes in the surface energies reflect a small change in structure. For both potentials the only major effect is the movement of the surface magnesium cation

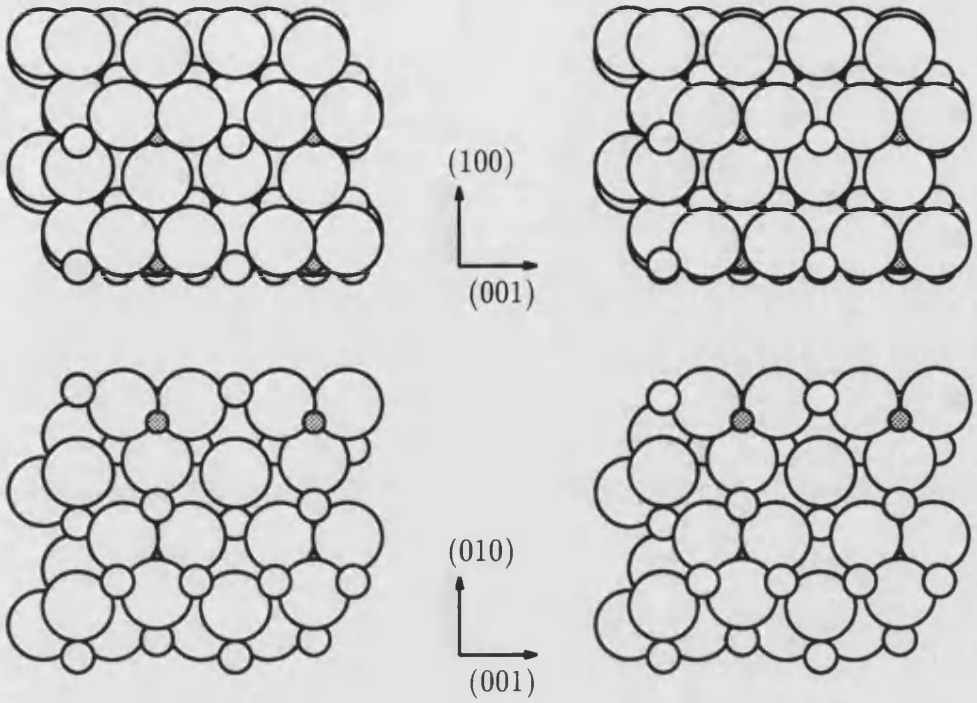


Figure 4.33: Relaxation of the {010} surface of forsterite using a two body potential. $Si^{4+}$ cations shown shaded.

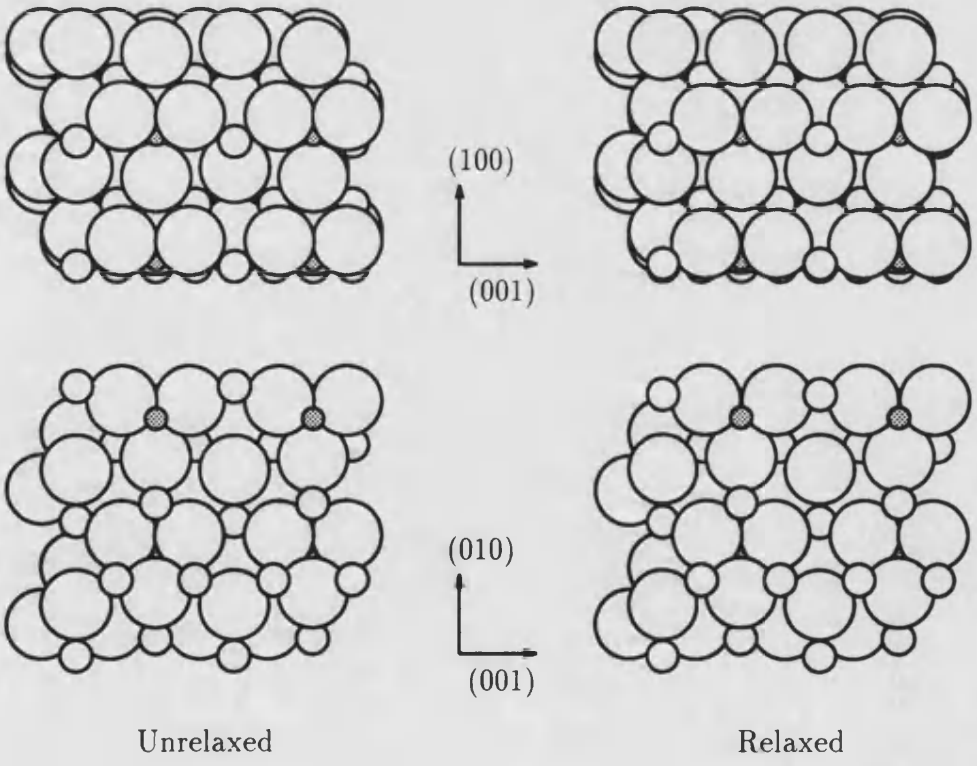


Figure 4.34: Relaxation of the {010} surface of forsterite using a three body potential. $Si^{4+}$ cations shown shaded.

into the surface. There is also some movement of the cations in the surface plane, relaxing in the direction of the surface anions. Overall both potentials predict very similar structures. The same is true of the other surfaces considered, in all case the relaxed structure are identical almost identical.

Despite this apparent agreement between the potentials, the small differences in the calculated surface energies do have some effect on the predicted equilibrium morphologies. These are given in figures 4.35 and 4.36 for the two and three body potentials respectively. For the unrelaxed surface energies there are large differences but these may be ignored as they cannot be compared to real crystals. The relaxed morphologies show a high degree of agreement. The major difference is that the morphology predicted using the three body results does not contain any {011} surface. This is due to the small differences in the {010} surface energies, the three body potential gives an energy 0.03 $Jm^{-2}$ more stable. Overall both potentials show good agreement with mineralogical samples [109, 112] although some higher index faces are normally present (these would normally exclude the {011} faces predicted by the two body potential) and most crystals are more elongated in the {001} direction. Also we predict a larger area of {111} faces than is normal but this can be put down to kinetic effects. Additionally some crystals show large {100} faces [108, 110] but again this may be due kinetic effects, forsterite twins along this face, or cleavage along this plane. Laboratory grown forsterite is normally produced using techniques that do not produce single crystals [126] and are therefore of no use in comparison to our results.

## 4.8 Summary

In this chapter we have presented the calculated surface energies for a range of materials. We have used equilibrium morphologies based on these calculated surface energies as a means of comparing with experiment. Such comparison in all but the case of spinel and magnetite showed good agreement with experimentally grown crystals. In the case of the two spinels considered the difference was attributed to kinetic effects.

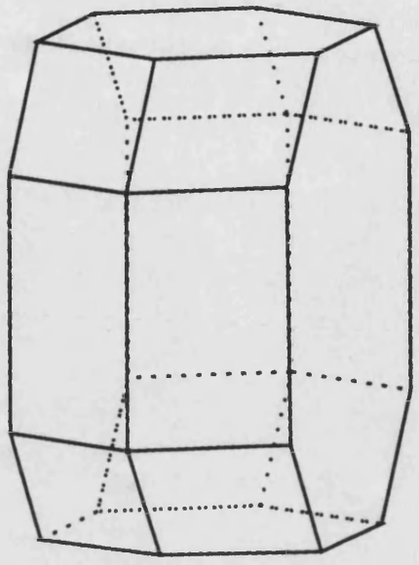

Unrelaxed

(001)

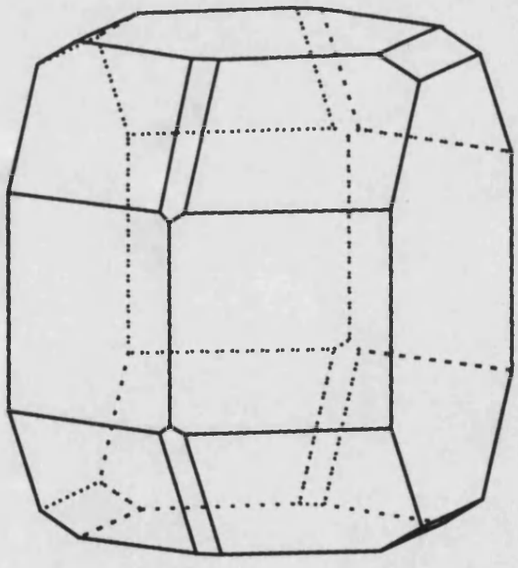

Relaxed

Figure 4.35: Predicted equilibrium morphology of forsterite base on surface energies calculated using a two body potential.

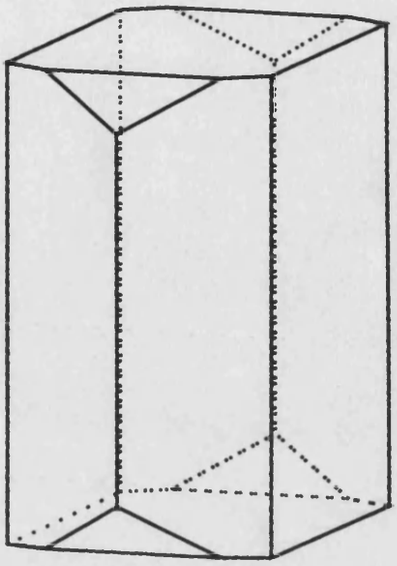

Unrelaxed

(001)

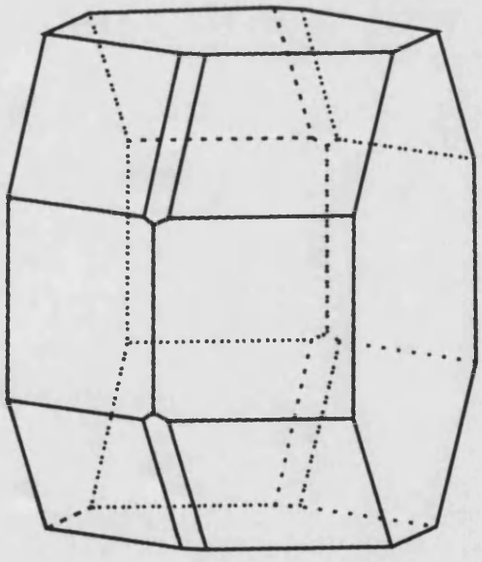

Relaxed

Figure 4.36: Predicted equilibrium morphology of forsterite base on surface energies calculated using a three body potential.

Throughout this chapter we have seen the importance of surface relaxation. The only surface that did not undergo significant relaxation was the {100} surface of FeO. For all the other surfaces considered large changes in surface energies were observed. The amounts of relaxation were surface specific. These changes affected the relative stabilities of crystal faces and therefore the predicted equilibrium morphologies.

For rutile, $TiO_2$, we found that before relaxation the {101} surface was the most stable. This disagrees with experiment where the {110} is thought to be the more stable [92]. However, on relaxation we find this surface became the most stable. The predicted equilibrium morphology for this compound also showed better agreement with real crystals for the relaxed surface energies.

In the case of spinel, $MgAl_2O_4$, we found that all three of the low index surface were dipolar. Vacancy arrangements at all three surfaces gave different surface energies. The most stable arrangement for each surface were determined. For the {110} and {111} surface we found that inversion of the cation distribution at the surface was required to obtain a minimum energy. As a results of these changes all the most stable surfaces were terminated in $Mg^{2+}$. This change in cation distribution at spinel type surfaces is important; catalytic processes using spinel structure materials are critically dependent on the cation distribution at the surface [127].

For magnetite, $Fe_3O_4$, an inverse spinel, we again found that surfaces terminating in divalent cation were the more stable. This was true except for the {100} surface where the tetrahedral sites occupied by a trivalent cation formed the more stable surface. The morphology of experimentally grown magnetite crystals is size dependent, therefore, the difference between the predicted and real morphologies was attributed to kinetic effects.

Finally we consider forsterite, $Mg_2SiO_4$, using both a two and three body potential. We discovered that disruption of the $SiO_4$ tetrahedra reduced the stability of several surfaces. Also we found that the dipolar surfaces had energies similar to

the non-dipolar surfaces. "Completion" of the silicon tetrahedra was seen to stabilise some surfaces, therefore strict planar cleavage had to be abandoned. Overall the differences in the surface energies calculated for the two types of potential were small. A more important consideration than the potential used is the maintenance of silicon saturation. Comparison between the predicted equilibrium morphology and mineralogical crystals was good.

# Chapter 5

## The perfect and defective surfaces of hematite

In the previous chapter we presented the calculated energies and structures of the surfaces of a large range of oxides. In the remainder of this thesis we shall focus on the surfaces of and grain boundaries in hematite.

Defects at surfaces play a important role in many surface properties, such as sintering, densification and a range of catalytic properties. Therefore in this chapter after considering the perfect surfaces using the same approach as in the previous chapter we shall present some calculations on the effect of defects at the low index hematite surfaces. We shall consider the vacancy formation energies close to some of the low index surfaces before going on to investigate isovalent impurity segregation to all of the low index surfaces of hematite. We shall start, however, with a detailed description of the hematite crystal structure.

### 5.1 The crystal structure of $\alpha Fe_2O_3$

Hematite is a member of the group of oxides commonly known as the corundum structured oxides. This group contains many oxides of the type $M_2O_3$ (sesquioxides) such as $Cr_2O_3$, $Ti_2O_3$, $V_2O_3$, and, of course, corundum itself $Al_2O_3$. The structure of these oxides is based on a hexagonal close packing of oxygen ions, with the cations occupying two thirds of the octahedral holes. As the structure is hexagonally close packed we might naively expect it to have hexagonal symmetry; however this is not the case. Large distortions occur in the cation sublattice lowering the space group symmetry to $R\bar{3}c$ and resulting in a variation in the cation-anion bond distances.

The nature of these distortions can clearly be understood if we consider the lattice packing parallel to the c-axis, figure 5.1. The packing of the oxygen sublattice produces columns of oxygen octahedra of which two out of three are occupied

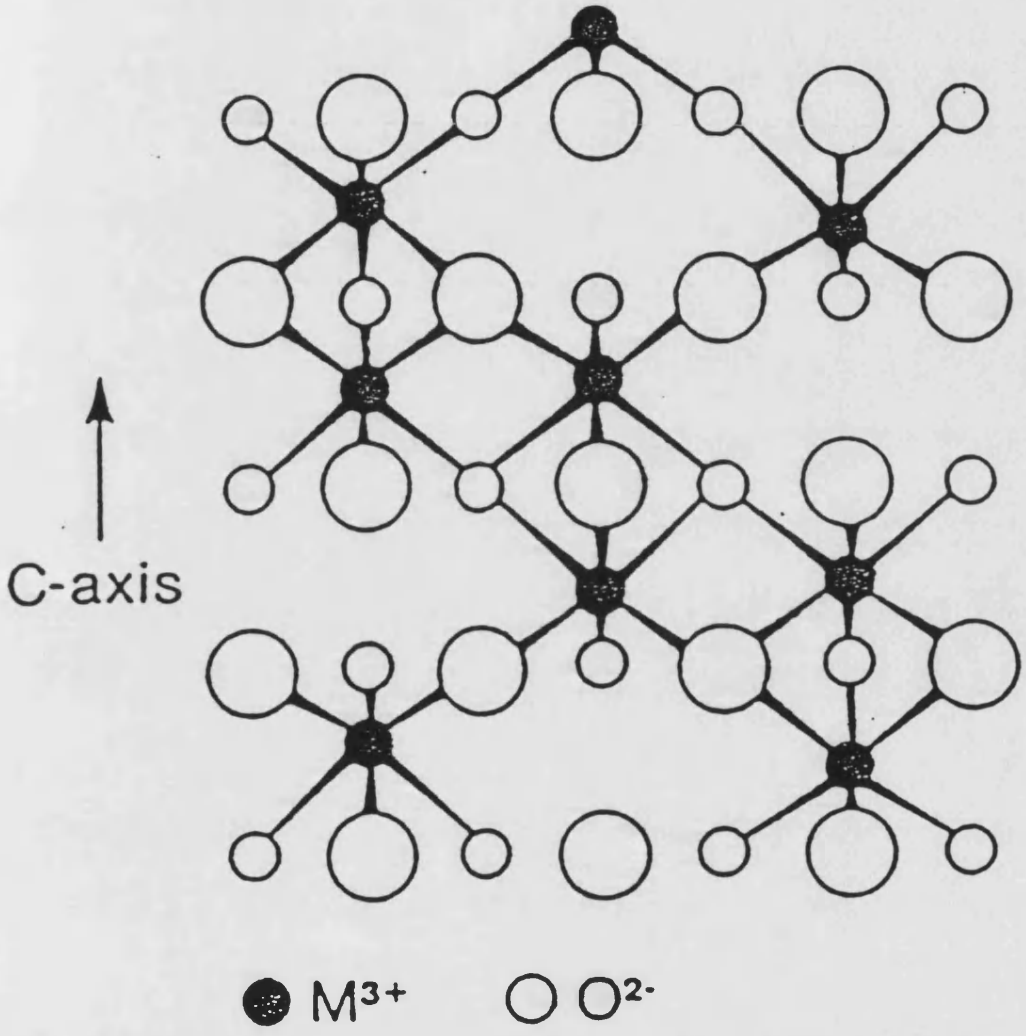


Figure 5.1: The corundum lattice structure.

by cations. This causes an inequivalence whereby one anion plane will be shared by two cations, coupled with two anion planes having only one cation nearest neighbour (n.n.). If this is related to the coordination number of individual ions the magnitude of the deviation from true hexagonal form can be seen. Due to the stoichiometric ratio of cations to oxygen, each cation will have 6 oxygen n.n., while each oxygen will have 4 cation n.n. . For each cation site the nearest neighbour oxygen will be split into two groups of three, one group will be face shared with another cation occupied octahedra, while the other face will be shared with an unoccupied octahedra. This produces two distinct observable cation-anion bond distances. In the case of hematite, 0.210nm for the cation to a shared anion face and 0.196nm for the cation to an unshared anion face [128]. This is simply rationalised by the repulsive nature of like charges i.e. $Fe^{3+} - Fe^{3+}$, causing the cations to relax away from each other.

Each oxygen site is surrounded by 4 cation n.n., which can be thought of in two different ways. Either as tetrahedrally coordinated oxygen or as oxygen ions surrounded by a trigonal bi-pyramid of cations from which two cations are missing. Allied to the cation repulsion described above the anions distort by moving towards the prism edge shared by two cations. Thus the anions are symmetrically coordinated with respect to the hexagonal c-axis, adopting a prefect packing sequence in this direction, but distorting perpendicular to the c-axis. This does not apply to the cation sub-lattice which only distorts parallel to the c-axis. This may be summarised by saying that one third of the cation sites are displaced above the midpoint of the anion planes, another third are displaced below the midpoint, while the remaining third are vacant interstitial sites which are symmetrical with respect to the oxygen planes.

## 5.2 Perfect Surface energies

The hexagonal closed packed nature of $\alpha Fe_2O_3$ leads to a large number of low index planes of which we shall consider the lowest five, the basal {0001}

plane and four others. Perpendicular to the basal plane are planes related to the hexagonal prism. The two lowest index are the hexagonal prism face itself, the $\{10\bar{1}0\}$, and the diagonal of the prism, the $\{11\bar{2}0\}$. The primitive unit cell of $\alpha Fe_2O_3$ is rhombohedral and therefore we shall consider the two possible primitive rhombohedra, the $\{01\bar{1}2\}$ and the $\{10\bar{1}1\}$ planes. Several corundum structured oxides have been observed to cleave along the $\{01\bar{1}2\}$ face [108], although no simple cleavage plane has been observed for hematite or corundum itself.

The stacking sequences for these five planes are illustrated in figure 5.2. As we have seen in the previous chapter, neutral repeats are rare except in the case of cubic structured oxides and, therefore, the termination of each surface has been chosen such that there is no net dipole perpendicular to the surface. The effects of the distortion of the corundum structure from pure hexagonal described above are well illustrated by the chose of terminating planes. In the case of the basal plane, $\{0001\}$, the "rumpling" of the cation plane in the $c$ direction leads to a cation terminated surface. Such a termination has been observed directly using scanning tunnelling microscopy [129]. The prism planes, the $\{10\bar{1}0\}$ and the $\{11\bar{2}0\}$, show the distortion of the anion sublattice perpendicular to the c-axis. The $\{10\bar{1}0\}$ plane has a very narrow repeat, almost representing a neutral repeat unit, but some of the anions deviate slightly from the mean of the plane. The $\{11\bar{2}0\}$ surface terminates with a plane of anions which are found to be not quite co-planar.

The rhombohedral planes, the $\{01\bar{1}2\}$ and the $\{10\bar{1}1\}$, both terminate in an anion layer, however unlike the basal and prism faces these surfaces are not close packed. The view from above the $\{01\bar{1}2\}$ surface is shown in figure 5.3; the surface anions form zig-zag rows separating the cations just below the surface. The surface cations are five fold coordinated in contrast to the three fold coordination at the basal surface. The $\{10\bar{1}1\}$ plane shows a similar surface structure, figure 5.4, but with isolated surface anions, the cations at the surface are four coordinate.

The surface energies of these five lowest index planes given above were calculated using the empirically derived potential model of Catlow and Lewis [50]

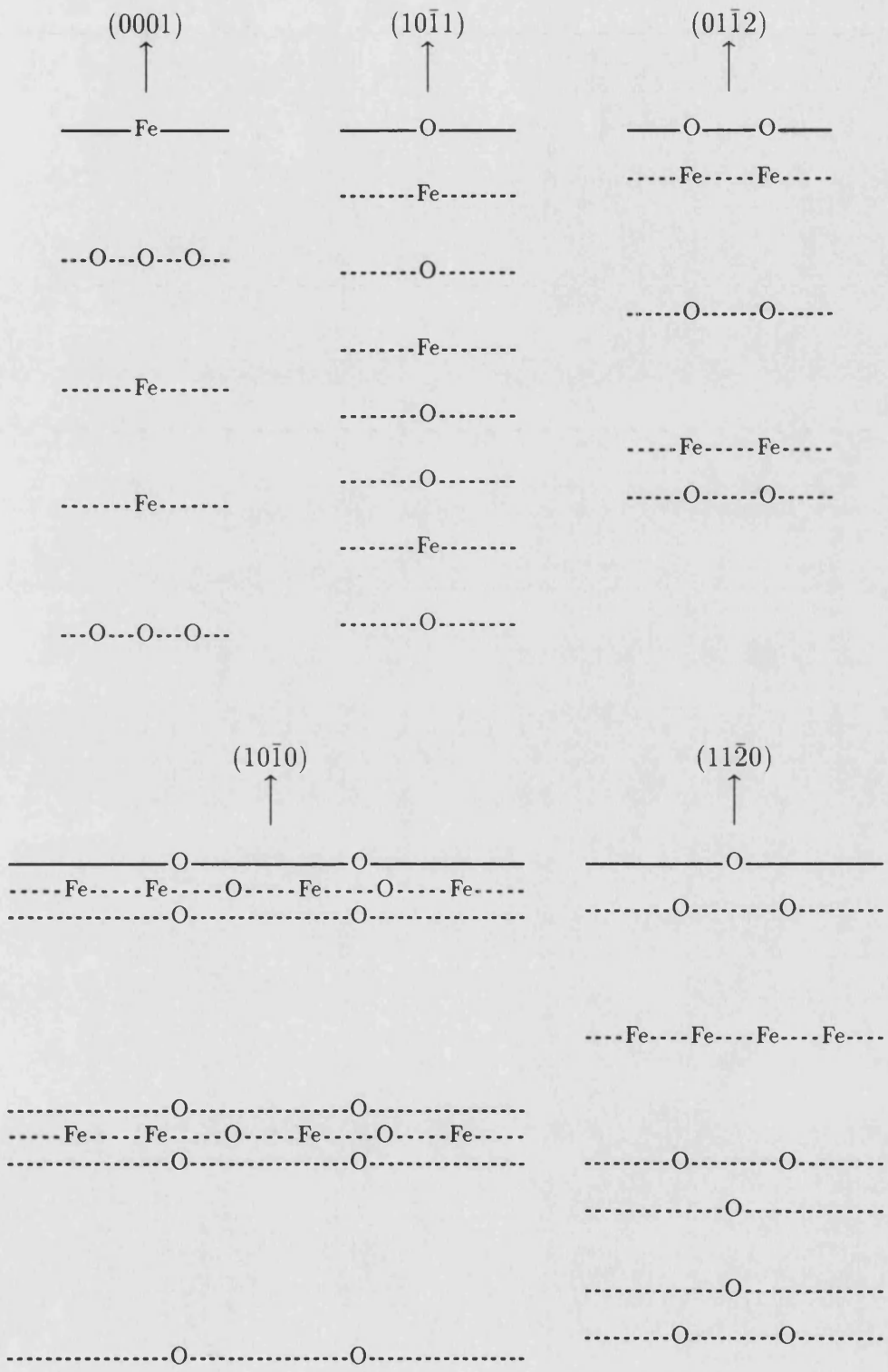


Figure 5.2: Stacking sequences for the low index surfaces of Hematite $\alpha Fe_2O_3$.

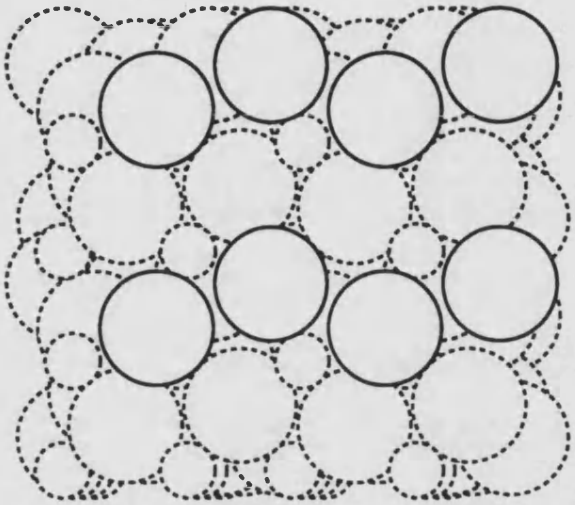

Figure 5.3: The structure of the $\{01\bar{1}2\}$ surface. Terminating anions shown in full lines, unit cell scaled $2 \times 2$.

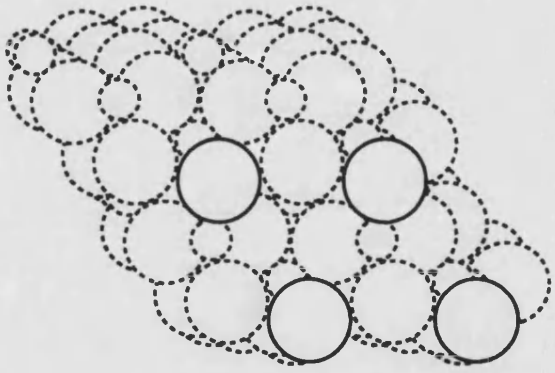

Figure 5.4: The structure of the $\{10\bar{1}1\}$ surface. Terminating anions shown in full lines, unit cell scaled $2 \times 2$.

| Surface | Unrelaxed Energy ($Jm^{-2}$) | Relaxed Energy ($Jm^{-2}$) |
|---|---|---|
| $\{0001\}$ | 5.04 | 2.32 |
| $\{10\bar{1}0\}$ | 5.46 | 2.24 |
| $\{10\bar{1}1\}$ | 4.82 | 2.85 |
| $\{01\bar{1}2\}$ | 2.86 | 1.95 |
| $\{11\bar{2}0\}$ | 3.89 | 2.32 |

Table 5.1: Calculated surface energies of $\alpha Fe_2O_3$.

and the methods described in the previous chapter. The calculated relaxed and unrelaxed surface energies are given in table 5.1. As in the previous chapter all the surfaces undergo some relaxation; the degree of relaxation being surface specific. In this case we can see that the $\{10\bar{1}0\}$ plane has the largest change in surface energy of 2.71 $Jm^{-2}$ or 59% whereas the $\{01\bar{1}2\}$ has the lowest change of 0.91 $Jm^{-2}$ or 32%. As a result of these varying amounts of relaxation, the order of stability before and after relaxation is different. Before relaxation the order of stability is

$$\{01\bar{1}2\} < \{11\bar{2}0\} < \{10\bar{1}1\} < \{0001\} < \{10\bar{1}0\}$$

and after relaxation it becomes

$$\{01\bar{1}2\} < \{10\bar{1}0\} < \{0001\} = \{11\bar{2}0\} < \{10\bar{1}1\}$$

The two planes exhibiting the greatest change in surface energy are the $\{10\bar{1}0\}$ and the basal $\{0001\}$. This is due to the large amount of relaxation that occurs at these surfaces. The effect of this relaxation on the stacking sequence $\{0001\}$ is illustrated in figure 5.5. It can be seen that in the case of the basal plane the surface contracts. Before relaxation the interplanar spacings are equal, but after relaxation we see a large reduction in the first cation-anion interplanar spacing of 43% to 0.4Å, with an increase in the second cation-anion interplanar spacing of 7% to 0.8Å. The changes in interplanar spacing are essentially zero by the third repeat unit below the surface. The effect on the surface structure of this relaxation is better illustrated if we consider the structure at an ionic level, figure

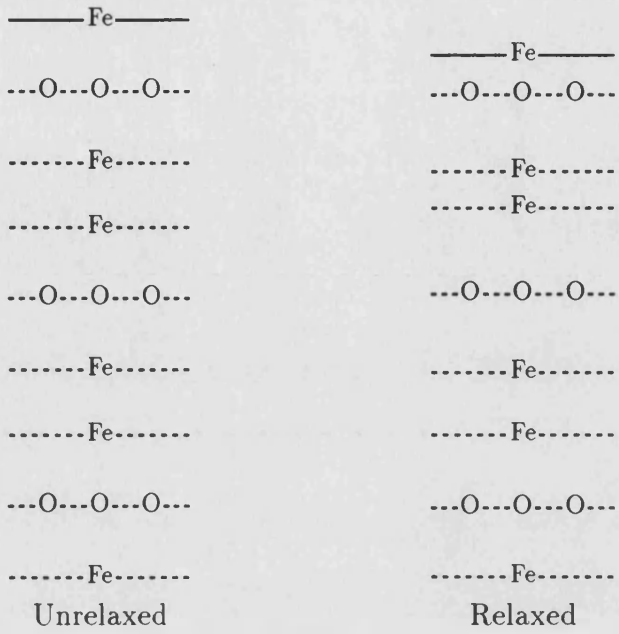


Figure 5.5: Effect of surface relaxation on stacking sequence perpendicular to the basal {0001} surface of hematite.

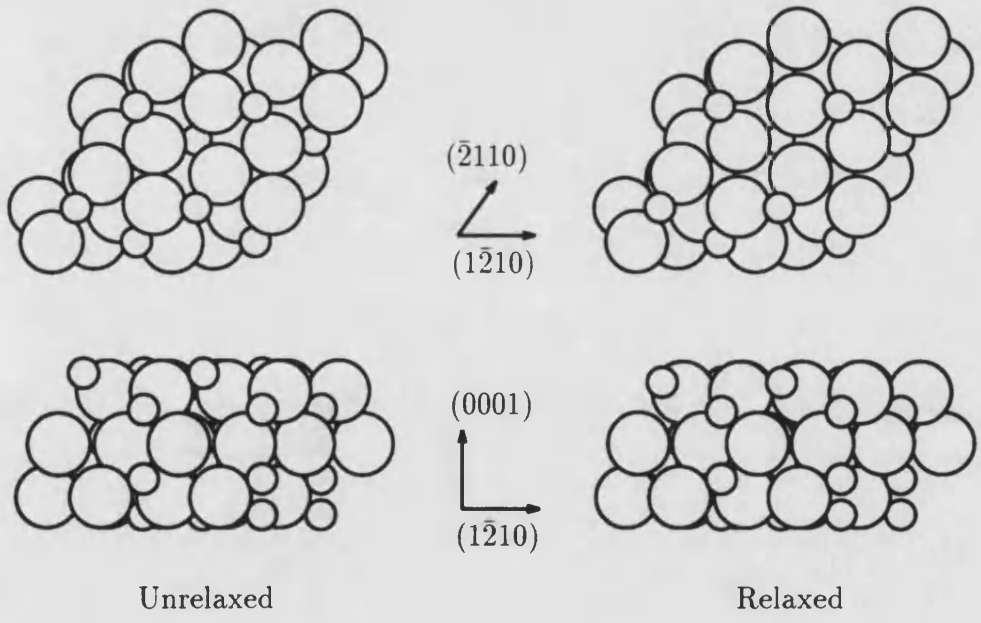


Figure 5.6: Effect of surface relaxation on the ionic structure of the basal {0001} surface of hematite.

5.6. In the unrelaxed structure the cations at the surface protrude above the much larger anions. However on relaxation the cations are drawn into the surface and now effectively lie just below it. This relaxation effect may in part explain the unexpected inertness of the $\alpha Fe_2O_3$ basal surface to the chemisorption of $O_2$, $H_2$, $H_2O$ and $SO_2$ observed by Kurtz and Henrich [130], the cations in the relaxed structure are being shielded to some extent from the adsorbate by the surface anions.

In contrast to the basal plane, the relaxation of the $\{10\bar{1}0\}$ planes is much more complex, figure 5.7. The surface as a whole dilates with the first interplanar spacing increasing by 233% to 0.5Å. In addition to this dilation the mixed cation-anion plane is seen to "rumple", splitting the plane. This "rumpling" can be understood if we examine the surface shown in figure 5.8 where the uppermost surface anions are shown with a dotted outline. We can see that the cations at the surface are split into two groups, those coordinated to the uppermost anion and those not coordinated to these anions. On relaxation we see that the anions move a considerable distance and are now coordinated to two cations each. The cations which were formally coordinated to these cations have moved upwards slightly more than the formally uncoordinated cations. The second repeat unit below the surface shows more pronounced "rumpling" but by the time we reach the fifth repeat unit below the surface the relaxation is negligible. This splitting of the cations nearest the surface into two types is important when considering impurity segregation as we shall see latter in this chapter.

Mackrodt et al [131] have also calculated the surface energies of the five lowest index planes of hematite using a set of non-empirical potentials. A comparison of the results of Mackrodt et al with those in table 5.1 indicates some potential sensitivity in these surface calculations. Both sets of results predict the same order of stability for the unrelaxed surfaces of hematite. In fact atomistic calculation on other corundum structured oxides such as those of Tasker on $\alpha Al_2O_3$ [22] and Lawrence on $\alpha Cr_2O_3$ [132] all predict the same order of stability for unrelaxed

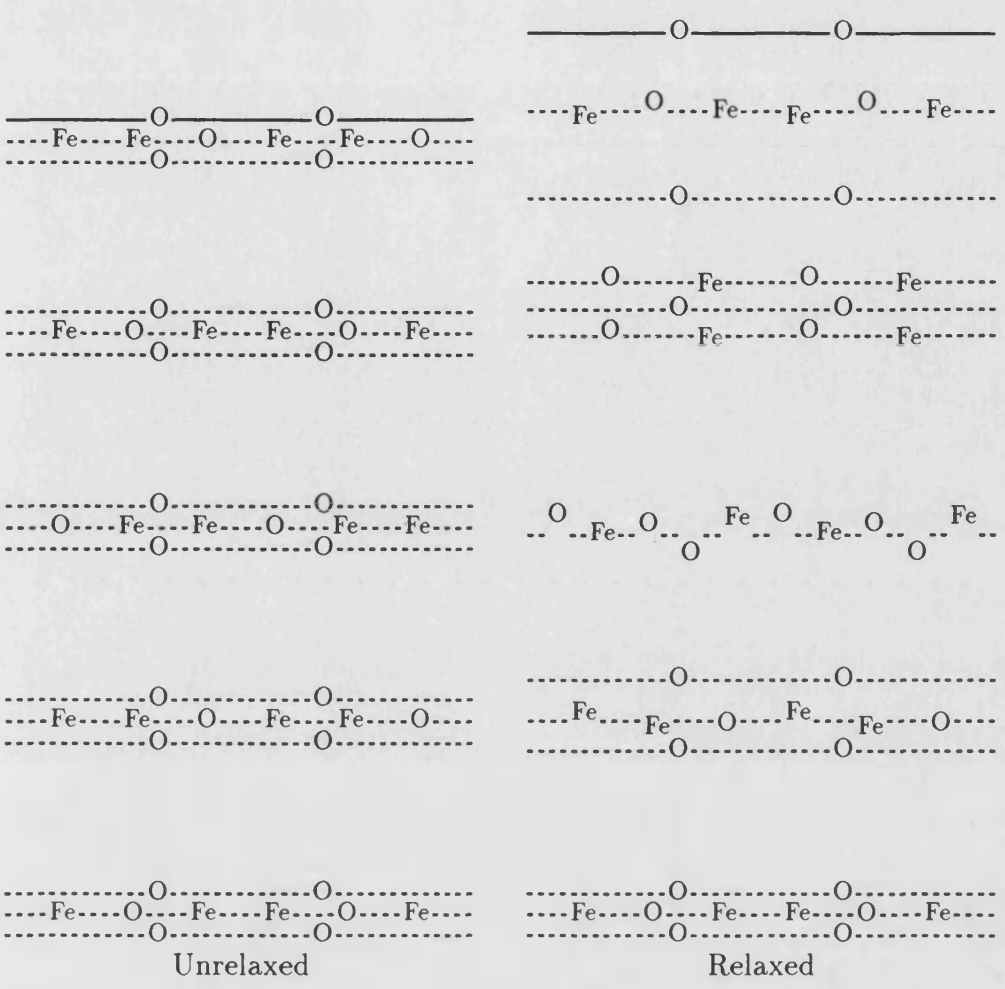


Figure 5.7: Effect of surface relaxation perpendicular to the $\{10\bar{1}0\}$ surface of hematite.

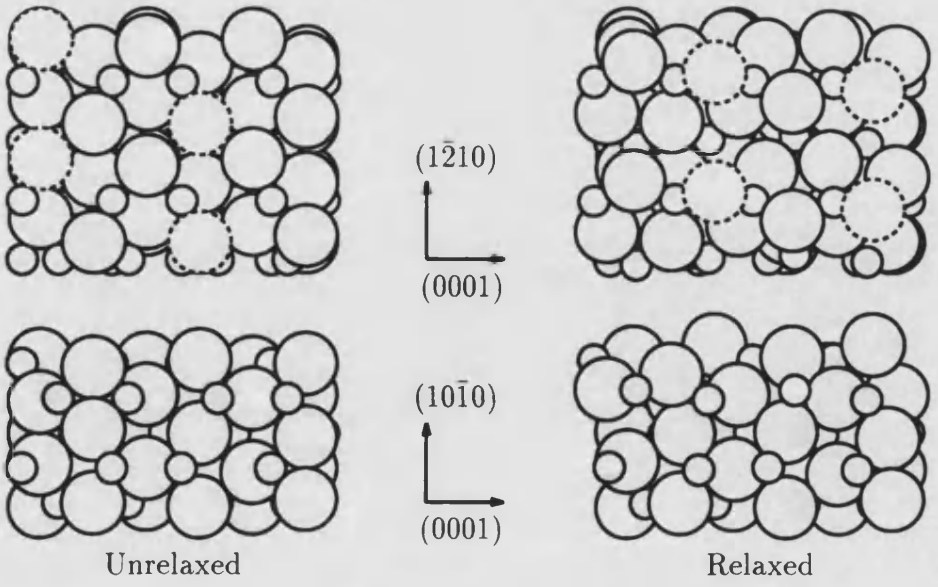


Figure 5.8: Effect of surface relaxation on the ionic structure of the $\{10\bar{1}0\}$ surface of hematite.

surfaces. The same order has also been obtained using the periodic bond chain technique [133] by Hartman [134] and Bessières and Baro [135]. On relaxation however, Mackrodt et al predict an order of stability different to that given in 5.1. They obtained an order of

$$\{01\bar{1}2\} \approx \{0001\} < \{11\bar{2}0\} < \{10\bar{1}0\} \approx \{10\bar{1}1\}$$

with surface energies in the range of 1.47 to 2.41 $Jm^{-2}$. Similar potential sensitivity was also noted by Lawrence [132] in his own calculations on chromia and in comparing the results of Tasker [136] and Mackrodt [131] on the surfaces of alumina. This sensitivity has been attributed to a failure of the empirical potentials when the interionic separations deviate from their bulk values as does occur in the relaxation of corundum structured oxide surfaces. However in the case of hematite we note that in the Mackrodt calculations the contraction of the basal plane is negligible, whereas in other reported calculations (including the $\alpha Al_2O_3$ calculations of Mackrodt [131]) on corundum structured oxides using either empirical or non-empirical potentials [132, 137] where relaxed basal structures are reported the contraction is large and more in line with that shown in figure 5.5.

Comparing the equilibrium morphologies predicted by Mackrodt, figure 5.9, and those predicted from the results in table 5.1, figure 5.10, we see that this difference in the order of stability can have large effects on an observable phenomena. Both sets of results give basically the same morphology for the unrelaxed surfaces. For the relaxed structures, however, Mackrodt et al predict a morphology consisting almost totally of the $\{01\bar{1}2\}$ plane and the basal $\{0001\}$ plane with small areas of $\{10\bar{1}1\}$. We, however, predict a more complex morphology which is also dominated by the $\{01\bar{1}2\}$ surfaces but additionally contains both the prism planes, the $\{10\bar{1}0\}$ and $\{11\bar{2}0\}$. Experimental crystals consisting of just the rhombohedral and basal plane have been reported [139], but the morphologies of these crystals were very dependent on the growth conditions. A large group of data on mineral hematite [140, 141] has been examined by Hartman [142] who came to the

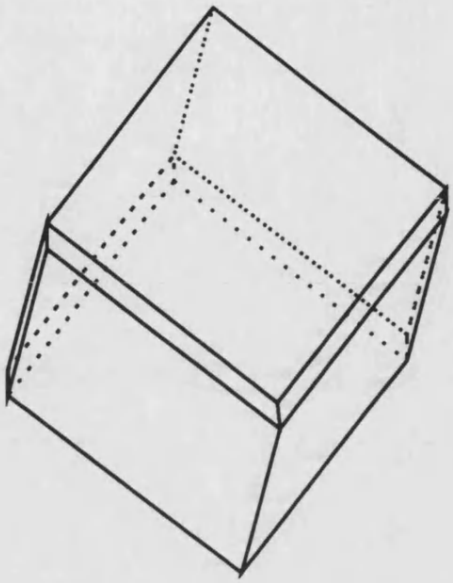

Unrelaxed

(0001)

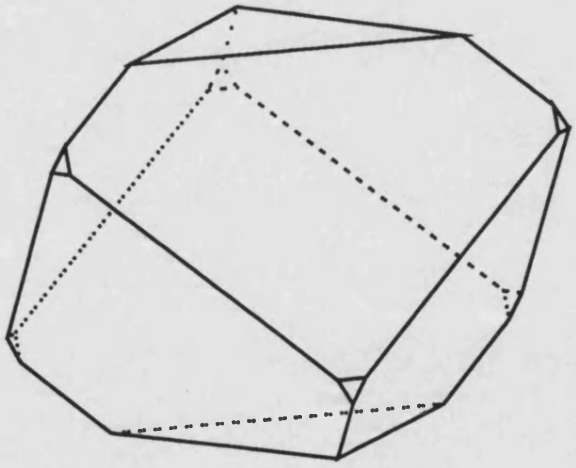

Relaxed

Figure 5.9: Predicted equilibrium morphology of hematite based on the calculated surface energies of Mackrodt et al [131].

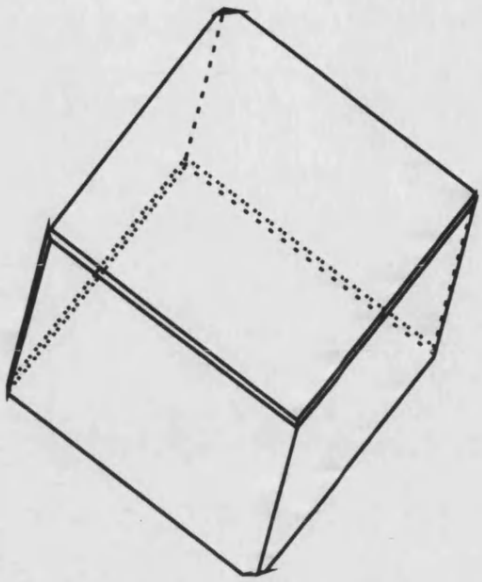

Unrelaxed

(0001)

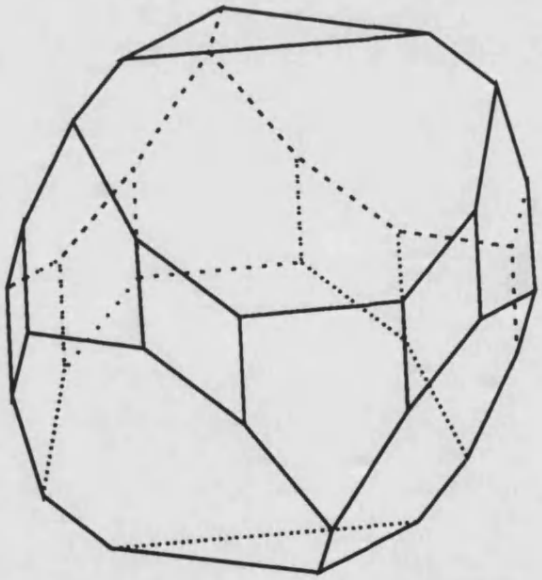

Relaxed

Figure 5.10: Predicted equilibrium morphology of hematite based on the calculated surface energies given in table 5.1.

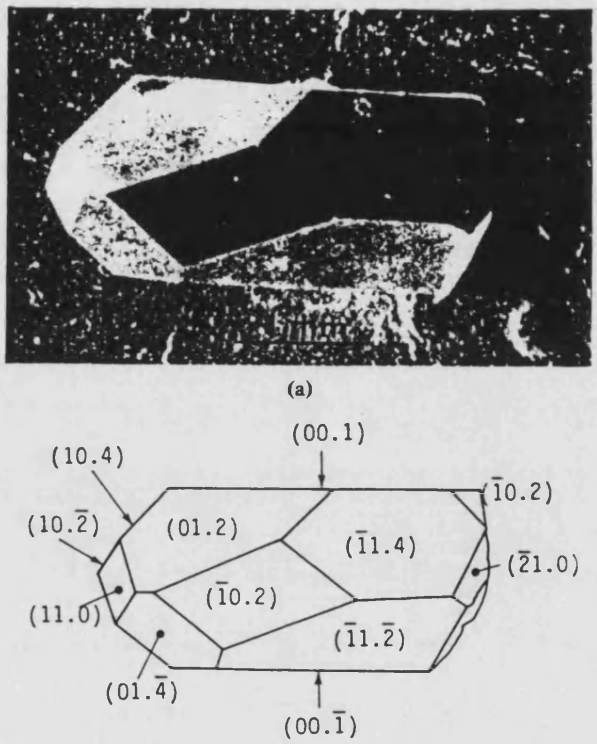


Figure 5.11: Hematite crystal prepared using gaseous phase transport reaction by Bessières and Baro [138].

conclusion that the most important faces are the {0001}, {01$\bar{1}$2}, {11$\bar{2}$3}, {10$\bar{1}$4} and {11$\bar{2}$0} with the {10$\bar{1}$0} occurring only rarely. The morphology we predict in figure 5.10 matches these results well although we are of course are missing the higher index planes. Also the {10$\bar{1}$0} is probably more prominent than we should expect from the mineral data. Our morphology also shows good agreement with crystals prepared by Bessières and Baro [138] using a gaseous phase transport reaction, see figure 5.11. Although again we are missing the higher index surfaces, the {10$\bar{1}$0} surfaces are not present in their crystals and the basal plane is more prominent than is predicted figure 5.11. Overall we can say that our predicted morphology matches the experimental data more closely that that predicted by Mackrodt.

## 5.3 Vacancy formation energies near the low index surfaces of $\alpha Fe_2O_3$

Vacancies at surfaces can have a large effect in the chemisorption and therefore rates of catalysis [143]. Surface also act as sinks of vacancies and intersitials and therefore the electric potential in the interior of an ionic crystal is related to the difference between the vacancy energies in the surface and the bulk [144]. Here we present the calculated formation energies for both cation and anion vacancies near the basal and {01$\bar{1}$2} surfaces of hematite and show how these may be compared to the bulk values.

The energies of cation and anion vacancies near the {0001} and {01$\bar{1}$2} surface were calculated using the computer code CHAOS, tables 5.2-5.5. The defect energies were calculated using MIDAS relaxed surfaces as the reference state. Point defects were created on each cation or anion site on successive planes below the surface until the vacancy energies converged to a constant value. Before direct comparison with the bulk vacancy energies can be made two surface specific effects must be taken into account.

Firstly, the Madelung energy of a defect near to a surface is significantly different from those of the same defect in the interior of the crystal, see tables 5.2-5.5.

| Plane | Unrelaxed Energies ($kJmol^{-1}$) | | | Relaxed |
|---|---|---|---|---|
| | Madelung | Short Range | Total | Energy ($kJmol^{-1}$) |
| 0 | 10748.81 | -1698.95 | 9049.86 | 6110.49 |
| 1 | 11398.84 | -1760.49 | 9638.35 | 6193.39 |
| 2 | 11085.45 | -1383.86 | 9701.58 | 6144.28 |
| 3 | 11134.53 | -1486.30 | 9648.23 | 5963.31 |
| 4 | 10992.83 | -1429.62 | 9563.20 | 5944.62 |
| 5 | 11054.41 | -1439.06 | 9615.35 | 6084.92 |
| 6 | 11091.42 | -1474.02 | 9617.40 | 6108.99 |
| 7 | 11092.21 | -1467.21 | 9625.00 | 6096.56 |
| 8 | 11102.70 | -1469.54 | 9633.15 | 6104.79 |
| 10 | 11092.02 | -1465.88 | 9626.15 | 6091.29 |
| 12 | 11092.27 | -1466.72 | 9625.55 | 6087.16 |
| 15 | 11093.07 | -1466.89 | 9626.18 | 6074.98 |
| Bulk | 10126.49 | -1466.81 | 8659.68 | 5101.64 |

Table 5.2: Unrelaxed and relaxed energies of cation vacancies near to the {0001} surface of hematite.

| Plane | Unrelaxed Energies ($kJmol^{-1}$) | | | Relaxed |
|---|---|---|---|---|
| | Madelung | Short Range | Total | Energy ($kJmol^{-1}$) |
| 1 | 4343.69 | -1087.71 | 3255.98 | 1592.36 |
| 2 | 4083.30 | -862.13 | 3221.16 | 1534.76 |
| 3 | 4182.33 | -913.31 | 3269.02 | 1581.06 |
| 4 | 4160.13 | -906.18 | 3253.95 | 1572.13 |
| 5 | 4154.56 | -901.67 | 3252.89 | 1568.94 |
| 6 | 4157.36 | -902.85 | 3254.51 | 1567.43 |
| 7 | 4157.51 | -903.09 | 3254.43 | 1564.41 |
| 8 | 4157.24 | -902.94 | 3254.30 | 1560.60 |
| 10 | 4157.31 | -902.94 | 3254.37 | 1557.28 |
| Bulk | 4801.60 | -903.93 | 3897.67 | 2192.31 |

Table 5.3: Unrelaxed and relaxed energies of anion vacancies near to the {0001} surface of hematite.

| Plane | Unrelaxed Energies ($kJmol^{-1}$) | | | Relaxed |
|---|---|---|---|---|
| | Madelung | Short Range | Total | Energy ($kJmol^{-1}$) |
| 1 | 9686.38 | -1510.50 | 8175.88 | 4775.53 |
| 2 | 9686.39 | -1510.51 | 8175.88 | 4775.48 |
| 3 | 9652.03 | -1407.38 | 8244.65 | 4729.67 |
| 4 | 9652.04 | -1407.39 | 8244.65 | 4729.66 |
| 5 | 9795.27 | -1500.26 | 8295.01 | 4777.49 |
| 6 | 9795.27 | -1500.27 | 8295.01 | 4777.49 |
| 7 | 9727.60 | -1469.11 | 8258.48 | 4751.02 |
| 8 | 9727.59 | -1469.11 | 8258.48 | 4751.01 |
| 9 | 9722.64 | -1460.37 | 8262.27 | 4739.56 |
| 10 | 9722.64 | -1460.37 | 8262.27 | 4739.56 |
| 11 | 9734.05 | -1466.52 | 8267.53 | 4743.41 |
| Bulk | 10126.49 | -1466.81 | 8659.68 | 5101.64 |

Table 5.4: Unrelaxed and relaxed energies of cation vacancies near to the $\{01\bar{1}2\}$ surface of hematite.

| Plane | Unrelaxed Energies ($kJmol^{-1}$) | | | Relaxed |
|---|---|---|---|---|
| | Madelung | Short Range | Total | Energy ($kJmol^{-1}$) |
| 1 | 4923.37 | -963.60 | 3959.77 | 2354.86 |
| 2 | 5039.72 | -853.48 | 4186.24 | 2520.14 |
| 3 | 5068.29 | -939.76 | 4128.53 | 2530.41 |
| 4 | 5029.90 | -875.65 | 4154.25 | 2474.44 |
| 5 | 5068.99 | -911.92 | 4157.06 | 2485.15 |
| 6 | 5073.49 | -903.86 | 4169.62 | 2497.97 |
| 7 | 5065.66 | -905.05 | 4160.62 | 2477.88 |
| 8 | 5063.95 | -902.74 | 4161.20 | 2480.64 |
| 9 | 5062.96 | -903.18 | 4159.79 | 2476.04 |
| 10 | 5063.22 | -902.80 | 4160.43 | 2475.67 |
| 11 | 5063.24 | -902.89 | 4160.35 | 2474.34 |
| 12 | 5063.42 | -902.86 | 4160.56 | 2472.61 |
| Bulk | 4801.60 | -903.93 | 3897.67 | 2192.31 |

Table 5.5: Unrelaxed and relaxed energies of anion vacancies near to the $\{01\bar{1}2\}$ surface of hematite.

This is due to the different methods by which the boundary conditions are defined in 3-dimensional bulk and 2-dimensional surface problems. For bulk defects, the outer region of the crystal is considered to be a polarisable continuum extending to infinity, i.e. the defect will never "feel" the effect of the terminating interface. For defects near surfaces, however, the terminating interface is an inherent part of the calculation. As we have seen surfaces are not strict bulk terminations, they relax. This relaxation leads a surface dipole layer which will induce an electrostatic potential which extends infinitely below the surface into the bulk. This leads to a shift in the Madelung field when the surface is taken into account [145] which can be quantified by the expression "$qV$", where $q$ is the full ionic charge of the ion involved and $V$ is the surface dipole induced electrostatic potential. The shift $V$ will be dependent on the magnitude of the displacement of relaxed ions at each surface and will therefore be surface specific.

Previous work on the MgO {100} surface [146] showed a perturbation in the cation Madelung field of 14.50 kJmol$^{-1}$, while the perturbation in the anion Madelung field was equal and opposite at -14.50 kJmol$^{-1}$. For the hematite surface the shifts in the Madelung fields are much greater due to the larger amount of surface relaxation. For the basal {0001} surface we can see from table 5.2 that the shift in cation vacancy Madelung energy is 967 kJmol$^{-1}$ and from table 5.3 the shift in the anion vacancy Madelung energy is -644 kJmol$^{-1}$. Similar large values have been reported by Lawrence [132] for vacancies near the basal surface of chromia. The shifts for the rhombohedral $\{01\bar{1}2\}$ surface are much lower as a results of the smaller amount of relaxation that occurs at this surface. The shift for the cation vacancy is -392 kJmol$^{-1}$, table 5.4, and for the anion vacancy it is 262 kJmol$^{-1}$, table 5.5.

The second extra effect that needs to be considered for point defects near surfaces is the polarisation due to the image charge [147]. In a material with a dielectric constant $\epsilon_1$ the image charge $Q_{image}$ of a defect with net charge $Q_{def}$ has

a magnitude give by [48]

$$Q_{image} = Q_{def} * \left(\frac{\epsilon_1 - \epsilon_2}{\epsilon_1 + \epsilon_2}\right)$$

where $\epsilon_2$ is the dielectric constant of a vacuum or gas in the case of surfaces. The position of this image charge is determined by reflection of the defect in a plane at the surface of the crystal. For atomistic calculations the definition of the surface is ambiguous. It is therefore assumed that it lies half an interplanar spacing above the top plane of ions. This gives reasonable convergence of the lattice sums with region size and is consistent with the methods used for calculating the electric field in region II of the crystal.

The effect of the image charge at the oxide surfaces is to repel charged defects from the boundary. This reduces the stability of a charged defect as it approaches the surface. By applying the methods of continuum electrostatics the force on the defect at a distance $x$ below the surface of a dielectric can be shown to be given by [146]

$$F = -\frac{Q_{def}Q_{image}}{\epsilon(2x)^2}$$

Therefore the energy required to move a defect from the bulk to a distance $d$ below the surface is

$$E_{pol} = \int_{-\infty}^{-d} F dx = \frac{Q_{def}Q_{image}}{4\epsilon d}$$

It can be seen that as the defect approaches the surface the contribution of the polarisation to the defect energy increases. The dotted lines in figures 5.12-5.15 represent a $1/r$ continuum approximation from which it can be seen that the agreement between our atomistic calculation and the continuum approximation is good at a reasonable distance below the surface but the approximation breaks down in the near surface region.

The calculated relaxed cation and anion vacancy formation energies near the basal surface are given in tables 5.2 and 5.3 and are plotted as a function of

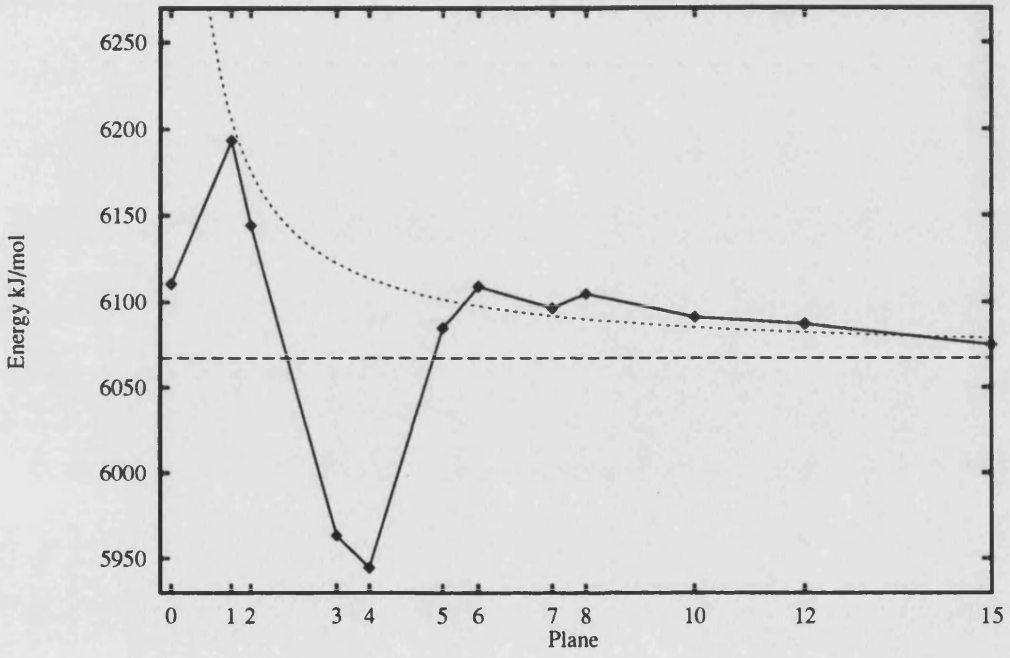


Figure 5.12: Plot of the cation vacancy energies as a function of distance from the {0001} surface. Horizontal dashed line - bulk energy. Dotted line - continuum approximation.

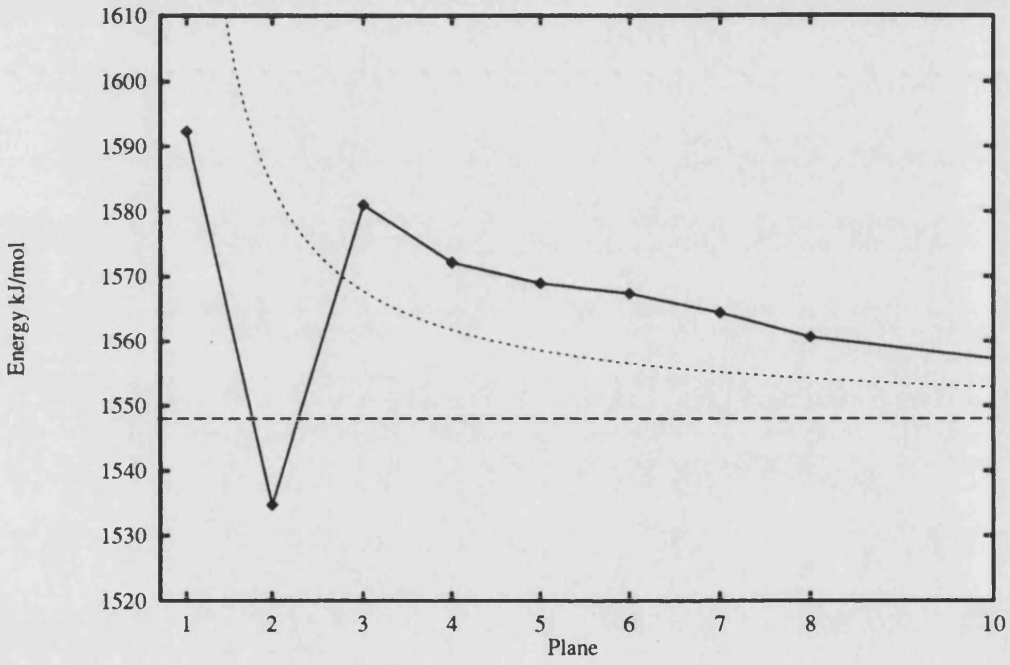


Figure 5.13: Plot of the anion vacancy energies as a function of distance from the {0001} surface. Horizontal dashed line - bulk energy. Dotted line - continuum approximation.

distance below the surface in figures 5.12 and 5.13 respectively. Also included are the bulk vacancy formation energies adjusted for the surface Madelung shift and a plot of a $1/r$ continuum which converges to the adjusted bulk value as the distance from the surface increases. Neither of these plots exhibit the behaviour that was observed in previous calculations by Duffy et al [146] for the {001} MgO surface. They observed a maximum in the vacancy formation energy in the subsurface layer (plane 3 for the cation vacancy, and plane 2 for the anion vacancy). The cation vacancies shown in figure 5.14 show a maximum of 126 $kJmol^{-1}$ above the bulk value at plane 1 but then the formation energy falls to a minimum of 123 $kJmol^{-1}$ below the bulk value on plane 4 before increasing again to plane 6 and then falling monotonically towards the bulk value as observed for the continuum model. The observed behaviour is substantially different from what one would expect from the Madelung energies of the cation vacancies given in table 5.2. The maximum in the Madelung energy is on plane 1 which corresponds to the maximum vacancy energy. However the minimum in the Madelung energy is on the uppermost plane (plane 0) which although more stable than the vacancy on plane 1 is not the most stable vacancy overall. Examining the overall trend in the energies we can see that the continuum model breaks down in the near surface region. This is to be expected as the vacancies in this region will be within or very close to the region of the surface that has deviated most from the bulk structure on relaxation. We can suggest from these results that there will be a reduced concentration of cation vacancies at the basal surface of $\alpha Fe_2O_3$ compared to the subsurface region where a minimum in the vacancy formation energy is observed. We would expect the existence of this sub-surface minima to have a major effect on cation vacancy distribution near the basal surface when compared to the bulk concentration.

The anion vacancies, in contrast to the cation vacancies, exhibit a maximum at the uppermost plane, figure 5.13. Again we see a minimum in the formation energy in the subsurface region, but in this case the minimum in the vacancy

energy corresponds to the minimum in Madelung energy on plane 2, table 5.3. With the exception of this minimum, the overall trend follows the continuum model closely. Again from these values would we expect an enhanced oxygen vacancy concentration in the sub-surface layer when compared with the bulk.

Figures 5.14 and 5.15 show the relaxed vacancy formation energies near the $\{01\bar{1}2\}$ surface given in tables 5.4 and 5.5. The cation vacancies in figure 5.14 show a similar affect as observed for the basal plane in figure 5.12. The variation on the vacancy energies is quite complex in the near surface region but then follows the continuum model in a gentle approach to the bulk value. In the case of the $\{01\bar{1}2\}$ surface we see a maximum in the vacancy energy occurs on the third plane but no overall minimum. A local minimum in the vacancy energy is seen on plane 2 which also shows the minimum Madelung energy. This energy, however, is still 21 $kJmol^{-1}$ above the bulk value. These results would suggest no enhancement of the cation vacancy concentration near the $\{01\bar{1}2\}$ surface.

In contrast the anion vacancy formation energies shown in figure 5.15 do show a minimum below the bulk value on the uppermost plane. The minimum is 99 $kJmol^{-1}$ below the bulk value with the remaining values all being above the bulk value. An overall maximum occurs on plane 3 with an energy 76 $kJmol^{-1}$ less stable than in the bulk. Beyond this plane the energies decrease, approaching the value in the bulk. This would suggest an enhanced concentration of the oxygen vacancies at the surface of the $\{01\bar{1}2\}$ plane and indeed LEED experiments on the $\{01\bar{1}2\}$ surface are strongly dependent on oxygen partial pressure [148]. Also a (1 x 2) reconstruction of the $\{01\bar{1}2\}$ surface was observed and attributed to ordering of oxygen vacancies along the oxygen rows at this surface.

Comparing these results with the calculations of Lawrence et al [149] on the basal and $\{01\bar{1}2\}$ surfaces of chromia using a set of non-empirical potentials we see good agreement. The overall trends are similar but we note that Lawrence et al observed actual vacancy migration to the energy minima in the near surface region.

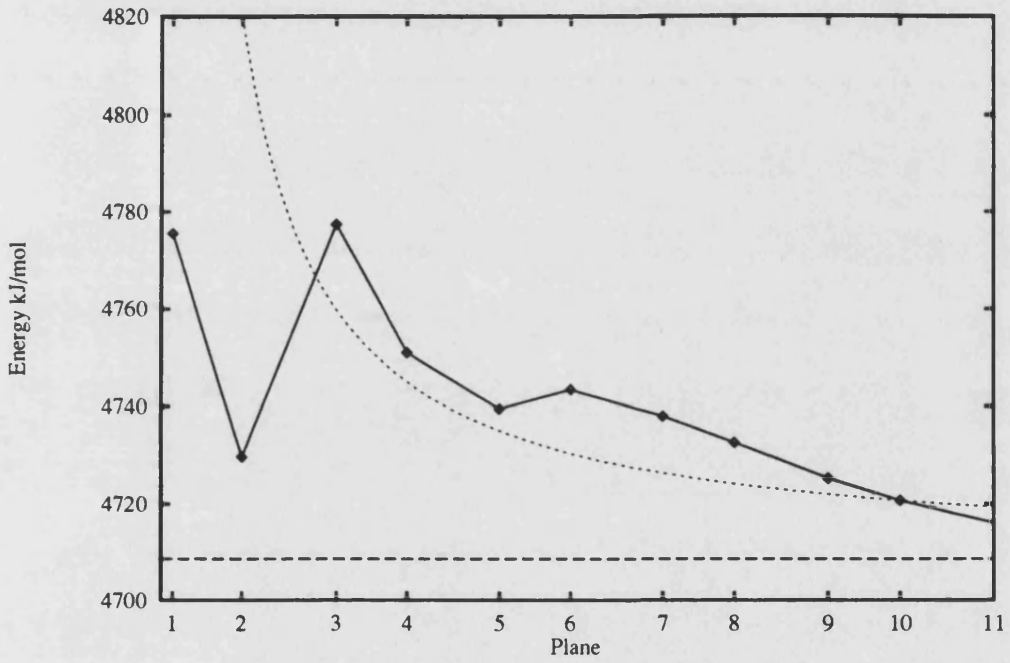


Figure 5.14: Plot of the cation vacancy energies as a function of distance from the $\{01\bar{1}2\}$ surface. Horizontal dashed line - bulk energy. Dotted line - continuum approximation.

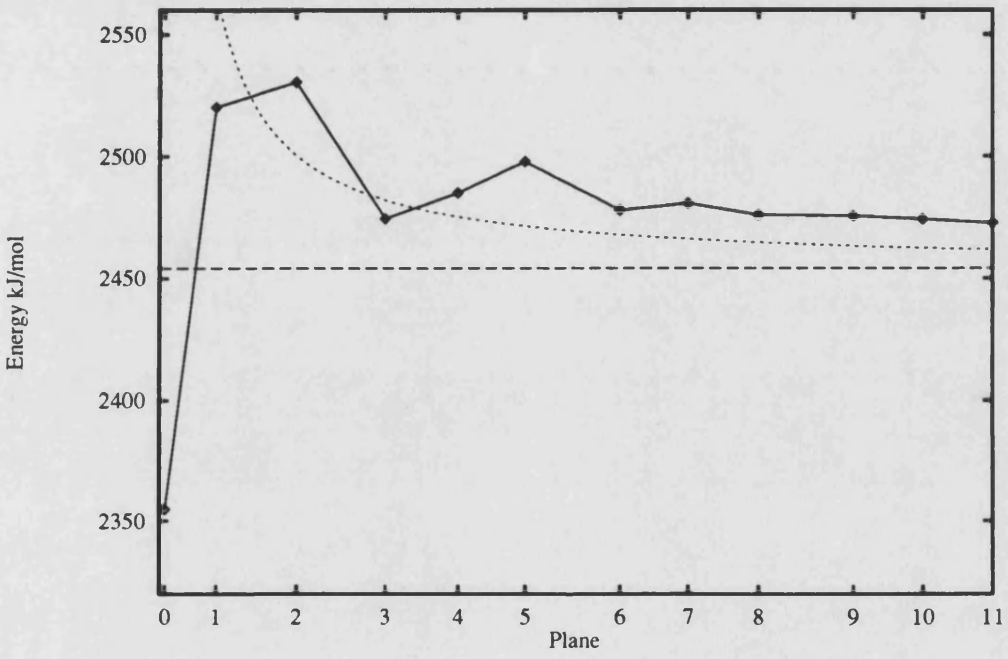


Figure 5.15: Plot of the anion vacancy energies as a function of distance from the $\{01\bar{1}2\}$ surface. Horizontal dashed line - bulk energy. Dotted line - continuum approximation.

## 5.4 Isovalent impurity segregation

The influence of impurities on ceramic materials is of fundamental importance in determining their properties. For example impurities will affect sintering, densification and catalytic properties [150, 151, 152]. In this section we shall consider the segregation of impurities to the low index surfaces of hematite. We shall start by discussing the isotherms presently used to interpret segregation results.

### 5.4.1 Segregation Isotherms

Experimental heats or enthalpies of segregation are obtained from plots of the logarithm of surface impurity concentration (assumed to be in equilibrium with the bulk) against the reciprocal temperature [153]. These plots are often linear and it is commonly assumed that this is indicative of an Arrhenius or Langmuir type behaviour, where the surface atomic ratio $x_s$ is related to the bulk ratio $x_b$ by an expression of the form

$$x_s \propto x_b \exp(-\Delta h/k_b T) \tag{5.1}$$

$\Delta h$ is the coverage independent heat of segregation, $k_b$ the Boltzmann constant, and $T$ is the temperature. Simple notions of steric hindrance, however, suggest that coverage-independent heats of segregation are a crude approximation other than at low coverages. Recent atomistic calculations [154, 155, 156] have confirmed that they are likely to be the exception rather than the rule. Consequently we shall present here a simple statistical mechanical model for segregation as derived by Mackrodt and Tasker [30] which allows for the variation of $\Delta h$ with surface coverage. This model assumes monolayer segregation; that is all segregated ions move to a single layer at the surface. Hence a direct relationship between the surface coverage and surface atomic ratio $x_s$ can be made.

The total free energy , $G$, for a two component system consisting of bulk and surface sites, each of one type only, can be written as

$$G = n_1^b g_1^b + n_1^s g_1^s + n_2^b g_2^b + n_2^s g_2^s - k_b T \ln \Omega \tag{5.2}$$

where $n_i^b$ and $n_i^s$ are the number of bulk and surface ions/atoms of type $i$ with individual free energies $g_i^b$ and $g_i^s$ respectively. Assuming a random distribution of ions the configurational entropy, $k_b \ln \Omega$, is given by

$$k_b \ln \Omega = \frac{N^b!}{n_1^b! n_2^b!} \frac{N^s!}{n_1^s! n_2^s!} \tag{5.3}$$

where $N_b$ and $N_s$ are the total number of bulk and surface sites. Due to the thermodynamic nature of this model we have to conserve the number of particles, hence

$$\begin{aligned} n_1^b + n_1^s &= n_1 \\ n_2^b + n_2^s &= n_2 \\ n_1^b + n_2^b &= N_b \\ n_1^s + n_2^s &= N_s \end{aligned} \tag{5.4}$$

Now if we use the convention that the atom/ion type 1 represents the impurity, then in addition to the constraints above we have

$$\begin{aligned} n_1 &<< n_2 \\ N^s &<< N^b \\ n_2^b &\approx N^b \end{aligned} \tag{5.5}$$

$G$ can now be rewritten as

$$G = G_1 + G_2 \tag{5.6}$$

with

$$\begin{aligned} G_1 &= n_1^s(g_1^s - g_2^s - g_1^b + g_2^b) + n_1 g_1^b + N^s g_2^s (n_2 - N^s) g_2^b \\ G_2 &= -k_b T \ln \Omega \end{aligned} \tag{5.7}$$

Differentiating with respect to $n_1^s$ and applying the constraint that the free energy does not change with the number of surface impurity ions/atoms gives

$$g_1^s - g_2^s - g_1^b + g_2^b + k_b T \ln(x_s/x_b) = 0 \tag{5.8}$$

where

$$x_s = \frac{n_1^s}{n_2^s}$$
$$x_b = \frac{n_1^b}{n_2^b} \tag{5.9}$$

Now writing

$$g_1^s - g_2^s = \delta g^s$$
$$g_1^b - g_2^b = \delta g^b \tag{5.10}$$
$$\delta g^s - \delta g^b = \Delta g$$

we get

$$x_s = x_b \exp(-\Delta g / k_b T) \tag{5.11}$$

which is similar to the Arrhenius like relationship quoted earlier.

To obtain a modified expression to allow change in heat of segregation with surface coverage we rewrite $G_1$ as

$$G_1 = n_1^s \Delta g + n_1 g_1^b + n_2 g_2^b + N^s(g_2^s - g_2^b) \tag{5.12}$$

in which $N^s(g_2^s - g_2^b)$ can be identified as the surface free energy of the host lattice. Differentiating $G_1$ with respect to $n_1^s$, allowing variation in $\Delta g$ with surface concentration, gives

$$\frac{dG_1}{dn_1^s} = \Delta g + n_1^s \frac{d\Delta g}{dn_1^s} \tag{5.13}$$

and since

$$n_1^s \frac{d\Delta g}{dn_1^s} = x_s(x_s + 1)\frac{d\Delta g}{dx_s} \tag{5.14}$$

the modified expression for $x_s$ is

$$x_s = x_b \exp[-(\Delta g + x_s(x_s + 1)\frac{d\Delta g}{dx_s})/k_b T] \tag{5.15}$$

If we write $\Delta g$ in terms of the heat of segregation $\Delta h$, and $\Delta s$ the vibrational entropy of segregation the final form of the isotherm is

$$x_s = x_b \exp[-(\Delta h + x_s(x_s + 1)\frac{d\Delta h}{dx_s})/k_b T] \exp[(\Delta s + x_s(x_s + 1)\frac{d\Delta s}{dx_s})/k_b] \tag{5.16}$$

from which the slope of $\ln(x_s)$ against $1/T$ is not $\Delta h$ as it is for an Arrhenius-Langmuir expression. It is important to note that $x_s$ in the equation above is the ratio of impurity/host ions at the surface and not a concentration. This is an inconvenient definition because monolayer coverage in undefined. This problem is overcome by writing equation (5.15) as

$$\frac{n_1^s}{n_2^s} = \frac{n_1^b}{n_2^b} \exp[(\Delta g + n_1^s \frac{d\Delta g}{dx_s})/k_b T] \tag{5.17}$$

and defining a surface and bulk concentration $C_s$ and $C_b$ such that

$$C_s = \frac{n_1^s}{(n_1^s + n_2^s)} \tag{5.18}$$

$$C_b = \frac{n_1^b}{(n_1^b + n_2^b)} = \frac{n_1^b}{n_2^b} \tag{5.19}$$

Substituting (5.18) and (5.19) into (5.17) the surface impurity concentration is given by

$$C_s = \frac{C_b \exp[(\Delta g + C_s \frac{d\Delta g}{dC_s})/k_b T]}{1 + C_b \exp[(\Delta g + C_s \frac{d\Delta g}{dC_s})/k_b T]} \tag{5.20}$$

and monolayer coverage corresponds to $C_s = 1$. Equation (5.20) is identical to that proposed by McLean [157], except that here $\Delta g$ is not independent of surface coverage. As above the surface coverage can be written in terms of the enthalpy and entropy of segregation thus

$$C_s = \frac{C_b \exp(-\Gamma/k_b T)}{1 + C_b \exp(-\Gamma/k_b T)} \tag{5.21}$$

where

$$\Gamma = (\Delta h + C_s \frac{d\Delta h}{dC_s}) - T(\Delta s + C_s \frac{d\Delta s}{dC_s}) \tag{5.22}$$

Again this form of the isotherm does not necessarily exhibit Langmuir behaviour. However, experimental plots of log surface concentration versus reciprocal tem-

perature are often linear. This can be interpreted by writing (5.21) as

$$\begin{aligned} \ln(C_s) &= \ln(C_b) + (\Delta s + C_s\frac{d\Delta s}{dC_s}) - (\Delta h + C_s\frac{d\Delta h}{dC_s}) \\ &= \chi - H/K_bT \end{aligned} \tag{5.23}$$

and solving for $H$ such that

$$H = \Delta h(C_s) + C_s\frac{d\Delta h}{dC_s} \tag{5.24}$$

The trivial solution is where $\Delta h$ is independent of $C_s$. H is also independent of the surface concentration when $\Delta h \propto -C_s^{-1}$.

The important result of this formulation is that there are two possible definitions of segregation. Both are atomistic definitions in that they physically represent the difference in the internal energy of an impurity at the surface and bulk, but for one we have defined the amount of impurity as the surface as an atomic ratio relative to the host surface cations, whilst in the other we have defined it as a concentration. The linear relationship between $\ln(C_s)$ and $1/T$ has been shown to be a special solution of the derived isotherm.

### 5.4.2 Results

The heats of segregation of $Al^{3+}$, $Cr^{3+}$ and $Y^{3+}$ at infinite dilution and coverages of a 1/4, 1/2, 3/4 and 1 were calculated using MIDAS for each of the five low index surfaces of hematite. For each surface where multiple arrangements of the impurities were allowed, the energies given here correspond to the most stable arrangement. According to the Mclean model of segregation [157] the primary driving force for isovalent impurity segregation is the elastic strain induced in the bulk lattice by the impurity. This is related to the difference in the size of the impurity and host cation, $\Delta r$, by the expression [158]

$$U_{elastic} = \frac{6\pi r^3(\frac{\Delta r}{r})^2 B}{1 + 3B/4\mu}$$

| Impurity Cation | $\Delta r/r$ | $U_{elastic}$ (J) |
|---|---|---|
| $Al^{3+}$ | -0.20 | $4.421 \times 10^{-21}$ |
| $Cr^{3+}$ | -0.02 | $3.215 \times 10^{-23}$ |
| $Y^{3+}$ | 0.40 | $1.296 \times 10^{-20}$ |

Table 5.6: Magnitude of elastic strain induced in hematite by isovalent impurities.

where $r$ is the radius of the host lattice, $B$ is the bulk modulus of the impurity and $\mu$ is the shear modulus of the host lattice. According to this expression all impurities should segregate, the elastic strain being reduced by a move to the surface, the driving force segregation being related to the ion size mismatch. The value for $\Delta r/r$ and $U_{elastic}$ for the three cation in hematite are given in table 5.6. From this table we can see that using this simple model we would predict the driving force for segregation is largest for $Y^{3+}$ and least for $Cr^{3+}$. Previous calculations on segregation of a series of divalent cations to the surfaces of MgO [154] have shown that such arguments give a good guide to the relative heats of segregation for such compounds.

The calculated heats of segregation to the basal {0001} surface of hematite are plotted as a function of surface coverage in figure 5.16. We can see that for both $Al^{3+}$ and $Y^{3+}$ the segregation energies are effectively constant with coverage, the changes being less than 5 $kJmol^{-1}$ between zero and full coverage for both ions. This reflects the large separation of surface cations, steric hindrance having no effect at this surface. The size mismatch relationship discussed above is reflected in the relative segregation energies of these two cations, the $Y^{3+}$ segregation energy being twice that of the $Al^{3+}$ cation. The impurity cation mismatch is also reflected in the relaxed structure of the basal surface containing either of these two cations. As we discussed earlier the cations at the basal surface relax into the surface. For $Al^{3+}$, the smaller cation, we find that the impurity relaxed further than the host cation into the surfaces, whereas $Y^{3+}$ remains above the surface anions. This steric effect is also reflected in the preferred orientation of impurities at half coverage.

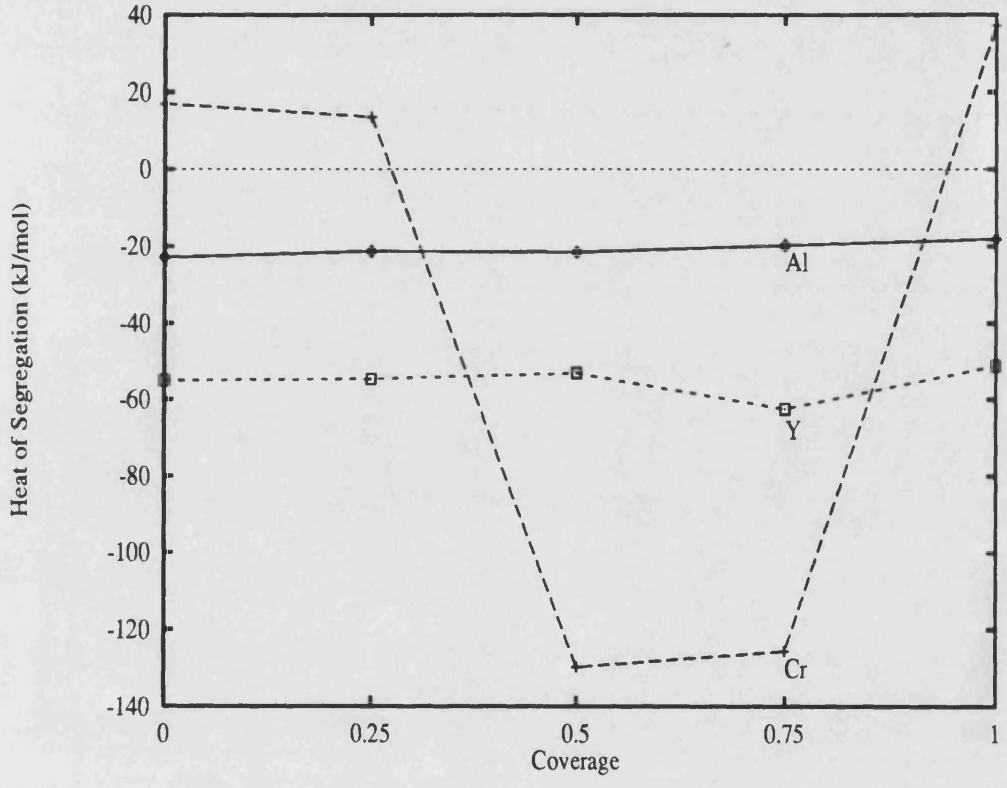


Figure 5.16: Calculated heat of segregation as a function of coverage at the {0001} surface.

For $Al^{3+}$ the most stable arrangement has the impurities along the diagonal, see figure 5.7, whereas for the large $Y^{3+}$ cation the preferred arrangement is along the cation rows where the cation-cation separation is maximised.

The most interesting feature of figure 5.16 is the variation of the heat of segregation for chromium. At low coverage of a quarter or below and at full coverage the heat of segregation is positive where as at half and three quarters coverage it is very negative. Based on the ion size arguments we would expect the energy to be less than that of $Y^{3+}$ and $Al^{3+}$, this is the case at low and full coverage but not over the whole range of coverages. This discrepancy between the simple model based on elastic strain above can be attributed to the effects of surface relaxation. Before relaxation the heat segregation for $Cr^{3+}$ is constant with coverage. The extra stability of the half and three quarters coverage is due to extra relaxation of the anions between the impurity cations. This will only occur when the $Cr^{3+}$ cations are close together as which is not the case at quarter coverage, and when there is some asymmetry in the cation arrangement which cannot occur at full coverage. In fact at full coverage the relaxed structure is almost identical to that for pure hematite with the $Cr^{3+}$ impurity cation relaxing to the same position as $Fe^{3+}$ cation in pure compound.

Figure 5.17 gives the calculated heats of segregation for the $\{10\bar{1}0\}$ surface. As with the basal surface we see that the $Y^{3+}$ segregation energy is more negative than for $Al^{3+}$ but less than for $Cr^{3+}$ which shows a large variation in its heat of segregation. The variation in the $Al^{3+}$ and $Y^{3+}$ heats of segregation is easily explained if the relaxed $\{10\bar{1}0\}$ surface structure described earlier is considered. For the $\{10\bar{1}0\}$ surface the top layer containing cations has four cation sites. On relaxation these split into two pairs, one pair relaxing slightly nearer to the surface. The preferred substitution site at the surface for $Al^{3+}$ is at a cation site that relaxed further into the surface, whereas $Y^{3+}$ prefers to substitute in the other site which moves closer to the surface. Above half coverage, however, the impurity must occupy some of the less favoured sites and the heat of segregation

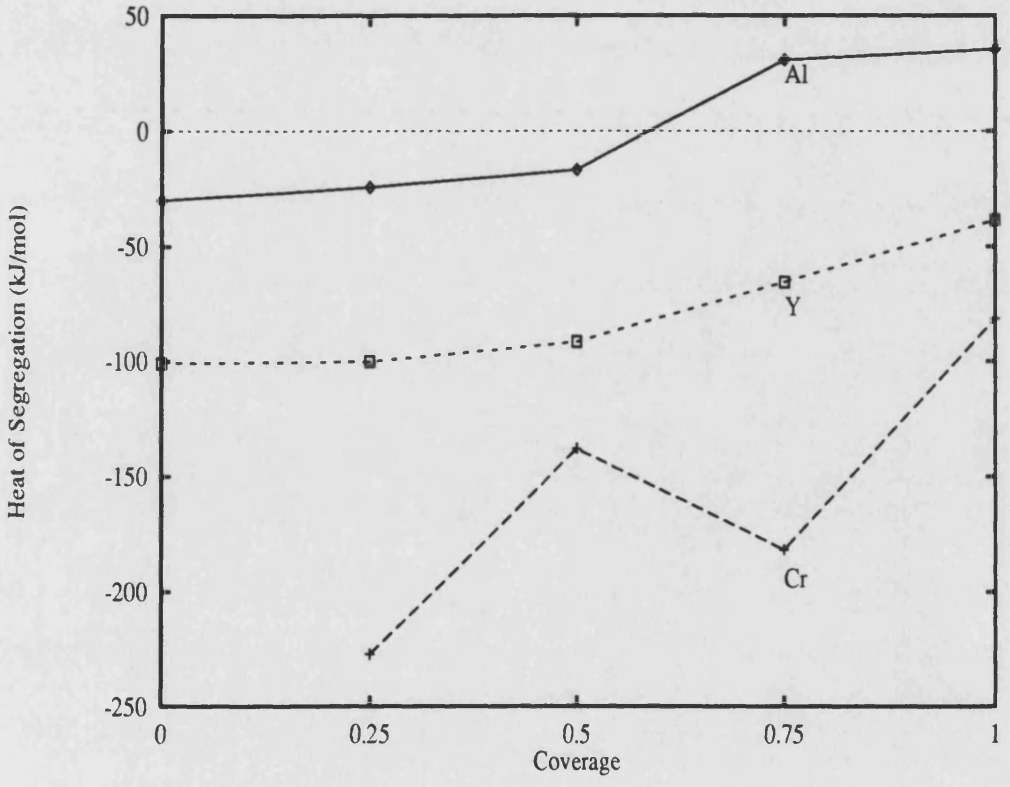


Figure 5.17: Calculated enthalpy of segregation as a function of coverage at the $\{10\bar{1}0\}$ surface.

becomes more positive as can be seen in figure 5.17. If there was a single type of surface cation site, the heats of segregation for these two cations would be almost constant with coverage. The variation of the heat of segregation with coverage for $Cr^{3+}$ is again much more complicated than for the other two cations. We observe minima at a quarter and three quarters coverage (the zero coverage calculation did not provide a minimised energy). These may be attributed to the presence of a three to one mix of the different cations at these coverages, when relaxing in both case the single cation of $Cr^{3+}$ at quarter coverage or the single $Fe^{3+}$ cation at three quarters coverage relax to a much greater degree towards the surface than the other surface cations. The similarity of the effect at the quarter and three quarters coverage may be due to the similarity of the impurity and host cation size, the difference being only 0.1Å[159]. This similarity is in ion size may also be responsible for the failure of the model based on elastic strain at this surface. The model predicts the correct order for the $Al^{3+}$ and $Y^{3+}$ heats of segregation, as it does at all surfaces considered. However, the prediction that $Cr^{3+}$ should have the smallest heat of segregation is certainly untrue for the $\{10\bar{1}0\}$ and all the remaining surfaces considered.

Comparing the results for the $\{10\bar{1}0\}$ and the other prism plane the $\{11\bar{2}0\}$ given in figure 5.18 we again see some coverage dependence for all three cations. For the $\{11\bar{2}0\}$ however, the $Al^{3+}$ cation differs from the other two cations. Both the $Cr^{3+}$ and $Y^{3+}$ impurities give a minimum in the heats of segregation. For $Y^{3+}$ this is at about quarter coverage and for $Cr^{3+}$ it is at about two thirds coverage. The variations are larger than in the case of the $\{10\bar{1}0\}$ surface. This maybe due to the smaller area of the surface unit cell for the $\{11\bar{2}0\}$ direction increasing the cation density, as it's area is about half that of the other prism plane. The minima in the $Y^{3+}$ results can be attributed to steric hindrance, the large cations interfering with each other as the coverage increases. The almost identical value for full coverage of $Y^{3+}$ or $Cr^{3+}$ has no obvious explanation, the relaxed structures being considerably different. The $Al^{3+}$ results bear some examination, we have

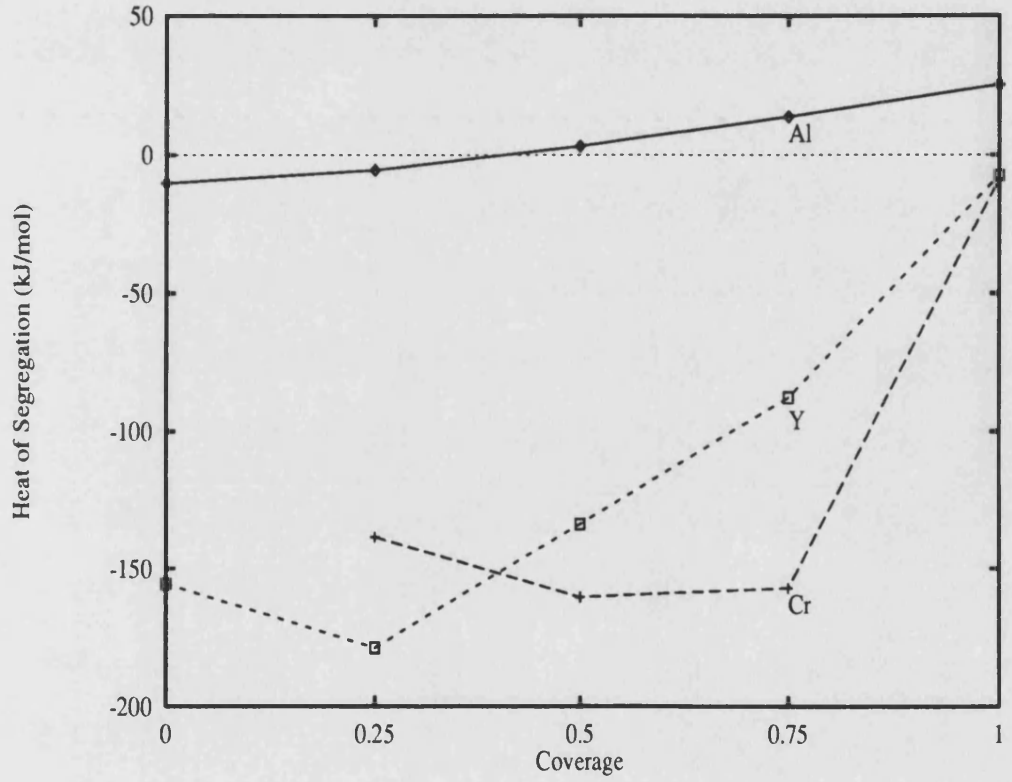


Figure 5.18: Calculated enthalpy of segregation as a function of coverage at the $\{11\bar{2}0\}$ surface.

a steady positive increase in the heat of segregation with coverage whereas for the $\{10\bar{1}0\}$ we had a jump in the energy above half coverage. Again this can be attributed to the higher cation density at the $\{11\bar{2}0\}$ surface. As with the $\{10\bar{1}0\}$ surface the four surface cations at the the $\{11\bar{2}0\}$ split into two pairs on surface relaxation. The $Al^{3+}$ impurity prefers the two sites that relax furthest into the surface, and therefore above half coverage we would expect a discontinuity in energy as we calculated for the $\{10\bar{1}0\}$ surface. However, because of the higher cation density at the $\{11\bar{2}0\}$ surface, interactions between the impurity cations will have a larger effect than for the other prism plane. The variation of the heat of segregation of $Al^{3+}$ is therefore a combination of steric effects and the occupancy of the two types of cation site. The same combination of effects will apply for $Y^{3+}$ but due to the large size of this ion the steric effects dominate.

In figure 5.19 we see the calculated heat of segregation for the $\{01\bar{1}2\}$ surface of hematite. This is the only surface to show a relatively constant heat of segregation for $Cr^{3+}$. All three cations at this surface show minima at approximately a quarter coverage, the size of the minima reflecting the ion size mismatch. $Y^{3+}$ shows a very distinct minima reflecting the steric effects caused by this large ion. The $Al^{3+}$ minima is more shallow but easily discernible, again this can be attributed to steric effects. The $Cr^{3+}$ minima, however, is very shallow, the heat of segregation varying by only 5 $kJmol^{-1}$ across the whole range of coverages. At this surface, therefore, we can conclude that the only effect on the heat of segregation due to coverage is due to steric effects, while relaxation effects make little or no contribution. This follows from the small amount of relaxation that takes place at this surface as shown by the small change in the surface energy given earlier in table 5.1.

Finally, in figure 5.20 we give the calculated heats of segregation as a function of coverage for the $\{10\bar{1}1\}$ surface. We can see that again we predict the $Cr^{3+}$ cation to have the most negative heat of segregation. In the case of the $\{10\bar{1}1\}$ surface we have the most exothermic heat of segregation for all the surface considered, the next most exothermic being $Cr^{3+}$ on the $\{10\bar{1}0\}$ surface which is

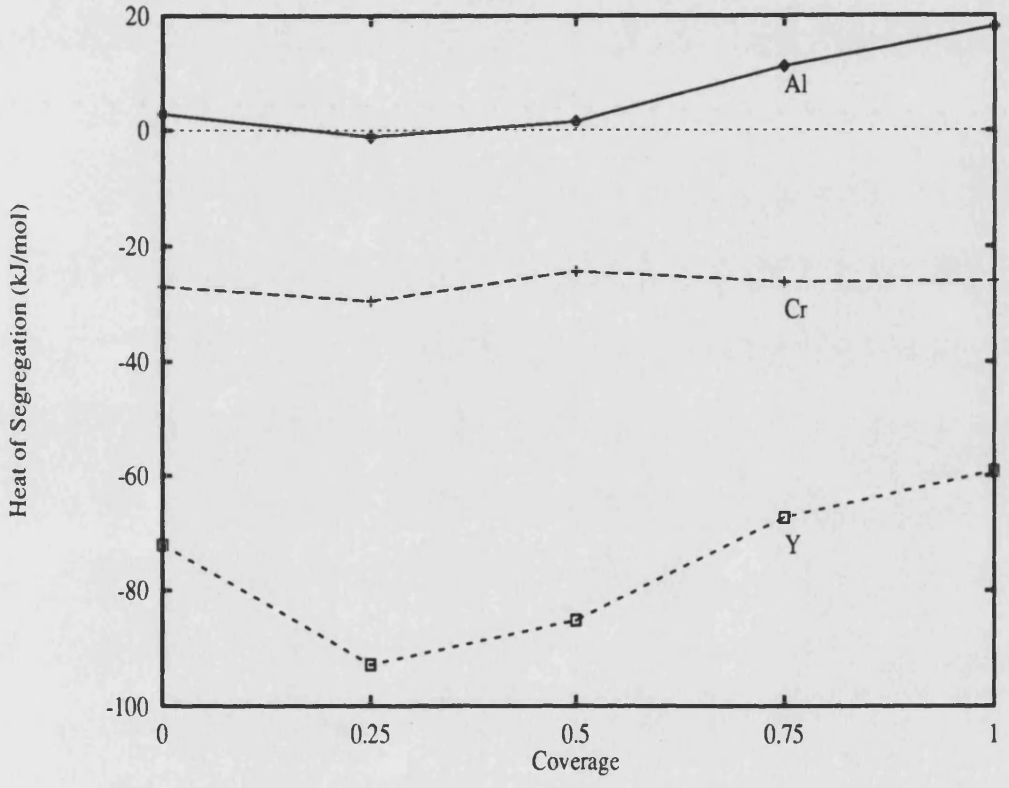


Figure 5.19: Calculated enthalpy of segregation as a function of coverage at the $\{01\bar{1}2\}$ surface.

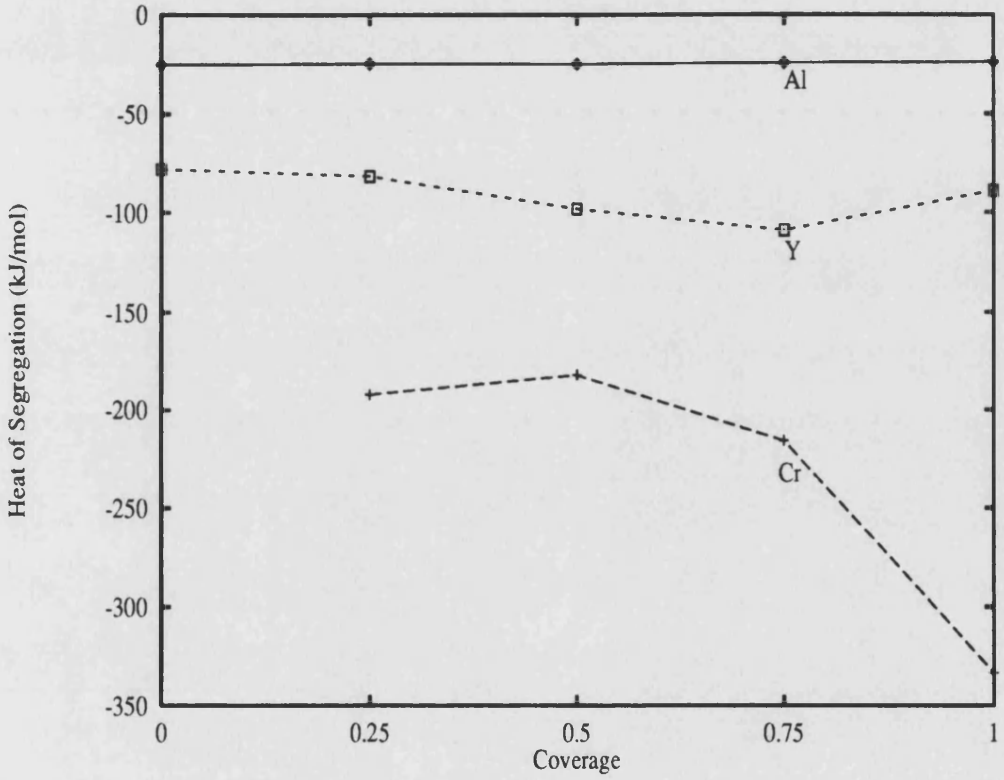


Figure 5.20: Calculated enthalpy of segregation as a function of coverage at the $\{10\bar{1}1\}$ surface.

approximately 100 $kJmol^{-1}$ less than the value shown in figure 5.20. This extra stability may be the result of the extra scope for relaxation at this surface. The perfect surface is predicted to be the least stable of the five low index faces therefore stabilisation by the impurities has a greater impact. Again as with the basal surface we see very little effect on $Al^{3+}$ heat of segregation with coverage. This can be attributed to the small size of this ion and the open structure of this surface. Steric effects still play some part in the $Y^{3+}$ segregation energy with a minima appearing at three quarters coverage.

Overall from this set of quite complex results some general trends can be observed. $Al^{3+}$ normally has a positive or slightly negative heat of segregation, for surfaces which undergo large amounts of relaxation a negative heat of segregation of approximately -20 $kJmol^{-1}$ is observed. However we note that even for such a small cation some steric effects apply, especially in the case of the $\{10\bar{1}0\}$ where the surface cation are split into two types. Overall we can say that $Al^{3+}$ is the cation least likely to segregate. $Y^{3+}$ shows negative heats of segregation for all surfaces ranging between -50 $kJmol^{-1}$ to -175 $kJmol^{-1}$. For this large cation steric effects are observed on all surfaces, the variation of the segregation energy being largest for surfaces where the cation density is large. Overall we would expect some segregation of $Y^{3+}$ to all surfaces, the coverage being surface dependent. The $Cr^{3+}$ results show the most complex behaviour. For most surfaces we see a minima and in some case multiple minima. In all cases however we have negative heats of segregation at most coverages. The complex nature of the $Cr^{3+}$ results may be attributed to the similarity of the ion sizes of the $Cr^{3+}$ and $Fe^{3+}$ cations. The minima may be due to the formation of ordered secondary phases.

There is no experimental data available for the impurity segregation to the surface of hematite. Therefore we shall compare our results to previous calculations and some experimental results for isovalent impurity segregation to the surfaces of polycrystalline alumina. Mackrodt [155] has calculated the heats of segregation for $Fe^{3+}$, $Y^{3+}$ and $La^{3+}$ to the low index surfaces of alumina, $\alpha Al_2O_3$.

He found large variations in the heat of segregation with coverage for all surfaces with energy minima present at several surfaces. The trend in the heats in segregation with ion size mismatch following the order predicted by Mclean's model based on elastic strain. These results show similar features to those presented here, but for the basal and the $\{01\bar{1}2\}$ surfaces we found that some ions showed almost a constant heat of segregation whereas Mackrodt found large variations. This difference is due to the fact that for the three cations considered at the alumina surfaces the ion size mismatches are all large and therefore steric effects will have more impact than the relatively small mismatches in the cation sizes consider here. Lawrence [132] also found constant heats of segregation with coverage for $Al^{3+}$, $Y^{3+}$and $La^{3+}$ at the basal plane of chromia, $\alpha Al_2O_3$. The Lawrence results, however, differ from our calculations in that he found the heat of segregation of $Al^{3+}$ to be much more negative than that for $Y^{3+}$ at all of the low index surfaces of chromia. Overall the results here show better agreement with the results of Mackrodt than those of Lawrence even thought we would consider chromia to be more similar to hematite than alumina.

Yttrium segregation to the surfaces of polycrystalline alumina has been examined experimentally by McCune et al, [160, 161]. They obtained a heats of segregation of -23 $kJmol^{-1}$ and -44 $kJmol^{-1}$ from straight line plots of surface atomic ratio versus reciprocal temperature. The two results reflect the different surface concentrations obtained at two different energies of an AES spectrum. These values do not compare well with the calculated heats of segregation given here, the calculated heats being near to 100 $kJmol^{-1}$. However we must remember that McCune assumes the straight lines are due to Langmuir behaviour, but we have shown that the heat of segregation does vary with coverage. Therefore in order to compare our results with experiment we must examine the relationship between the equilibrium surface coverage predicted by the calculated heats of segregation and temperature.

### 5.4.3 Equilibrium surface coverage

We can obtain the equilibrium coverage for each impurity and surface using the segregation isotherms described earlier in section 5.4.1 by solving the equation

$$C_s = \frac{1}{1 + C_b^{-1} \exp\left[(\Delta h + C_s \frac{d\Delta h}{dC_s})/k_b T\right]} \tag{5.25}$$

Here we use the enthalpy of segregation $\Delta h$ although to be strictly correct we would require the free energy of segregation $\Delta g$. However we have no way of evaluating the entropy of segregation $\Delta s$ so we assume it to be zero. Masri et al [162] have obtained a value of -0.24$k_b$ for the entropy of segregation for $Ca^{2+}$ to the {100} surface of MgO at half coverage, the contribution to the free energy for this entropy would be approximately 3 kJmol$^{-1}$ compared to a experimental heat of segregation of between -40 and -100 kJmol$^{-1}$. This assumption therefore has some justification.

In figures 5.21 to 5.23 we plot the calculated equilibrium coverages for each of the three cation impurities considered to some of the low index surfaces of $\alpha Fe_2O_3$ for a temperature range of 1000 to 1700 K and a bulk impurity concentration of 200 ppm. In figure 5.21 we see the equilibrium coverages for $Al^{3+}$ at the {0001}, {10$\bar{1}$0} and {10$\bar{1}$1} surfaces hematite. The remaining two surfaces, the {01$\bar{1}$2} and {11$\bar{2}$0}, have predominantly positive heats of segregation and therefore no segregation should take place. The small size heats of segregation for these three surfaces are reflected in the low coverages predicted; a ratio of 0.004 being equivalent to a surface coverage of 0.4 percent. These low coverages and their small range results in a linear variation with temperature as is normally observed experimentally. The variation of the heat of segregation with coverage having no effect and Langmuir behaviour can be assumed. From the slopes of these lines we can calculate the heat of segregation as would be observed experimentally. These are given in table 5.7, and because of the Langmuir behaviour exhibited by $Al^{3+}$, the energies taken from these graphs are identical to the calculated heats of segregation given earlier.

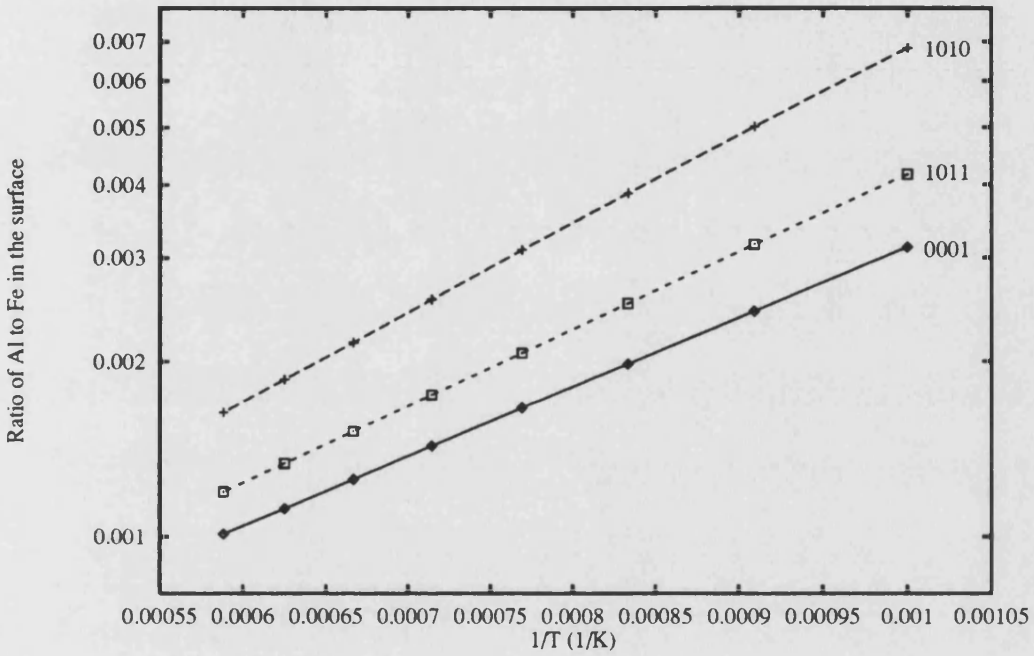


Figure 5.21: Calculated equilibrium coverage of $Al^{3+}$ at the surfaces of $\alpha Fe_2O_3$ as function of temperature for a bulk concentration of 200 ppm.

| Surface | $C_s$ at 1000 K | $C_s$ at 1700 K | $\Delta h$ (kJmol$^{-1}$) |
|---|---|---|---|
| {0001} | 0.0031 | 0.0010 | -22.82 |
| $\{10\bar{1}0\}$ | 0.0068 | 0.0016 | -28.88 |
| $\{10\bar{1}1\}$ | 0.0041 | 0.0012 | -25.23 |

Table 5.7: Calculated heat of segregation based on the predicted variation of $Al^{3+}$ coverage at the surfaces of hematite. Bulk concentration 200ppm.

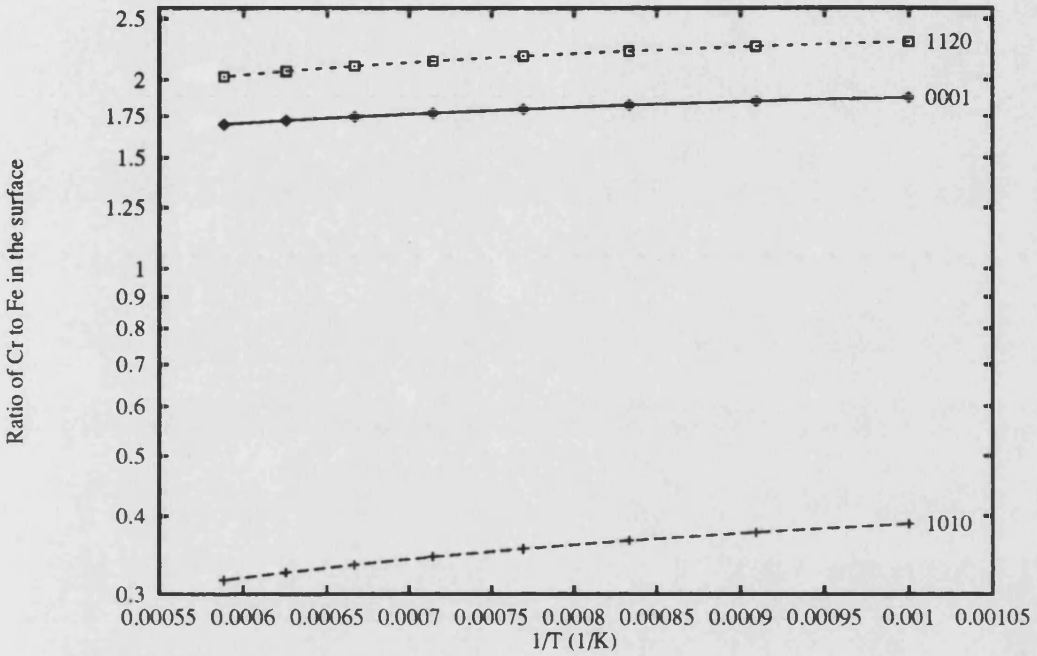


Figure 5.22: Calculated equilibrium coverage of $Cr^{3+}$ at the surfaces of $\alpha Fe_2O_3$ as function of temperature for a bulk concentration of 200 ppm.

| Surface | $C_s$ at 1000 K | $C_s$ at 1700 K | $\Delta h$ (kJmol$^{-1}$) |
|---|---|---|---|
| {0001} | 0.652 | 0.629 | -1.99 |
| $\{10\bar{1}0\}$ | 0.280 | 0.240 | -4.20 |
| $\{01\bar{1}2\}$ | 0.005 | 0.001 | -27.45 |
| $\{11\bar{2}0\}$ | 0.697 | 0.669 | -2.54 |

Table 5.8: Calculated heat of segregation based on the predicted variation of $Cr^{3+}$ coverage at the surfaces of hematite. Bulk concentration 200ppm.

In figure 5.22 we see the calculated variation of equilibrium coverage of $Cr^{3+}$. The $\{01\bar{1}2\}$ surface is not included because of the small value calculated. No variation was found for the $\{10\bar{1}1\}$ surface, the high heat of segregation resulting in 100 percent coverage for all temperatures. The equilibrium coverages shown in figure 5.22 reflect the minima in the heats of segregation seen earlier. For the $\{10\bar{1}0\}$ surface we see an equilibrium coverage of approximately 25 percent where as for the $\{0001\}$ and $\{11\bar{2}0\}$ we calculate value of approximately 64 and 68 percent respectively. The effect of minima are also reflected in the small variation of the coverage with temperature. These small variations lead to very small slopes and therefore small heats of segregation, table 5.8. The only surface predicting a heat of segregation comparable to the calculated heats given earlier is the $\{01\bar{1}2\}$ which showed a relatively small heat of segregation almost constant with coverage. These results would suggest that experimental measurements based on an assumption of Langmuir behaviour for the segregation of $Cr^{3+}$ to the surfaces of hematite would grossly underestimate the real heat of segregation. For example, the calculated heat of segregation for $Cr^{3+}$ at the $\{0001\}$ surface for a coverage of 0.64 given earlier is approximately -153 $kJmol^{-1}$ whereas that predicted from the slope of the coverage versus reciprocal temperature is only -2 $kJmol^{-1}$.

For $Y^{3+}$ the predicted equilibrium coverages show much larger variations both with surface and temperature, figure 5.23. This is due to the large heats of segregation calculated and the lack of shape minima in the coverage dependence of those heats. The plots in figure 5.23 could be consider linear if a smaller temperature range were used. The heats of segregation obtained from these graphs and the variation in coverage for the other two surfaces are given in table 5.9. Here we see a range of energies from -56 $kJmol^{-1}$ to -6 $kJmol^{-1}$ but again as with $Cr^{3+}$ these energies are far below the corresponding calculated heats given earlier (except in the case of basal surface where we would expect true Langmuir behaviour). The worst case is that for the $\{11\bar{2}0\}$ surface where a large minima is observed in the heat of segregation at quarter coverage. This range of value

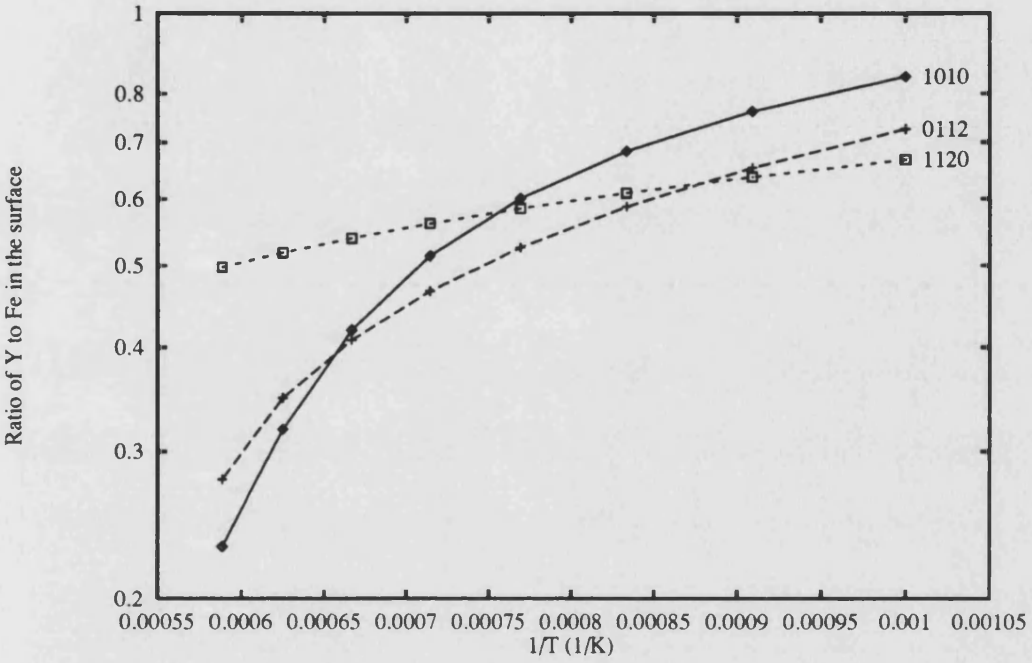


Figure 5.23: Calculated equilibrium coverage of $Y^{3+}$ at the surfaces of $\alpha Fe_2O_3$ as function of temperature for a bulk concentration of 200 ppm.

| Surface | $C_s$ at 1000 K | $C_s$ at 1700 K | $\Delta h$ (kJmol$^{-1}$) |
|---|---|---|---|
| {0001} | 0.135 | 0.010 | -55.93 |
| $\{10\bar{1}0\}$ | 0.456 | 0.188 | -24.29 |
| $\{10\bar{1}1\}$ | 0.773 | 0.665 | -10.62 |
| $\{01\bar{1}2\}$ | 0.421 | 0.217 | -18.20 |
| $\{11\bar{2}0\}$ | 0.400 | 0.332 | -5.88 |

Table 5.9: Calculated heat of segregation based on the predicted variation of $Y^{3+}$ coverage at the surfaces of hematite. Bulk concentration 200ppm.

covers the experimental values of -44 or -23 kJmol$^{-1}$ obtained by McCune et al for polycrystalline alumina. However, this apparent agreement with experiment, all be it with a different compound, may not reflect that we have correctly modelled either the heats of segregation or their variation with coverage at each surface. The calculated equilibrium coverages and their variation are dependent on a subtle mix of the heats of segregation and their variations. Therefore we can imagine there to be many possible scenarios which could result in a good match with the experimental heats of segregation. Direct comparison between the expermental and predicted coverages could help to identify possible errors in our calculations, however, such comparisons are impossible due to some lack of specificity in the experiments. The coverages detected by McCune et al at approximately 16 percent are much lower than we predict for all except the basal surface, this however may reflect the fact that experimental methods sample a finite depth of crystal whereas our calculated coverages are for the top cation layer alone.

### 5.5 Summary

In this chapter we have presented calculations dealing with the perfect and defective surfaces of hematite. As in the previous chapter we found for the perfect surfaces that relaxation effects were important. The relative order of stability of the surfaces change on relaxation. This had a large effect on the predicted equilibrium morphology. Again as discovered in the previous chapter, the morphology based on the relaxed surface energies showed good agreement with real crystals.

The importance of the surface relaxation effects was also seen in the vacancy formation energies at the {0001} and {01$\bar{1}$2} surfaces of hematite. The relaxation at both surfaces generated a dipole perpendicular to the surface. This dipole effects the vacancy formation energies by shifting the Madelung potential. Comparison of the bulk and surface vacancy energies therefore required this shift to be taken into account. Taking this shift and the image charge interaction into account we found that in all but the case of the cation vacancies near the {01$\bar{1}$2}

surface the vacancies were stabilised with respect to the bulk. For the basal surface we found minima in the vacancy energies in the subsurface region. For the anion vacancies at the $\{01\bar{1}2\}$ surface we found a minima at the surface. This was proposed as an explanation for problems observed in LEED studies of this surface.

Segregation energies for $Al^{3+}$, $Y^{3+}$ and $Cr^{3+}$ for all of the low index surfaces were calculated. We observed that the segregation energies for all three impurities varied with coverage. Simple arguments based on elastic strain correctly predicted the relative heats of segregation for $Y^{3+}$ and $Al^{3+}$, however, this model broke down for $Cr^{3+}$. Minima were observed for $Cr^{3+}$ on the majority of surfaces, these may be due to the formation of ordered phases. Equilibrium coverages calculated from our heats of segregation gave plots versus reciprocal temperature which were linear, a feature normally associated with Langmuir type behaviour. Heat of segregation obtained from these plots gave energies well below that calculated directly. In the case of $Y^{3+}$ we found that these energies gave good agreement with those obtained experimentally for polycrystalline alumina. This apparent agreement, however, may be fortuitous.

# Chapter 6

## Grain boundaries in hematite

In ceramic materials the boundaries between grains have are large and often controlling effect on many properties and processes, such as fracture strength, toughness, plastic deformation, conductivity, creep, corrosion and sintering [163]. Therefore a knowledge of their structure is of great interest to ceramic scientists. However the vast majority of theoretical work carried out to date has centered around metallic systems [164, 165] where calculations have been utilised in determining a large number of grain boundary structures. Previous calculation on oxide boundaries have in the main been limited to boundaries in rocksalt structured oxides [33, 166].

In this chapter we shall consider grain boundaries in hematite, more specifically we shall consider the highly symmetric twin boundaries. After determining the most stable structure for each low index twin we shall go on to consider vacancy formation and impurity segregation at these boundaries following the work on the surfaces of hematite in the previous chapter. We shall start however, with a brief outline of the models used to describe grain boundaries.

### 6.1 Grain boundary models

A grain boundary is the interface between two crystalline grains with different orientations. Nine parameters are required for a complete macroscopic description of for any particular interface: three to describe the misorientation, two for the boundary inclination, three for the relative translation and a ninth to locate the boundary plane which may pass through non-equivalent planes when basis atom/ions are present. Such a description does not, however, provide any information about the detailed atomic/ionic configuration of the boundary or the relationship between the misorientation angle and properties such as the interfacial energy. Consequently three models have been proposed to provide additional

information about the boundaries and their properties [167]. We shall give brief summaries of these models here.

One of the earliest models of grain boundary structure formulated is the dislocation model which describes low-angle boundaries as a regular network of lattice dislocations [168, 169]. Using this model expressions for the variation in the boundary energy with orientation and the stress factor have been derived by Read [170]. This model has been used successfully in describing the variation of a large number of interfacial properties with misorientation angle, although its success is limited to the low angle regime where the atom/ion cores of the boundary are resolvable. Even in this low angle regime, however, it has been shown that this model may not always be unambiguous.

The coincident sites lattice model is based on imagining the two neighbouring lattices continuing across the interface. The points that are then common to both lattices form the coincident site lattice (CSL). The inverse of the ratio of coincident sites to lattice sites is expressed as a $\Sigma$ value for the boundary. Coincident boundaries are always periodic in the boundary plane but the unit cell may be large. Certain low $\Sigma$ (high coincidence) boundaries have particularly low interfacial energy and diffusivites and these are often referred to as "special" boundaries. The reason for the special properties of the high coincidence boundaries was originally thought to be due to the good crystallographic fit between the two crystals around the coincidence sites. However, it has been demonstrated using imaging techniques [171] and computer simulation [172] that the lowest energy structures are generally displaced from the coincidence configuration. Not all low $\Sigma$ boundaries exhibit these properties and the interfacial energy does not appear to be correlated with the value of $\Sigma$ [173]. Therefore this model does not predict anything about the detailed atomic/ionic structures or energies of grain boundaries.

The third model we shall consider is the structural unit model. Sutton and Vitek [174] following the discovery of dense polyhedral units in grain boundary

structures [175] carried out an extensive examination of the calculated configurations of tilt boundaries in both BCC and FCC metals. They succeeded in analysing a large number of both high and low $\Sigma$ boundaries in terms of a small number of densely packed structural units. Indeed they demonstrated that favoured boundaries containing only one type of structural unit corresponded to the "special boundaries" found experimentally. They found that it was possible to move continuously from one favoured boundary (containing only structural unit $A$) to another (containing only $B$ units) by mixing $A$ and $B$ units in various ratios. Thus it appears that this model does have some predictive power, but a problem arises in that the identification of the basic structural unit is not unique [176]. For a given series of boundaries there is a hierarchy of choices of favoured or delimiting boundaries. Consequently the predictive power of this model is also limited.

We can see that none of these models provide a systematic way of predicting the low energy boundaries. They all suffer the disadvantage that there is no unique method for identifying the special boundaries. In fact the different models may predict different choices for the special boundaries. Therefore, the only reliable method for predicting the structure and properties of a given interface is by direct modeling or simulation techniques.

## 6.2 Mirror twins in hematite

A twinned crystal consists of two or more individual single crystals joined together in some definite mutual orientation. The lattices of one crystal is related to that of the other crystal by some simple symmetry operation. The most common operations are a either a rotation of 180° about a *twin axis* or a reflection in a plane known as the *twin plane*. A twin axis is always the normal to some lattice plane and a crystal twinned about such an axis is know as a rotation twin. A twin plane is always a lattice plane and a crystal twined about such a plane is know as a reflection twin. Here we shall present the calculated energies of the low index reflection (mirror) twins in hematite.

In order to generate these mirror twins in a MIDAS calculation, one block is rotated by 180° relative to the other. This is somewhat confusing considering the definitions given above but it should be noted that the rotation take place around the axis parallel to the twinning direction. This is equivalent to a reflection about that plane. In addition to this rotation the block may also have to be displaced to ensure that the structure correctly reflected about the interface.

As with surfaces we must also ensure that there is not net dipole perpendicular to the interface direction. This is most simply achieved for the mirror twins by placing two non dipolar surfaces together. However, if we examine the stacking sequences perpendicular to each of low index directions given in figure 6.1, we see that this may also be achieved by reflection about the central plane of each non-dipolar repeat unit. These are indicated with a † in figure 6.1. The resulting twin may be thought of as a "sandwich" with a single repeat unit of lattice placed between two surface terminations. The stacking sequences perpendicular to the two possible basal mirror twins are given in figure 6.2. In each case there is no net perpendicular dipole and for the case the sandwich sequences we have a plane of ions on the interfacial boundary. It is interesting to note that crystallogaphic descriptions of the basal twin in corundum structures oxides [177, 178] never consider the surface-surface possibility and only ever include the sandwich configuration as a description of the basal twin. We shall see that this is totally justified.

The energies of perfect mirror twins were calculated using MIDAS for each of the low index directions considered in the previous chapter. Here perfect means that the lattices either side of the interface were an exact mirror image of each other. This results in a perfect CSL description of the boundary; that is each coincident lattice point has an identical basis associated with them. The energies of both the surface-surface and sandwich arrangements described above were calculated. The energies are determined by comparison with a piece of bulk crystal as we did for surfaces, see chapter 4. If the energy of the piece of bulk crystal is $E_{bulk}$

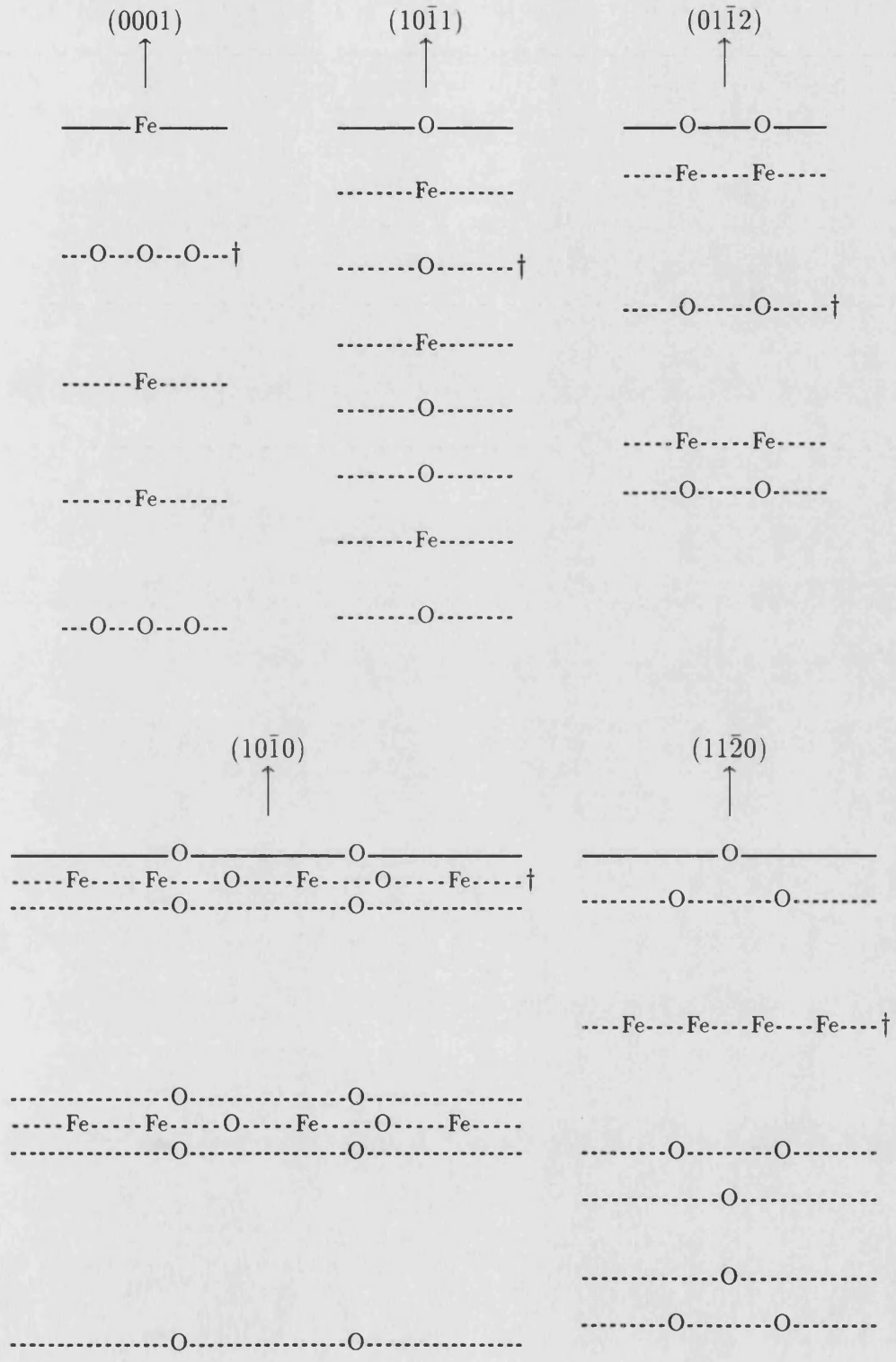


Figure 6.1: Stacking sequences perpendicular to low index directions in hematite. Sequences end in non-dipolar repeat. Center of non-dipolar repeats marked with †.

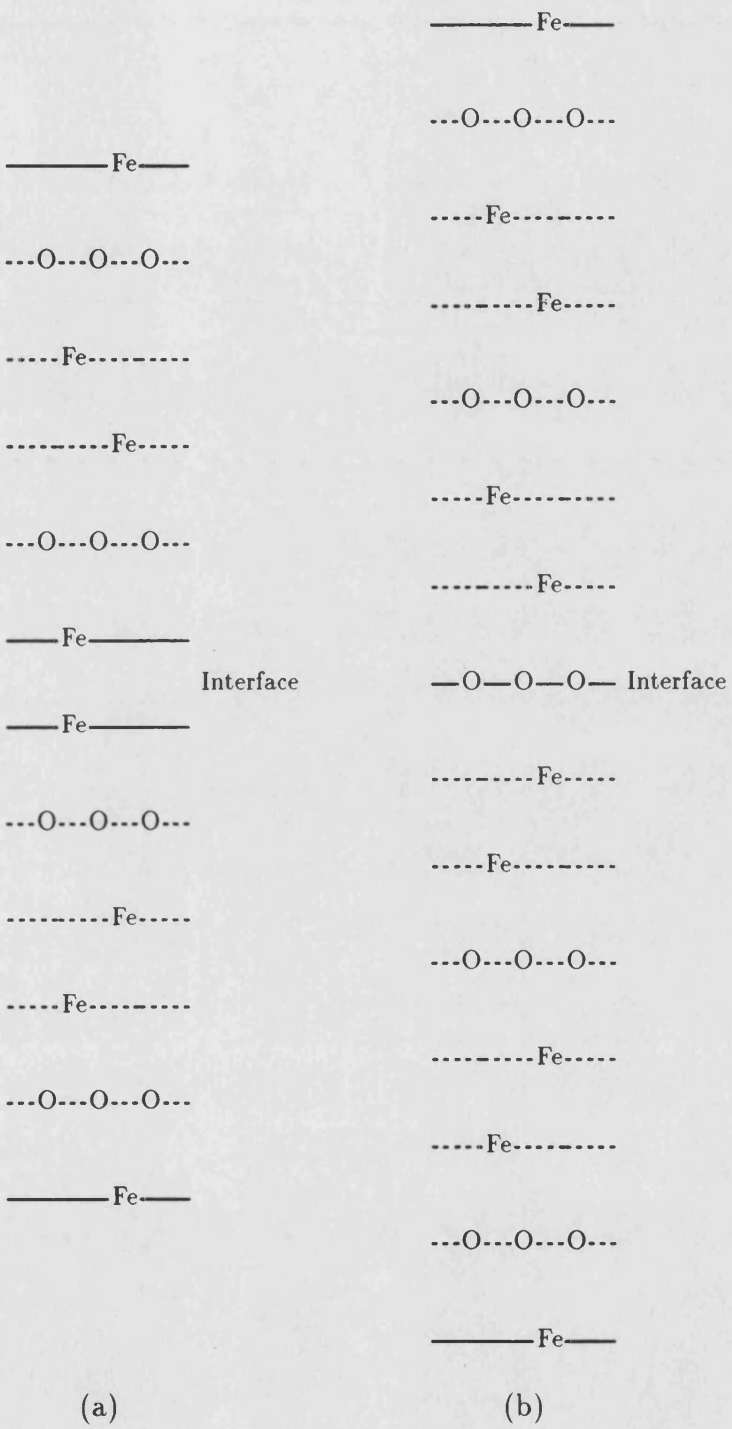


Figure 6.2: Stacking sequences for two possible mirror twin boundaries in the {0001} direction. (a) Surface-Surface configuration. (b) Sandwich configuration.

and the energy of an piece of crystal of identical size containing the boundary is $E_{twin}$, then the boundary energy is given by

$$E_{boundary} = \frac{E_{bulk} - E_{twinned}}{A}$$

where $A$ is the area of the boundary unit cell at the interface.

The energies for each of the surface-surface and sandwich mirror twin boundaries are given in tables 6.1 and 6.2 respectively. Also included is the CSL $\Sigma$ value for each boundary as determined by Grimmer [179] and the amount of dilation the boundary undergoes on relaxation. All attempts at obtaining a relaxed energy for either of the $\{10\bar{1}0\}$ perfect mirror twins failed; the boundaries dilating to a large extent but no minimum in the energy was achieved. No energy could be obtained for the unrelaxed $\{10\bar{1}0\}$ sandwich configuration due to ion overlap across the boundary. The $\{11\bar{2}0\}$ twins requires some closer examination. A twin boundary cannot form about a plane which is parallel to a mirror plane in the space group of the crystal [180]. Examining the spacegroup of hematite, i.e. R$\bar{3}$c, we see that there is a mirror plane in the $\{11\bar{2}0\}$ direction [181]. Therefore this boundary is not actually a twin boundary because no misorientation in the lattice takes place on reflection about this plane and the resulting CSL description is $\Sigma 0$. The actual structure considered is a displacement of $\frac{1}{2}[1\bar{1}0\bar{1}]$ of one half of crystal relative to the other. This could be more correctly described as constructing an antiphase boundary or a stacking fault.

The first observation of note from these tables is the generally high energy for the unrelaxed configuration, with energies ranging up to 90 $Jm^{-2}$. This is due to the large amount of repulsion between like ions on either side of the boundary, these ions being directly opposite each other because of the reflection. This repulsion is somewhat reduced in the case of the sandwich configuration due to shielding by the ions on the boundary plane. However the unrelaxed energies are still large. All the twins undergo considerable relaxation but in the case of the surface-surface configuration most of the relaxation is taken up in dilation of the

| Direction | $\Sigma$ | Unrelaxed Energy ($Jm^{-2}$) | Relaxed Energy ($Jm^{-2}$) | Dilation (Å) |
|---|---|---|---|---|
| $\{0001\}$ | 3 | 91.32 | 6.44 | 8.4 |
| $\{10\bar{1}0\}$ | 3 | 49.10 | – | – |
| $\{10\bar{1}1\}$ | 11 | 13.70 | 5.69 | 9.4 |
| $\{01\bar{1}2\}$ | 7 | 22.58 | 3.90 | 8.3 |
| $\{11\bar{2}0\}$ | 0 | 10.69 | 4.64 | 14.0 |

Table 6.1: Calculated energies of mirror twins in hematite. Surface-Surface configuration.

| Direction | $\Sigma$ | Unrelaxed Energy ($Jm^{-2}$) | Relaxed Energy ($Jm^{-2}$) | Dilation (Å) |
|---|---|---|---|---|
| $\{0001\}$ | 3 | 17.79 | 2.66 | 0.5 |
| $\{10\bar{1}0\}$ | 3 | – | – | – |
| $\{10\bar{1}1\}$ | 11 | 59.87 | 5.82 | 2.6 |
| $\{01\bar{1}2\}$ | 7 | 26.02 | 3.62 | 1.7 |
| $\{11\bar{2}0\}$ | 0 | 6.18 | 2.05 | 0.6 |

Table 6.2: Calculated energies of mirror twins in hematite. Sandwich configuration.

crystal. These dilations are huge and the resulting structure is effectively two surfaces separated by a region of empty space. This is reflected in the energies which if compared to the energies given in chapter 5 are twice the corresponding surface energies in most case with the exception of the basal plane where the twin energy is closer to three times its surface energy. In each case for the surface-surface configuration of the perfect mirror twins the formation of surfaces would be thermodynamically favoured. In the case of the sandwich configurations the relaxations are just as large but the dilations are much smaller. The twin energies in most but not all case are more stable than the corresponding surface-surface energies and the relaxed structures can be considered to be true interfaces. However the energies of these boundaries are still relatively high when compared to the corresponding surface energies.

The high energies of these perfect mirror twins can be attributed to the fact that upon reflection like ions are put in positions where maximum Coulombic repulsion is likely to occur. This repulsive energy may be removed by displacing one half of the crystal relative to the other after reflection. However, this will destroy the coincident site lattice. For the four twin boundaries considered a systematic search was made to find the displacement which achieved the minimum energy configuration. The energies of the displaced twin boundaries found to be most stable are given in tables 6.3 and 6.4. For each twin the displacement relative to the perfect configuration to achieve this minimum energy structure is also presented.

We see from both of these tables that displacement of the two halfs of the boundary results is a considerable reduction in the boundary energies both before and after relaxation. In the case of the $\{01\bar{1}2\}$ twin boundary we now predict a energy as low as 0.23 $Jm^{-2}$. In general we can see that the surface-surface configurations are the more stable than the respective sandwich configuration. The exception to this is the basal twin. Here we find that the sandwich configuration is still more stable. This is because in the sandwich configuration the

| Direction | Displacement | Unrelaxed Energy ($Jm^{-2}$) | Relaxed Energy ($Jm^{-2}$) | Dilation (Å) |
|---|---|---|---|---|
| $\{0001\}$ | $\frac{1}{2}[0\bar{1}10]$ | 7.54 | 2.14 | 0.49 |
| $\{10\bar{1}0\}$ | $\frac{1}{2}[01\bar{1}0]$ | 3.29 | 0.60 | 0.06 |
| $\{10\bar{1}1\}$ | $\frac{1}{2}[12\bar{3}1]$ | 3.94 | 1.51 | 0.28 |
| $\{01\bar{1}2\}$ | $\frac{1}{2}[01\bar{1}0]$ | 0.37 | 0.23 | -0.05 |

Table 6.3: Calculated energies of mirror twins in hematite with displacements. Surface-Surface configuration.

| Direction | Displacement | Unrelaxed Energy ($Jm^{-2}$) | Relaxed Energy ($Jm^{-2}$) | Dilation (Å) |
|---|---|---|---|---|
| $\{0001\}$ | $\frac{1}{3}[1\bar{1}00]$ | 6.39 | 1.42 | 0.12 |
| $\{10\bar{1}0\}$ | $\frac{1}{6}[0\bar{2}21]$ | 6.90 | 0.87 | 0.09 |
| $\{10\bar{1}1\}$ | $\frac{1}{6}[10\bar{1}1]$ | 14.87 | 2.22 | 0.83 |
| $\{01\bar{1}2\}$ | $\frac{1}{2}[24\bar{6}1]$ | 14.57 | 1.80 | -0.06 |

Table 6.4: Calculated energies of mirror twins in hematite with displacements. Sandwich configuration.

normal hexagonal ABAB oxygen stacking sequences is maintained for the basal plane. This allows the cations near the boundary to retain their normal octahedral coordination and hexagonal arrangement. For the {0001} surface-surface configuration the oxygen stacking sequence at the boundary is BAAB and therefore in order to maintain normal octahedral coordination the cations line up along the $(1\bar{2}10)$ direction. This results in the cation-cation separations at the boundary being shorter than in the bulk, the extra cation-cation repulsion generated destabilizes the boundary. These effects would not be seen if the oxide layer were perfectly hexagonal, the A layer could then be translated into B layer by a simple translation. For the other direction these effects do not apply, the oxide distortion perpendicular to the c direction has a larger effect on the choice of the non dipolar repeat and surface-surface configurations give the most stable structures.

Comparison of the results given here with previous calculations on the mirror twin boundaries in corundum structured oxides is difficult because of the the lack of detail provided. Mackrodt [182] has calculated the energy of the mirror twins in alumina, whereas Lawrence [132] calculated their energies in chromia. Both sets of results do not compare well with those presented here. However, this is not surprising if their results are examined closely. Both authors do not consider the sandwich configuration and therefore will not obtain the most stable basal twin. Also both authors quote energies for the $\{11\bar{2}0\}$ twin which as we noted above is not a true twin boundary. From the details provided we can assume that the previous authors have obtained different local minima and not the most stable configurations for the twin boundaries (especially in the case of the $\{11\bar{2}0\}$). Therefore comparison with the results presented here is not possible.

The study of grain boundary structures in ionic crystals is normally inhibited due to the difficulty of obtaining pure bicrystals with reliable orientation. However the {0001} and $\{01\bar{1}2\}$ twins in hematite can easily be prepared by crystal deformation [183]. The same formation mechanism has also been observed in alumina [184]. It has been noted by Bursill and Wither [185] that in samples of hematite

the rhombohedral ($\{01\bar{1}2\}$) twin is much more common than basal twin. This is inline with our calculations in which the $\{01\bar{1}2\}$ is by far and away the most stable twin. The $\{10\bar{1}0\}$ twin in hematite has also been observed experimentally as a growth twin [186]. This again is inline with out results, the $\{10\bar{1}0\}$ twin being relatively stable.

The structures of the basal twin in hematite have been discussed by Bursill and Withers [185] and hence we shall compare their proposed structures with those predicted from our calculations. For the basal twin two possible structures are proposed, both of which are based on the sandwich configuration of the boundary. The first corresponds to the perfect sandwich twin, whereas the second is described as a glide twin with a parallel transalation of $\frac{1}{3}[11\bar{2}0]$ relative to first structure. This displacement is equivalent to that given in table 6.4, i.e. $\frac{1}{3}[1\bar{1}00]$. We therefore predict the glide twin to be the preferred structure. The structures proposed by Bursill and Withers do not take into account relaxation and if we examine the relaxed structure of this twin we note an interesting phenomenon. In figure 6.3 the stacking sequences for this twin both before and after relaxation are shown. We can see that on relaxation the effective boundary plane changes. Before relaxation a oxide plane is the twinning plane, but on relaxation the cations below this plane become coplanar and now make up the boundary plane. Examining the structure in more detail in figure 6.4 we can see that the now coplanar cations occupy quite different environments. One has unoccupied octahedral cation sites above and below it, whilst the other is between occupied cation sites. Overall the structural changes are small except in the repeat unit surrounding the now coplanar cations. The changes in the normal cation arrangement at the boundary are small and very localised and therefore would be difficult to detect experimentally.

The effects of relaxation on the $\{01\bar{1}2\}$ twin are much smaller than in the case of the basal twin. This is reflected in relative small dilation at this boundary. The displacement choice in the case of the $\{01\bar{1}2\}$ twin has a more profound effect on the structure of the boundary. The undisplaced, displaced and relaxed twin

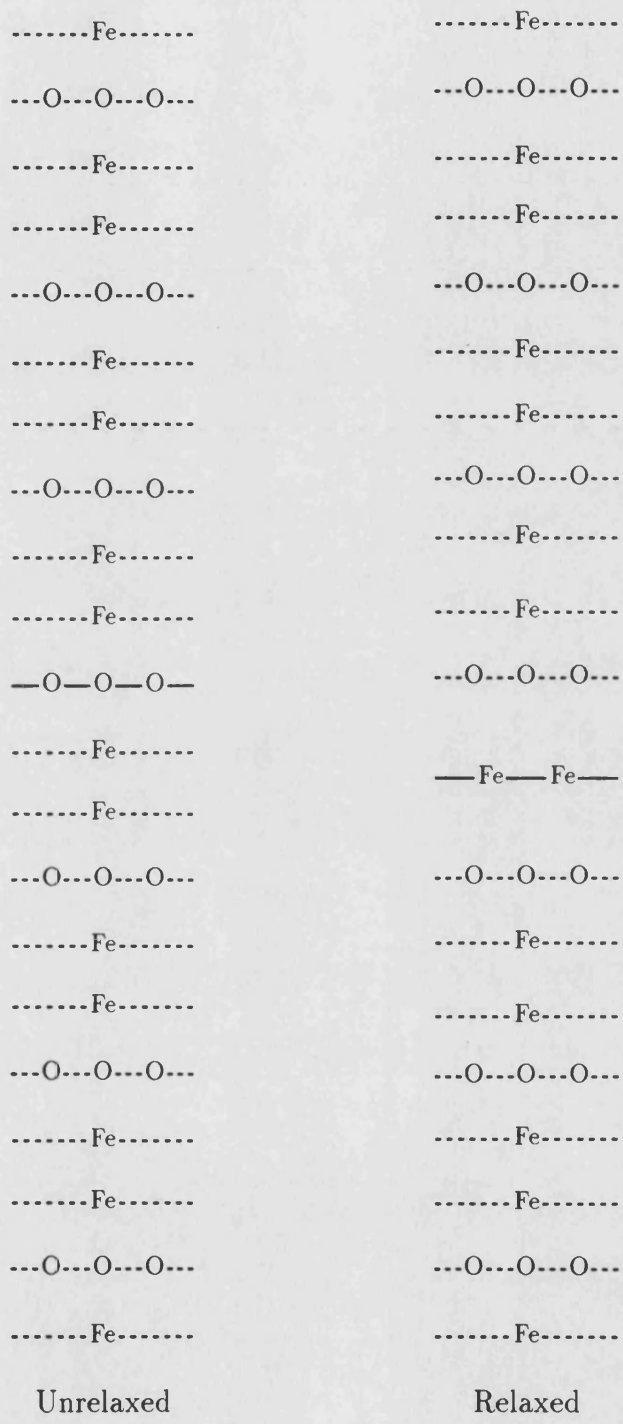


Figure 6.3: Effect on relaxation on the stacking sequence of the {0001} twin boundary.

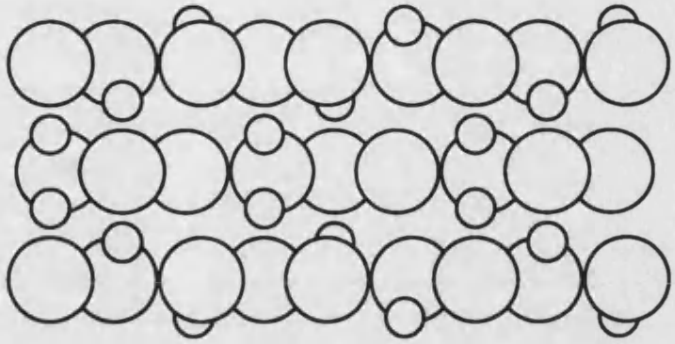

Unrelaxed perfect {0001} mirror twin.

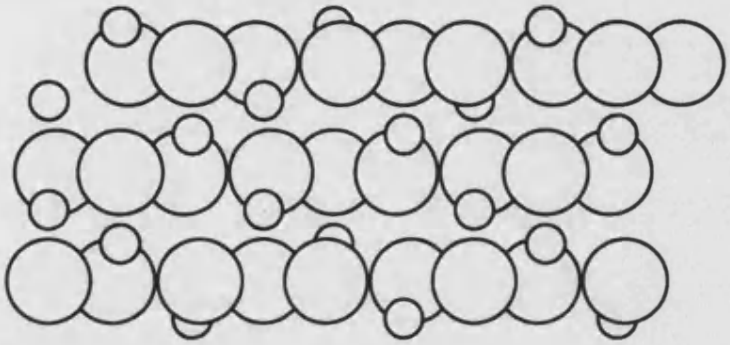

Unrelaxed displaced {0001} mirror twin.

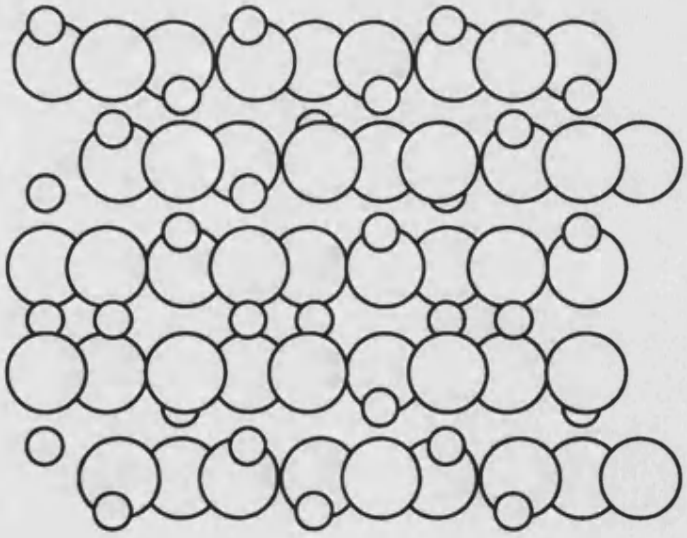

Relaxed displaced {0001} mirror twin.

Figure 6.4: Structures of the {0001} mirror twin, all views looking down the $(1\bar{2}10)$ axis. Top - perfect mirror twin sandwich configuration. Middle - Unrelaxed twin after displacement of $\frac{1}{3}[1\bar{1}00]$. Bottom - Relaxed twin.

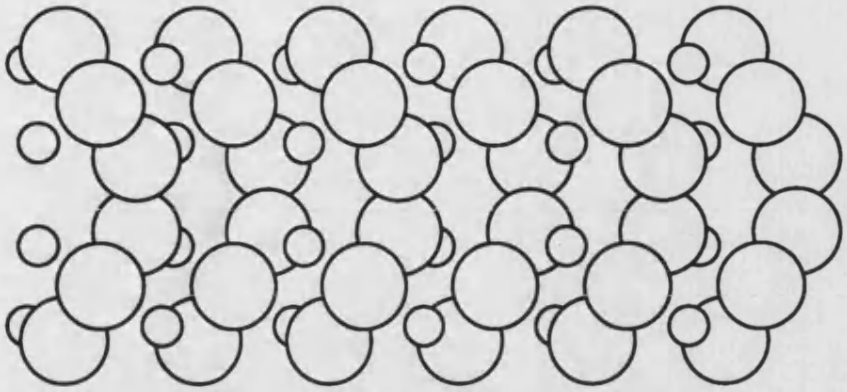

Unrelaxed perfect $\{10\bar{1}2\}$ mirror twin.

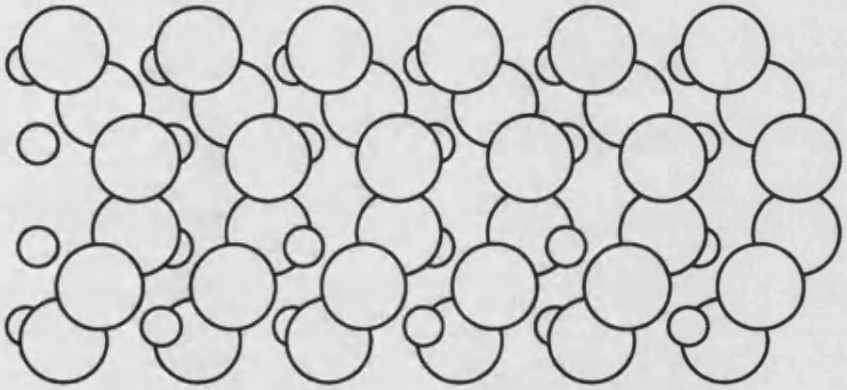

Unrelaxed displaced $\{01\bar{1}2\}$ mirror twin.

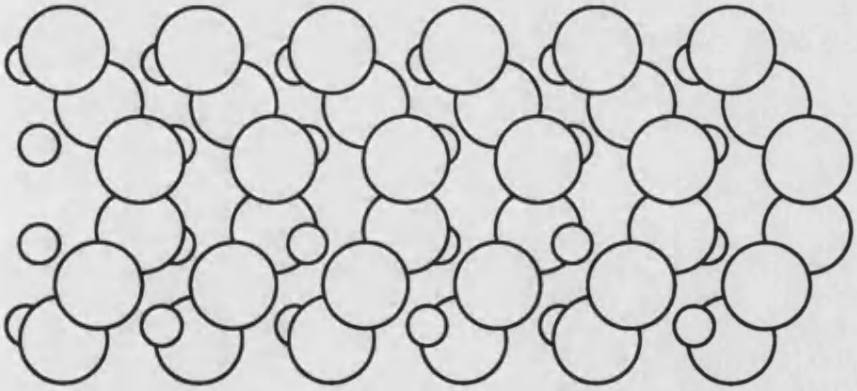

Relaxed displaced $\{01\bar{1}2\}$ mirror twin.

Figure 6.5: Structures of the $\{01\bar{1}2\}$ mirror twin, all views looking down the $(1\bar{2}10)$ axis. Top - perfect mirror twin sandwich configuration. Middle - Unrelaxed twin after displacement of $\frac{1}{2}[01\bar{1}0]$. Bottom - Relaxed twin.

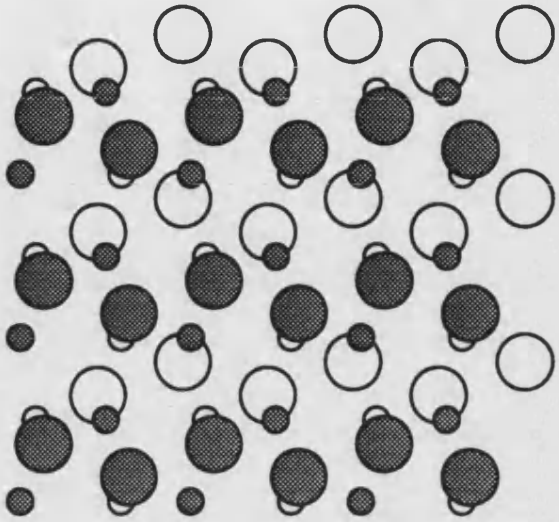

Perfect lattice

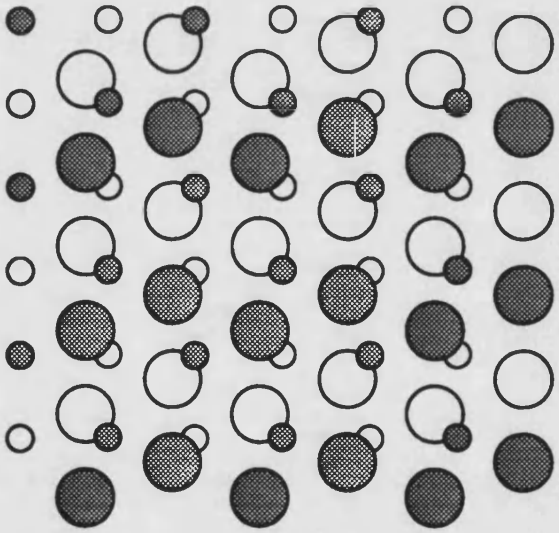

Relaxed displaced $\{01\bar{1}2\}$ mirror twin.

Figure 6.6: Structures of perfect lattice and most stable $\{01\bar{1}2\}$ mirror twin looking through the boundary. One anion and one cation layer above and below the boundary shown. Shaded ions above boundary.

boundary structures are shown in 6.5. We can see that the displacement does not seem to remove the mirror reflection in the plane about the twin boundary. However the view is slightly confusing as the displacement take place perpendicular to the page. The result of this is a staggering of the ions in the $(1\bar{2}10)$ direction. On relaxation the only change observed is a small dilation. We can compare the structure in the perfect lattice and at the twin boundary by examining figure 6.6. Here we show the view looking through the boundary plane. We see that for the twin the anions form straight rows in the $(1\bar{2}10)$ direction whereas in the perfect lattice they are staggered perpendicular to this direction.

Comparing this structure with that proposed by Bursill and Lin [187] based on their high resolution images of this twin we see some difference. The Bursill and Lin structure is similar to that shown in figure 6.6 but contains an small additional displacement which disrupts the rows of ions. The rows become staggered but to a much lesser degree than in the perfect lattice. This difference may be to the fact that our calculation correspond to zero temperature structure whereas the experiment includes the effects of temperature.

In summary we seem to have predicted the correct order of stability of the basal and rhombohedral twins and the structures we achieve are close to those proposed by experimentalists. We shall therefore proceed to consider defects at these two boundaries.

## 6.3 Vacancy formation energies close to grain boundaries

Defects tend to accumulate at grain boundaries in both metals [188] and ionic crystals [189]. The structural variation in the vicinity of the boundary can help to relieve the strain induced in a lattice by point defect. In chapter 5 we considered the vacancy formation energies close to the $\{0001\}$ and $\{01\bar{1}2\}$ surfaces, here we present the same calculations for vacancy formation energies near the basal and rhombohedral twins.

The cation and anion vacancy formation energies as a function of distance from these two boundaries are plotted in figures 6.7 to 6.10. A feature of all these graphs is the lack of symmetry about the boundary. This is cause by the presence of a small dipole at both twin boundaries. As we discussed in chapter 5, such a dipole will shift the Madelung energy of the vacancies. For a boundary the shifts will be in opposite directions on either side of the interface, thus the asymmetry is explained. For the basal twin we find a Madelung shift of 0.6 $kJmol^{-1}$ and -0.4 $kJmol^{-1}$ for the cation and anion vacancies respectively. The shifts for the rhombohedral twin are somewhat larger, at 1.2 $kJmol^{-1}$ and -0.8 $kJmol^{-1}$ for the cation and anion vacancies respectively. These are tiny when compared to the shifts generated by the surfaces, these amounted to hundreds of $kJmol^{-1}$. The presence of these shift is very disturbing, we would not expect such an asymmetry at a twin boundary. Therefore due to the small size of these shifts we contend that they are not due to a "real" dipole but are caused by computational errors. Manipulation of the ion coordinates in the CHAOS code may be introducing small changes in relative position due to rounding and other ill defined errors. Such changes could generate a dipole, but only a very small one. The fact that both boundaries show shifts in the same direction may indicated some consistency in these errors. The larger shift in the case of the rhombohedral twin may be due to its larger unit cell area, the ions are more densely packed in this direction therefore small changes in position will have a large effect.

The energies for the formation of cation and anion vacancies in the vicinity of the {0001} twin are shown graphically in figures 6.7 and 6.8 respectively. The cation vacancy energies at the boundary reflect the two different type of cation site mentioned earlier. The vacancy with the octahedral cation sites above and below occupied is stabilised with respect to the other cation site which has vacant site above and below it. The effective negative charge on the vacancy site is being stabilised by the cations above and below it. From the remainder figure 6.8 we can see that as we move away from the boundary in either direction we pass through

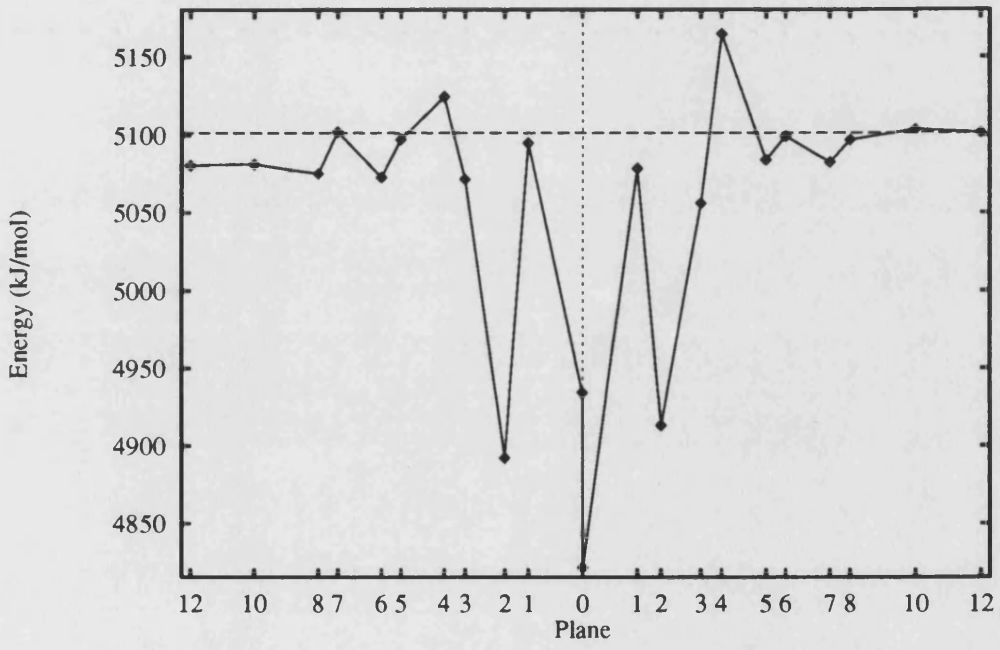


Figure 6.7: Plot of the cation vacancy energies as a function of distance from the {0001} twin boundary. Horizontal dashed line - bulk energy.

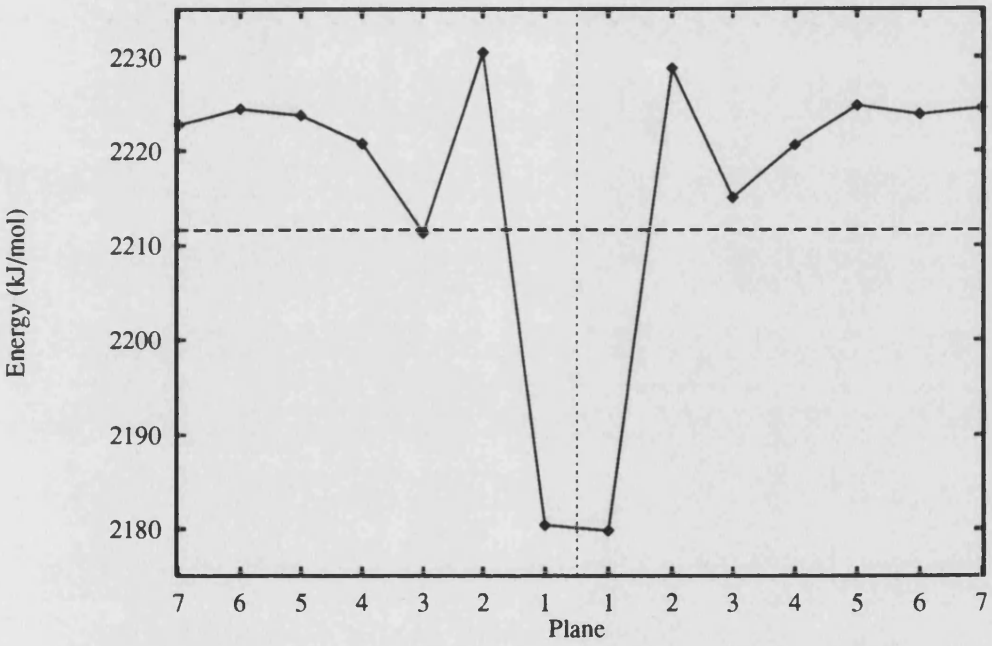


Figure 6.8: Plot of the anion vacancy energies as a function of distance from the {0001} twin boundary. Horizontal dashed line - bulk energy.

a maximum at plane four and beyond this the energies begin to converge to a fixed value. However the values on either side of the boundary are different by approximately 25 kJmol$^{-1}$. This is due to the fact that the vacancies are still relatively close to the dipolar region mentioned above which still has an effect on the relaxation process. The value on the right hand side of the graph appears closer to the bulk value than that of the left. This may reflect some differences in the way the bulk and interface energies are calculated. We note, however, that if either is assumed to be in error, the error is small amounting to 0.25% of the defect energy and is within the accuracy of the calculations.

For the anion vacancies near the {0001} twin shown in figure 6.8 we again see some some asymmetry about the boundary. This time the energies on the left converge to a value 5 kJmol$^{-1}$ less than the right. The most stable vacancies form on the planes nearest the boundary. We see a maximum at plane two and in the near boundary region we see that the most stable anion vacancy alternates between left and right up until the fourth plane after which the values begin to converge. Here again we do not see convergence to the exact bulk value.

The vacancy energies for the $\{01\bar{1}2\}$ mirror twin are given in figures 6.9 and 6.10. Again we see the vacancies are most stable closest to the boundary and that as we move away from the boundary the energies begin to converge to a fixed value. A zig zag pattern is also obvious near the boundary. For the anion vacancies near the $\{01\bar{1}2\}$ twin we find that the vacancies are more stable on plane 2. The plot appear as a W shape. Beyond this plane the energies go to a maximum at plane 5 then begin to converge to a fixed value.

In summary, we find that both types of vacancies are stabilised with respect to the bulk at the boundaries, but in the case of the anion vacancy at the $\{01\bar{1}2\}$ twin the minimum is two planes away from the boundary. Maxima in the vacancy formation energies also appear in the near boundary region. In all cases therefore we would expect an enhancement of vacancy concentration at the boundary relative to the bulk. Comparing these energies with those presented for the surfaces

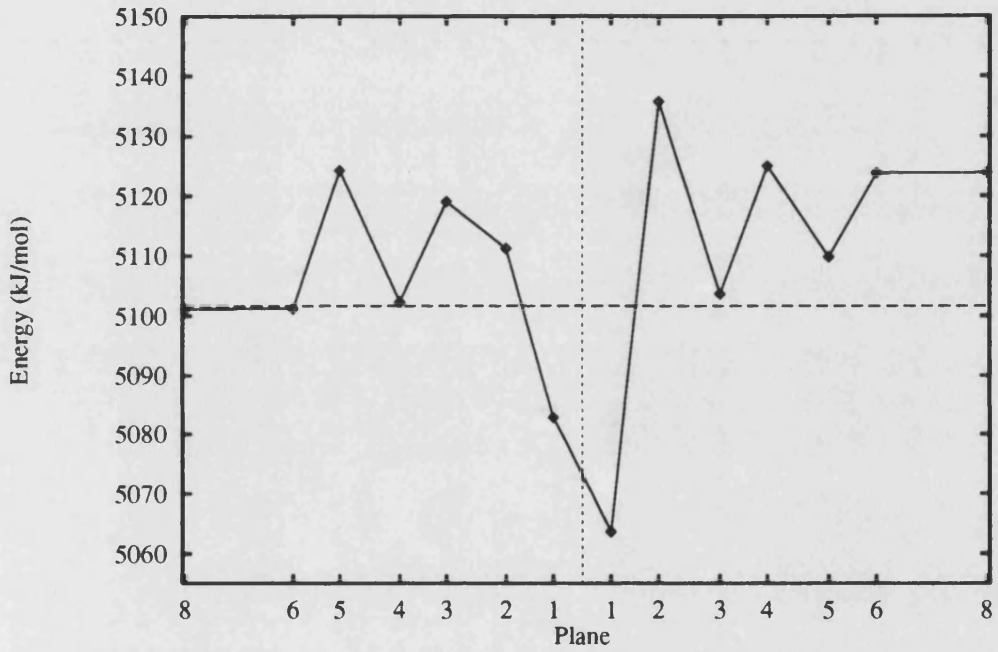


Figure 6.9: Plot of the cation vacancy energies as a function of distance from the $\{01\bar{1}2\}$ twin boundary. Horizontal dashed line - bulk energy.

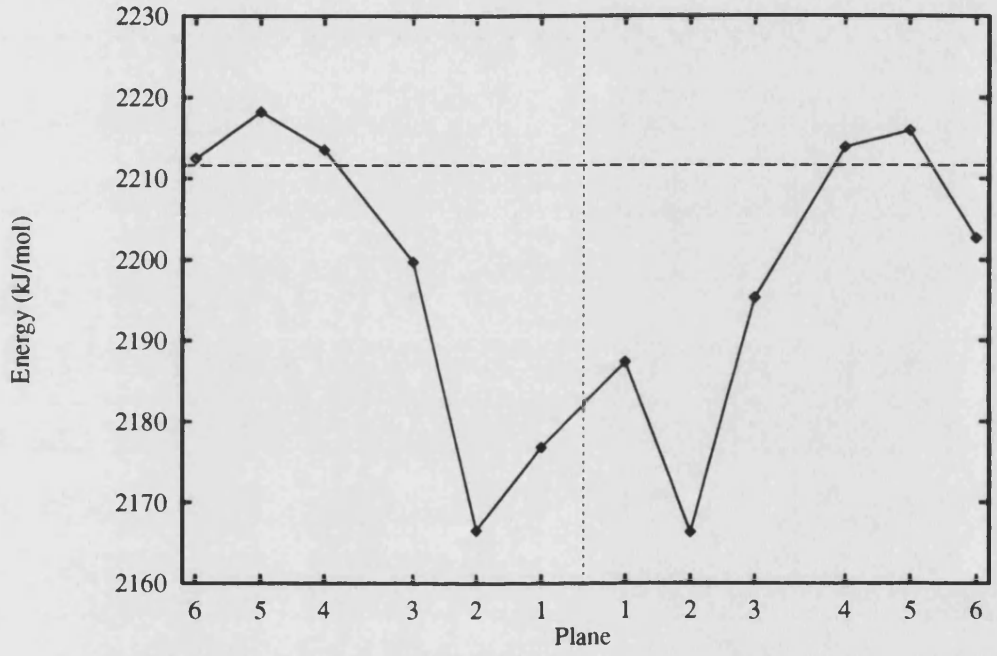


Figure 6.10: Plot of the anion vacancy energies as a function of distance from the $\{01\bar{1}2\}$ twin boundary. Horizontal dashed line - bulk energy.

in chapter 5 we see different features for the the different direction. In the case of the {0001} boundaries we find that the vacancies are stabilised more by the twin than the surface. The cation vacancy is 158 $kJmol^{-1}$ more stable at the boundary than at plane 4 below the surface, the anion vacancy is 26 $kJmol^{-1}$more stable near the twin than near the basal surface. For the $\{01\bar{1}2\}$ surface and boundary we find that the cation vacancy are stabilised by the twin but are destabilized by the surface. However, for the anion vacancy we find the formation at the surface in 50 $kJmol^{-1}$ more stable than for the boundary. Therefore we would expect an enhancement in the vacancy concentration at the two twin boundaries with respect to the surface in all but the case of the anion vacancy at the rhombohedral twin. The type and concentration of vacancies at real boundaries will be determined by space charge effects [190].

## 6.4 Isovalent impurity segregation to grain boundaries

The segregation of impurities to grain boundaries can have as large an effect on their properties as does segregation to surfaces. Grain boundary impurity segregation has been seen to effect structure, growth rates and diffusion along the boundaries [189]. Therefore we shall consider isovalent impurity segregation to the {0001} and $\{01\bar{1}2\}$ twin boundaries we generated earlier in this chapter. As with the surface calculations presented in the previous chapter we shall adopt a two site model assuming all impurities segregate to the cation layers at or closest to the boundary.

The calculated heats of segregation of $Y^{3+}$ and $Al^{3+}$ to the {0001} mirror twin are shown graphically in figure 6.11. We can see that both ions have a high heat of segregation up until half coverage above which the energies decrease rapidly. This is due to the two types of cation site present at the {0001} twin, a similar effect was seen in chapter 5 for the segregation behaviour to the $\{10\bar{1}0\}$ surface. In the case of the {0001} twin we can see from the relaxed structure given earlier that the environment surrounding the two coplanar cation at the boundary are

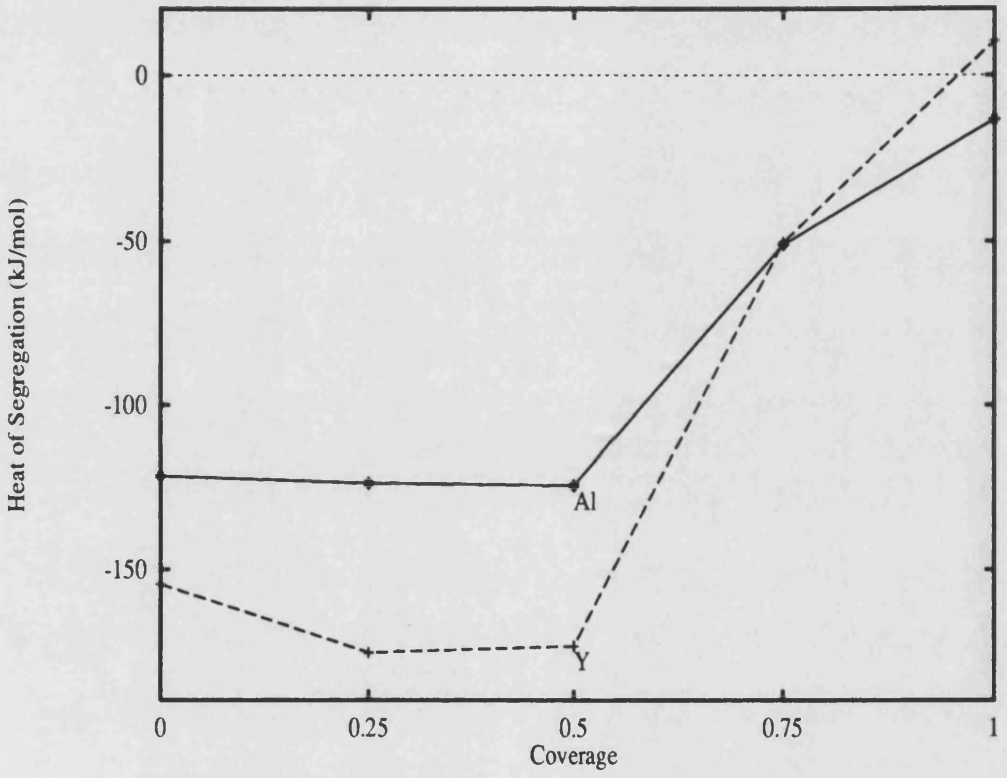


Figure 6.11: Calculated enthalpy of segregation as a function of coverage at the {0001} mirror twin.

significantly different. One cation has vacant octahedral cation sites above and below it, whereas in the case of the other cation these sites are occupied. The energy of segregating to these two sites for both impurities show large differences. In the case of $Al^{3+}$ we find that the second site (surrounding octahedral cation sites occupied) is more stable , the zero coverage heat of segregation to the other site being 83.5 $kJmol^{-1}$ i.e positive. The reverse is true for $Y^{3+}$, it prefers the first site with unoccupied surrounding octahedral sites, the zero coverage heat of segregation to the other site again being large and positive, 233 $kJmol^{-1}$. These effects are easily attributed to the different ion sizes, the large $Y^{3+}$ cation preferring the more open sites which can relax more to accommodate it. Another effect of the impurity cation size is the dilation of the relaxed boundary. For a stoichiometric boundary we found a dilation of 0.12 Å but for half coverage of $Al^{3+}$ we find the boundary actually contracts by 0.01 Å. The large $Y^{3+}$ cation at half coverage increase the dilation to 0.37 Å. We would expect such changes in the boundary structure to effect boundary phenomena such as diffusion. The energies overall follow a simple pattern once the less stable sites begin to be occupied. From the trends observed we can say that both cations would form an ordered phase at the boundary with alternate impurity/host cations and that coverages about half would be discouraged. Previous calculations by Mackrodt [182] on the segregation of $Y^{3+}$ to the {0001} mirror twin in alumina also showed a rapid decrease in the heat of segregation above half coverage. However direct comparison with the results here are difficult because, as mentioned earlier, Mackrodt only considered the surface-surface twin structure which is not the most stable arrangement.

The calculated heats of segregation for the two impurities cations to the $\{01\bar{1}2\}$ mirror twin are given in figure 6.12. In the case of the $\{01\bar{1}2\}$ boundary we considered segregation to take place to the cation layers on either side of the boundary, as there are no cations actually on the boundary plane. This allows several arrangements of the impurity, however, because the four sites are all equivalent only at half coverage will any energy difference with arrangement be observed. From

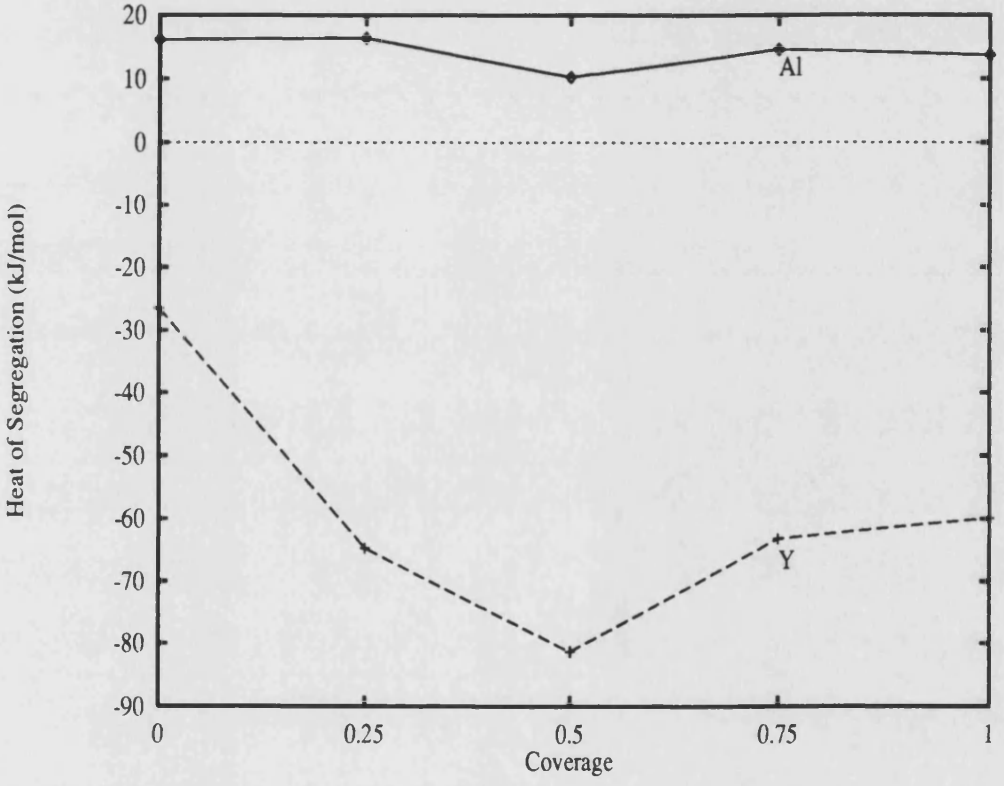


Figure 6.12: Calculated enthalpy of segregation as a function of coverage at the $\{01\bar{1}2\}$ mirror twin.

figure 6.12 we can see that we predict that $Al^{3+}$ will not segregate and $Y^{3+}$ will. Overall both impurities show the same general trends with a minimum in the segregation energy at half coverage, the minimum in the $Y^{3+}$ energies being relatively sharp. The variation of the heats of segregation can be attributed to steric hindrance at the boundary, with the $Y^{3+}$ cation showing a larger variation due to its size. Unexpectedly at half coverage both ions adopt the same arrangement at the boundary with the impurity cations preferring to occupy the two sites on the same side of the boundary. As with the {0001} twin the impurities had opposite effects on the dilation of the boundary. For $Al^{3+}$ the normal small contraction of the twin by 0.05 Å was increased at all coverages, for example at half coverage it became 0.27 Å. This may help to explain the positive heat of segregation for $Al^{3+}$. Either the extra contraction destabilizing the boundary or the boundary cannot contract enough to stabilize the $Al^{3+}$ impurity. For $Y^{3+}$ we again see a dilation of the boundary, at half coverage this is 0.50 Å.

Comparing these energies with those obtained for the free surfaces given in chapter 5 we see different trends for the two boundaries. For the {0001} twin we find the segregation energies to be approximately 100 $kJmol^{-1}$ more exothermic than for the surface. The reverse is true in the case of the $\{01\bar{1}2\}$ twin where the segregation energies are 5 and 10 $kJmol^{-1}$ less exothermic for $Al^{3+}$ and $Y^{3+}$ respectively when compared with the surface results. The differences may reflect the relative amounts of relaxation that take place at the respective surfaces and boundaries. The $\{01\bar{1}2\}$ surface and boundary undergo relatively small amounts of relaxation.

Again, as with segregation to surfaces, no direct experimental data is available for segregation to grain boundaries in hematite. However Przybylski et al [191] have observed $Y^{3+}$ segregation to grain boundaries in chromia, $Cr_2O_3$, and they report the formation of coherent and incoherent perovskite phases of stoichiometric composition of $YCrO_3$ in their chromia scales. Of course these observations were not made on well characterised boundaries but it should be noted that for

both twins we found a decrease in heat of segregation above fifty percent coverage. Calculating the equilibrium coverages using the same methods as used for the surfaces in chapter 5 we find that for the three cases when segregation occurs, a coverage of approximately 0.45 is obtained. Also as we found with some surfaces, the variations in coverage with temperature are calculated to be approximately linear and small. The heats of segregation to the boundaries obtained from such plots were all below -12 $kJmol^{-1}$.

## 6.5 Summary

In this chapter we have presented calculations on the mirror twin boundaries in hematite. We considered two possible stacking sequences for each twin. The first corresponded to placing two surfaces together whereas the second contained ions on the boundary. Perfect reflection across the boundary resulted in a large amount of Coulombic repulsion. For the surface-surface twins we found that such boundaries effectively dissociated into two surfaces.

The boundaries were stabilised by displacing one side of the boundary with respect to the other. For each twin a minimum energy displacement was determined. We found the $\{01\bar{1}2\}$ twin to be the most stable twin although comparison of the relaxed structure with an experimentally determined structure did not show total disagreement. In the case of the basal twin we determined that the so called "glide" twin [185] was more stable than the perfect sandwich configuration. In the relaxed structure of this twin we found a pair of coplanar cations.

The calculated vacancy formation energies near to basal and rhombohedral boundaries showed a small shift in the Madelung energy. This shift was attributed to a small dipole which may have been generated by rounding errors. Overall we found that the vacancies at the boundary were more stable than in the bulk. The energies were also more stable than for vacancies at the corresponding surface except in the case of anion vacancies at the $\{01\bar{1}2\}$ twin. Enhancement of vacancy concentration at the twin boundaries is therefore predicted.

Segregation energies for $Y^{3+}$ and $Al^{3+}$ were also calculated for the basal and rhombohedral twin. A cutoff at half coverage for both impurities at both boundaries was observed. This is in accord to what is observed in chromia [191]. Comparing theses results with the surface segregation energies given in chapter 5 we found an enhancement of segregation energy to the basal twin with respect to the surface. The opposite was true for the rhombohedral twin where the segregation energies for $Al^{3+}$ were all positive.

## Conclusions

This thesis has been concerned with the application of computer simulation techniques to the study of the surfaces and grain boundaries of oxides. In this work we have made two major achievements. The first is the extension of surface simulation to spinels and forsterite. The spinels are ternary oxides where all the low index surfaces are dipolar, whereas forsterite is a silicate. The second achievement was the determination of the minimum energy configurations of the mirror twins in hematite.

In chapter 4, calculations of the surface energies of a range of oxides were presented. We saw that for the cubic oxide FeO surface relaxation has no effect on the relative order of stabilities of the surfaces and that the {100} surface undergoes almost no relaxation. For the other oxides considered, however, we saw that surface relaxations were large and surface specific. These relaxations often had a large effect on the relative stabilities of the surfaces. We found that for rutile, $TiO_2$, the unrelaxed surface energies predicted the {101} surface to be the most stable, whereas, after relaxation the {110} surface became the most stable. This is in accord with experiment. These changes in order were reflected in the predicted equilibrium morphologies where a comparison with experimental crystals showed better agreement when using relaxed surface energies.

For the spinels, $MgAl_2O_4$, and magnetite, $Fe_3O_4$, the results in chapter 4 showed that the choice of terminating surface plane was very important. We found that the spinel, $MgAl_2O_4$, {110} and {111} surfaces could be stabilized by inversion of the cation distribution at the surface. This brought the divalent cation to the surface plane. Similarly for magnetite, an inverse spinel, we found that surfaces terminating in divalent cations were the more stable. For both these compounds, comparison of the predicted equilibrium morphologies with experiment were difficult. The experimental crystal morphologies appear to be dominated by kinetic effects.

The surface energies of forsterite, $Mg_2SiO_4$, were also considered in chapter 4. Here we found that use of a three body bond bending potential had little or no effect on the calculated surface energies. A more important consideration was the maintenance of silicon saturation. the formation of surfaces maintaining the tetrahedral coordination of silicon required strict planar cleavage to be abandoned. The predicted morphologies of forsterite compared well with experiment.

In chapter 5 we considered the pure and defective low index surfaces of hematite. A comparison of the calculated surface energies with previous calculations indicated some dependance on the potential used. When the equilibrium morphologies predicted by the previous calculations and those presented here were compared, however, we saw that our calculations fitted the experimental morphology data more closely. In addition to considering the perfect surface we went on to consider defects at the surfaces. Firstly we considered the vacancy formation energies near the $\{0001\}$ and $\{01\bar{1}2\}$ surfaces. The calculated bulk and surface defect energies could not be compared directly because of a shift the Madelung energy caused by a surface dipole generated by surface relaxation. In addition, image charge effects must also be taken into account at the surface. We found that after taking account of these two effects, the vacancy formation energies for either type of vacancy were more favourable than for the bulk at certain specific sites near or at the surface. This would indicate an enhanced vacancy concentration near surfaces. We then went on to consider the isovalent impurity segregation to the surface of hematite. We found that simple arguments based on elastic strain predicted the relative order of the the heats of segregation for $Y^{3+}$ and $Al^{3+}$ but that for $Cr^{3+}$ this model broke down. $Cr^{3+}$ showed several minima in its heat of segregation which could be attributed to the formation of ordered phases. For the large $Y^{3+}$ cation steric effects were shown to have a large effect on the variation of the heat of segregation with coverage. Calculated equilibrium coverages based on these heats of segregation were seen to produce linear plots with respect to reciprocal temperature, and segregation energies obtained from the slope of these plots

were found to very different from the calculated heats of segregation. In the case of $Y^{3+}$, energies obtained from such plots were similar to those obtained experimentally for polycrystalline alumina. This apparent agreement cannot however be taken a face value as there could be many ways to obtain similar agreement.

In chapter 6 we considered grain boundaries in hematite. The energies of the mirror twins were calculated. Two possible stacking sequences for each twin were considered. We found that the perfect mirror twins were relatively unstable but that they could be stabilized by displacing one side of the boundary with respect to the other. Minimum energy configurations were determined for each twin by means of these displacements. It was demonstrated that for the basal twin the glide version was the more stable, and that on relaxation the cations at the boundary became coplanar. Segregation and vacancy formation energy calculations were also performed for the {0001} and $\{01\bar{1}2\}$ twins. For vacancies we found that the formation energies at or close to the boundary were well below the bulk values, therefore we would expect enhanced vacancy concentration at the grain boundaries. The isovalent impurity segregation calculations indicated a cutoff in the boundary concentration at half coverage. Comparing the energies with the corresponding surfaces we found an enhanced heat of segregation at the basal twins, while the reverse was true for the rhombohedral twin.

To conclude, this work has shown the range and versatility of atomistic simulation when applied to surfaces and boundaries. We have seen that where experimental data is available relatively good agreement has been achieved. These results could have important implication for catalytic and corrosion process. Segregation to hematite surface and boundaies will effect iron corrosion, materials such as yttrium are added to steels to increase there corrosion resistance. The rearrangement of the cation distribution and the favouring of divalent cation and spinel surfaces will effect their use as catalyst.

In using equilibrium morphologies as a means of comparing calculated properties with experimental properties we saw that in several cases agreement was

bad, we assumed this to be due to kinetic effects dominating the real morphology. The use of morphologies as a tool for comparing simulation and experimental results could therefore be improved if the mechanism of crystal growth could be simulated. Addition of entropic and temperature effects could only improve the reliabilty and versatility of these methods.

## References


[1] D. A. Bonnell and D. R. Clarke. *J. Am. Ceram. Soc.*, 71 629, 1989.

[2] G. Binnig, C. F. Quate, and C. Gerber. *Phys. Rev. Lett.*, 56 930, 1986.

[3] J. Nowotny and L. C. Dufour (Eds). *Mat. Sci. Mon. Volume 47.* Elsevier, Oxford, 1988.

[4] J. Roubort, S. J. Rothman, B. K. Flandmeyer L. J. Nowicki, and J. E. Baker. *J. Mat. Sci. Res.*, 2 116, 1988.

[5] T. M. French and G. A. Somorjai. *J. Phys. Chem.*, 74 2489, 1970.

[6] J. B. Pendry. *Low Energy Electron Diffraction.* Academic Press, London, 1974.

[7] G. Binnig and H. Rohrer. *Helv. Phys. Acta*, 55 726, 1982.

[8] S. Baik, D. E. Fowler, J. M. Blakely, and R. Raj. *J. Am. Ceram. Soc.*, 68 281, 1985.

[9] J. D. Cawley and J. W. halloran. *J. Am. Ceram. Soc.*, 68 281, 1986.

[10] W. Hirschwald. In *Mat. Sci. Mon. Volume 47.* Elsevier, Oxford, 1988.

[11] H. F. Fischmeister. In J. A. Pask and A. G. Evans, editors, *Ceramic Microstructures 86*, page 1. Plenum Press, London, 1986.

[12] S. Hegege, C. B. Carter, F. Cosandey, and S. L. Sass. *Phil. Mag. A*, 45 723, 1982.

[13] K. L. Merkle and D. J. Smith. *Phys. Rev. Lett.*, 59 2887, 1987.

[14] M. J. Norgett and A. B. Lidiard. *Phil. Mag.*, 18(1193), 1968.

[15] C. R. A. Catlow. PhD thesis, Oxford, 1974.

[16] M. J. L. Sangster and A. M. Stoneham. *Phil. Mag. B*, 43 597, 1981.

[17] R. James. PhD thesis, London, 1979.

[18] G. V. Lewis and C. R. A. Catlow. *Radiat. Eff.*, 73 307, 1983.

[19] S. C. Parker. PhD thesis, University of London, 1983.

[20] P. W. Tasker. *Phil. Mag. A*, 39 119, 1979.

[21] W. C. Mackrodt, P. W. Tasker, and E. A. Colbourn. *Surf. Sci.*, 152/153 940, 1985.

[22] P. W. Tasker. In W. D. Kingery, editor, *Advances in Ceramics Volume 10*, page 176. The American Ceramic Society, Columbux, Ohio, 1984.

[23] D. M. Duffy and P. W. Tasker. Technical Report TP953, AERE Harwell, Theoretical Physics Division, Harwell Laboratory, Oxfordshire OX11 0RA, U.K., 1982.

[24] D. M. Duffy and P. W. Tasker. *Phil. Mag. A*, 47 817, 1983.

[25] D. M. Duffy and P. W. Tasker. *Phil. Mag. A*, 54 759, 1986.

[26] P. W. Tasker and A. M. Stoneham. *J. Chim. Phys.*, 84 147, 1987.

[27] A. M. Stoneham. *Appl. Surf. Sci*, 14 249, 1982/3.

[28] A. M. Stoneham and P. W. Tasker. *J. Phys. C*, 18 L543, 1985.

[29] J. H. Harding. *Physica B*, 131 13, 1985.

[30] W. C. Mackrodt and P. W. Tasker. *J. Am. Ceram. Soc.*, 72 1576, 1989.

[31] S. K. Rhee. *J. Am. Ceram. Soc.*, 58 441, 1975.

[32] G. Wulff. *Z. Kristallogr. Kristallgeom.*, 34 449, 1901.

[33] D. Wolf. *J. Physique Coll.*, 43 C645, 1982.

[34] P. W. Tasker. Technical Report AERE R 9130, AERE Harwell, Theoretical Physics Division, Harwell Laboratory, Oxfordshire OX11 0RA, U.K., 1978.

[35] D. M. Duffy and P. W. Tasker. Technical Report AERE R 11059, AERE Harwell, Theoretical Physics Division, Harwell Laboratory, Oxfordshire OX11 0RA, U.K., September 1983.

[36] M. Born and K. Huang. *Dynamical Theory of Crystal Lattices.* Oxford University Press, Oxford, 1954.

[37] P. P. Ewald. *Ann. Physik*, 64 253, 1921.

[38] D. E. Parry. *Surf. Sci.*, 49 433, 1975.

[39] D. E. Parry. *Surf. Sci.*, 54 195, 1976.

[40] M. P. Tosi. *Solid State Physics*, 16 1, 1964.

[41] D. M. Heyes, M. Barber, and J. H. R. Clarke. *J. Chem. Soc. Farad. Trans.*, 10 1485, 1977.

[42] J. H. Harding. Technical Report AERE R 13127, AERE Harwell, Theoretical Physics Division, Harwell Laboratory, Oxfordshire OX11 0RA, U.K., May 1988.

[43] W. C. Davidon. Technical Report ANL-5990 (Rev), Argonne Nat. Lab., 1963.

[44] R. Fletcher and M. J. D. Powell. *Computer J.*, 6 163, 1963.

[45] J. T. Kummer and Y. Y. Yao. *Can. J. Chem.*, 45 421, 1967.

[46] M. J. Norgett. Technical Report R7650, Harwell Lab., 1974.

[47] N. F. Mott and M. J. Littleton. *Trans. Farad. Soc.*, 34 485, 1938.

[48] J. D. Jackson. *Classical Electrodynamics.* Wiley, New York, 1962.

[49] A. M. Stoneham and M. J. L. Sangster. *Phil. Mag. B*, 52 717, 1985.

[50] G. V. Lewis and C. R. A. Catlow. *J. Phys. C*, 18 1149, 1985.

[51] M. J. Sanders, M. Leslie, and C. R. A. Catlow. *J. Chem. Soc. Chem. Commun.*, page 1273, 1984.

[52] G. D. Price, S. C. Parker, and M. Leslie. *Phys. Chem. Miner.*, 15 181, 1987.

[53] C. R. A. Catlow, M. J. Dixon, and W. C. Mackrodt. In *Computer Simulation of Solids*, page 130. Springer-Verlag, New York, 1982.

[54] A. B. Woods, W. Cochran, and B. N. Brockhouse. *Phys. Rev. B*, 119 980, 1960.

[55] M. J. Norgett. *J. Phys. C*, 4 298, 1971.

[56] R. Tubino, L. Piseri, and G. Zerbi. *J. Chem. Phys.*, 56 1022, 1972.

[57] I. D. Faux. *J. Phys. C*, 4 L211, 1971.

[58] B. G. Dick and A. W. Overhauser. *Phys. Rev. B*, 112 90, 1958.

[59] C. R. A. Catlow and W. C. Mackrodt. *Computer Simulation of Solids.* Springer-Verlag, New York, 1982.

[60] P. T. Weedpohl. *Proc. Phys. Soc.*, 56 3122, 1972.

[61] P. Weedpohl. *J. Phys. C*, 10 1855, 1977.

[62] Y. S. Kim and R. G. Gordon. *J. Chem. Phys.*, 60 1842, 1974.

[63] W. C. Mackrodt and R. F. Stewart. *J. Phys. C*, 12 431, 1979.

[64] C. R. A. Catlow and A. M. Stoneham. *J. Phys. C*, 16 4321, 1983.

[65] C. R. A. Catlow. *Proc. R. Soc. A*, 333 533, 1977.

[66] C. R. A. Catlow, C. M. Freeman, and R. L. Royle. *Physica*, 131*B* 1, 1985.

[67] T. Young. *Phil. Trans. R. Soc. Lond.*, page 65, 1805.

[68] P. S. Laplace. *Mécanique céleste.* 1806.

[69] R. Shuttleworth. *Proc. Phys. Soc. London Sect. A*, 62 167, 1949.

[70] S. C. Parker and G. D. Price. *Advances in Solid State Chemistry*, 1 295, 1989.

[71] N. M. Parikh. *J. Am. Ceram. Soc.*, 41 18, 1958.

[72] W. D. Kingery. *J. Am. Ceram. Soc.*, 37 42, 1954.

[73] P. Nikolopoulos. *J. Mat. Sci.*, 20 3993, 1985.

[74] A. R. C. Westwood and D. L. Goldheim. *J. Appl. Phys.*, 34 3085, 1963.

[75] S. G. Lipsett, F. M. G. Johnson, and O. Maass. *J. Amer. Chem. Soc.*, 49 1940, 1927.

[76] K. Kendall, N. McN. Alford, and J. D. Birchall. *Proc. R. Soc. Lond. A*, 412 269, 1986.

[77] J. J. Bikerman. *Physica Status Solidi*, 10 2, 1965.

[78] J. J. Duga. Surface energy of ceramic materials. Technical Report Rept. 69-2, Defence Ceramic Information Center, 1969.

[79] J. W. Gibbs. *On the Equilibrium of Heterogeneous Substances*, volume I of *Collected Works*, page 55. Longmans, New York, 1928.

[80] H. Hilton. *Mathematical Crystallography.* Oxford, 1903.

[81] H. Liebman. *Z. Kristallogr.*, 53 171, 1914.

[82] M. von Laue. *Z. Kristallogr.*, 105 124, 1943.

[83] M. Volmer. *Kinetik der Phasenbildung.* Steinkopff, Leipzig, 1939.

[84] I. N. Stranski. *Z. Phys. Chem.*, *B*38 451, 1938.

[85] R. F. Strikland-Constable. *Kinetics and Mechanism of Crystallization.* Academic Press, London and New York, 1968.

[86] R. Kern. *Morphology of Crystals, Part A*, chapter 2. Terra Scientific Publishing Company, Tokyo, 1990.

[87] E. Dowty. *Am. Mineralogist*, 65 446, 1980.

[88] L. S. Darken and R. W. Gurry. *J. Am. Chem. Soc.*, 68 798, 1946.

[89] F. A. Cotton and G. Wilkinson. *Advanced Inorganic Chemistry*, chapter 21, page 752. Wiley-Interscience, fourth edition, 1980.

[90] J. R. Gavarri, D. Weigel, and C. Carel. *Mater. Res. Bull.*, 11 917, 1976.

[91] W. C. Mackrodt. *Phys. Chem. Miner.*, 15 228, 1988.

[92] V. E. Henrich. *Rep. Prog. Phys.*, 48 1481, 1985.

[93] R. E. Cech and E. I. Alessandrini. *Trans. Am. Soc. Metals*, 51 150, 1959.

[94] M. Prutton, J. A. Walker, M. R. Welton-Cook, and R. C. Felton. *Surf. Sci.*, 89 95, 1979.

[95] A. J. Pignocco and G. E. Pellissier. *J. Electrochemical Soc.*, 112 1188, 1965.

[96] Masaoki Oku and Kichinosuke Hirokawa. *J. Appl. Phys.*, 50 6303, 1979.

[97] T. Gotoh, S. Murakami, K. Kinosita, and Y. Murata. *J. Phys. Soc. Japan*, 50 2063, 1981.

[98] M. R. Welton-Cook and W. Berndt. *J. Phys. C*, 15 5691, 1982.

[99] A. von Hippel. *J. Phys. Chem. Solids*, 23 779, 1962.

[100] C. R. Catlow, C. M. Freeman, M. S. Islam, R. A. Jackson, M. Leslie, and S. M. Tomlinson. *Phil. Mag. A*, 58 123, 1988.

[101] V. E. Henrich and R. L. Kurtz. *J. Vac. Sci. Technol.*, 18 416, 1981.

[102] V. E. Henrich. *Prog. Surf. Sci.*, 14 175, 1983.

[103] W. Gospel, J. A. Anderson, D. Frankel, M. Jacknig, K. Philips, J. A. Schafer, and G. Rocher. *Surf. Sci.*, 139 333, 1984.

[104] Y. W. Chung, W. J. Lo, and G. A. Somorjai. *Surf. Sci.*, 64 588, 1977.

[105] V. E. Henrich and R. L. Kurtz. *Phys. Rev. B*, 23 6280, 1981.

[106] L. E. Firment. *Surf. Sci.*, 116 205, 1982.

[107] R. H. Tait and R. V. Kasowski. *Phys Rev B*, 20 5178, 1979.

[108] W. E. Ford. *Dana's Textbook of Mineralogy.* Chapman and Hall Ltd, London, fourth edition, 1932.

[109] W. A. Deer, R. A. Howie, and J Zussman. *An Introduction to Rock Forming Minerals.* Longman Group Ltd, London, 1966.

[110] L. G. Berry and B. Mason. *Mineralogy.* W. H. Freeman and Company, London, 1959.

[111] T. Oota, I. Yamai, and M. Yokoyama. *J. Crystal Growth*, 66 262, 1984.

[112] C. W. Correns. *Introduction to Mineralogy.* Allen and Unwin Ltd, London, 1969.

[113] J. S. Berkes, W. B. White, and R. Roy. *J. Applied Physics*, 10 3276, 1965.

[114] D. W. Susnitzky, Y. Kouh Simpson, B. C. De Cooman, and C. B. Carter. In *Defect Properties and Processing of High-Technology Nonmetallic Materials, Volume 60*, page 219. Materials Research Society, Pittsburgh, Pennsylvania, 1986.

[115] J. L. Hutchinson and N. A. Briscoe. *Ultramicroscopy*, 18 435, 1985.

[116] R. K. Mishra and G. Thomas. *J. Appl. Phys.*, 48 4577, 1977.

[117] W. Ebert and H. H. Kung. *Phil. Mag. B*, 52 1135, 1985.

[118] T. Fujii, M. Takano, R. Katano, and Y. Bando. *J. Appl. Phys.*, 68 1735, 1990.

[119] F. Heider and L. T. Bryndzia. *J. Crystal Growth*, 84 50, 1987.

[120] W. Feitknecht. *Helvetica Chimica Acta*, XLV 2042, 1962.

[121] M. N. Viswanathiah, J. A. K. Tareen, and K. V. Krishnamurthy. *J. Crystal Growth*, 49 189, 1980.

[122] S. Hirano and S Somiya. *J. Crystal Growth*, 35 273, 1976.

[123] M. Oda and N. Saegusa. *Japanese Journal of Applied Physics*, 24 L702, 1985.

[124] R. M. Hazen. *American Mineralogist*, 61 1280, 1976.

[125] J. 't Hart. *Acta Cryst A*, 31(S) S214, 1975.

[126] S. Hosoya and H. Takei. *J. Crystal Growth*, 57 343, 1982.

[127] M. Shelef, M. A. Z. Wheeler, and H. C. Yoa. *Surf. Sci.*, 47 697, 1975.

[128] G. K. Lewis Jr. and H. G. Drickamer. *J. Chem. Phys.*, 45 224, 1966.

[129] J. Heil, J. Wesner, B. Lommel, W. Assmus, and W. Grill. *J. Appl. Phys.*, 65 5220, 1989.

[130] R. L. Kurtz and V. E. Henrich. *Physical Review B*, 36 3413, 1987.

[131] W. C. Mackrodt, R. J. Davy, S. N. Black, and R. Docherty. *J. Crystal Growth*, 80 441, 1987.

[132] P. J. Lawrence. PhD thesis, School of Chemistry, University of Bath, 1989.

[133] P. Hartman. *Crystal Growth: An Introduction*, chapter 14. North-Holland, Amsterdam, 1973.

[134] P. Hartman. *J. Crystal Growth*, 49 166, 1980.

[135] J. Bessières and R. Baro. *J. Crystal Growth*, 18 225, 1973.

[136] P. W. Tasker. Technical Report TP 999, AERE Harwell, Theoretical Physics Division, Harwell Laboratory, Oxfordshire OX11 0RA, U.K.

[137] P. R. Kenway. PhD thesis, School of Chemistry, University of Bath, 1991.

[138] J. Bessières and R. Baro. *J. Crystal Growth*, 19 218, 1973.

[139] G. Garton, S. H. Smith, and B. M. Wanklyn. *J. Crystal Growth*, 13/14 588, 1972.

[140] M. Maurice. *Neuses Jahrb. Mineral Geol. Pal. Abh. Beil*, A63 279, 1932.

[141] H. Biäsch. *Z. Krist.*, 70 1, 1929.

[142] P. Hartman. *J. Crystal Growth*, 96 667, 1989.

[143] K. E. Smith, J. L. Mackay, and V. E. Henrich. *Physical Review B*, 35 5822, 1987.

[144] J. Frenkel. *Kinietic Theory of Liquids.* Oxford University Press, 1946.

[145] D. M. Duffy and A. M. Stoneham. *J. Phys. C*, 16 4087, 1983.

[146] D. M. Duffy, J. P. Hoare, and P. W. Tasker. *J. Phys. C*, 17 L195, 1984.

[147] A. M. Stoneham and P. W. Tasker. *Phil. Mag. B*, 55 237, 1987.

[148] R. J. Lad and V. E. Henrich. *Surf. Sci.*, 193 81, 1988.

[149] P. J. Lawrence, S. C. Parker, and P. W. Tasker. *J. Am. Ceram. Soc.*, 71 C389, 1988.

[150] D. W. Budworth. *An introduction to Ceramic Science.* Pergammon Press, Oxford, 1970.

[151] R. L. Coble. *J. Appl. Phys.*, 32 793, 1961.

[152] R. C. Johnson and R. L. Coble. *J. Am. Ceram. Soc.*, 61 110, 1978.

[153] P. Wynblatt and R. C. McCune. In J. Pask and A. Evans, editors, *Surfaces and Interfaces in Ceramic and Ceramic-Metal Systems*, page 83. Plenum Press, Newyork and London, 1980.

[154] P. W. Tasker, E. A. Colbourn, and W. C. Mackrodt. *J. Am. Ceram. Soc*, 68 74, 1985.

[155] W. C. Mackrodt. In C. R. A. Catlow and W. C. Mackrodt, editors, *Advances in Ceramics, Volume 23*, page 293. The American Ceramic Society, Westerville, Ohio, 1987.

[156] W. C. Mackrodt and P. W. Tasker. *Mater. Res. Soc. Symp. Proc.*, 60 291, 1986.

[157] D. McLean. *Grain Boundaries in Metals.* Clarendon Press, London, 1957.

[158] J. D. Eshelby. *Solid State Physics*, 3 79, 1956.

[159] *Handbook of Chemistry and Physics.* CRC Press Inc, Boca Raton, Florida, 70 edition, 1989.

[160] R. C. McCune. In *Applied Material Characterization.* 1985.

[161] R. C. McCune, W. T. Donlon, and R. C. Ku. *J. Am. Ceram. Soc.*, 69 C196, 1986.

[162] P. Masri, P. W. Tasker, J. P. Hoare, and J. H. Harding. *Surf. Sci.*, 173 439, 1986.

[163] W. D. Kingery. *J. Am. Ceram. Soc.*, 57 1, 1974.

[164] R. W. Balluffi and P. D. Bristowe. *Surf. Sci.*, 144 28, 1984.

[165] M. Rühle, R. W. Balluffi, H. Fischmeister, and S. L. Sass. *J. Physique Coll.*, 46, 1985.

[166] D. M. Duffy and P. W. Tasker. *Phil. Mag. A*, 50 155, 1984.

[167] D. M. Duffy. *J. Phys. C*, 19 4393, 1986.

[168] J. M. Burges. *Proc. K. Ned. Akad. Wet. Ser. B*, 42 293, 1939.

[169] W. L. Bragg. *Proc. Phys. Soc.*, 52 54, 1940.

[170] W. T. Read and W. Shockley. *Phys. Rev.*, 78 275, 1950.

[171] R. C. Pond and V. Veitek. *Proc. R. Soc. A*, 357 453, 1977.

[172] M. J. Wiens, H. Gleiter, and B. Chalmers. *J. Appl. Phys.*, 42 2639, 1971.

[173] P. J. Goodhew. In *Grain Boundary Structure and Kinetics*, page 155. American Society of Metals, Ohio: Metals Park, 1980.

[174] A. Sutton and V. Veitek. *Phil. Trans. Roy. Soc. A*, 309 1, 1983.

[175] M. F. Ashby, F. Spaepen, and S. Williams. *Acta Metall.*, 26 1647, 1978.

[176] R. W. Balluffi and P. D. Bristowe. *Surf. Sci.*, 144 28, 1084.

[177] K. J. Morrissey and C. B. Carter. *J. Am. Ceram. Soc.*, 67 292, 1984.

[178] M. L. Kronberg. *Acta Metall.*, 5 507, 1957.

[179] H. Grimmer and R. Bonnet. *Phil. Mag. A*, 61 493, 1990.

[180] D. McKie and C. Mckie. *Essentials of Crystallography.* Blackwell Scientific Publications, 1986.

[181] *International Table For Crystallography. Volume A. Space-Group Symmetry.* Kluwer Academic Publishers, 1989.

[182] W. C. Mackrodt. In J. A. Pask and A. G. Evans, editors, *Ceramic Microstructures*, page 271. Plenum Press, London, 1986.

[183] K. Veit. *J. Jb. Miner. Geol. Paleont. Beil. Bd.*, 45 101, 1921.

[184] A. H. Heuer. *Phil. Mag.*, 13 379, 1966.

[185] L. A. Bursill and R. L. Withers. *Phil. Mag. A*, 40 213, 1979.

[186] S. Mckernan and C. B. Carter. *Ultramicroscopy*, 30 256, 1989.

[187] L. A. Bursill and P. J. Lin. *Phil. Mag. Letters*, 60 1, 1989.

[188] H. Gleiter and B. Charmers. *Prog. Mater. Sci.*, 16 1, 1972.

[189] W. D. Kingery. *J. Am. Ceram. Soc.*, 57 74, 1974.

[190] D. M. Duffy and P. W. Tasker. *Phil. Mag. A*, 50 143, 1984.

[191] K. Przybylski, A. J. Garratt-Reed, and G. J. Yurek. *J. Am. Ceram. Soc.*, 69 C264, 1986.